

# MATHEMATICAL MODELLING OF PLANAR SOLID OXIDE FUEL CELLS.

by

JAMIE IAN SANDELLS

A thesis submitted to  
The University of Birmingham  
for the degree of  
DOCTOR OF PHILOSOPHY (PHD.)

School of Chemical Engineering  
The University of Birmingham  
August 2013

**UNIVERSITY OF  
BIRMINGHAM**

**University of Birmingham Research Archive**

**e-theses repository**

This unpublished thesis/dissertation is copyright of the author and/or third parties. The intellectual property rights of the author or third parties in respect of this work are as defined by The Copyright Designs and Patents Act 1988 or as modified by any successor legislation.

Any use made of information contained in this thesis/dissertation must be in accordance with that legislation and must be properly acknowledged. Further distribution or reproduction in any format is prohibited without the permission of the copyright holder.

# ABSTRACT

In this thesis we construct a series of mathematical models from first principles to examine the advection, diffusion and reactions of species within a planar Solid Oxide Fuel Cell (SOFC). We reduce the complexity of an SOFC to flow and reaction across a flat, impermeable plate and begin by establishing a simplistic model for the incompressible, isothermal flow and reaction of hydrogen. Throughout the thesis we seek to extend this initial model by adding appropriate levels of complexity such as alternative fuels, compressibility and thermal effects.

In establishing solutions to these models we use a series of analytical techniques. We adopt the concept of boundary-layer flow and self similarity to simplify the model equations into a form where we can obtain analytical and efficient numerical solutions. We also utilise asymptotics to examine and validate the model around regions of singularities within the flow. Within each model we have examined the electrical performance of the cell and in some cases we have validated these results with existing experimental data.

## ACKNOWLEDGEMENTS

I would like to thank my supervisor Dr Jamal Uddin for his constant enthusiasm and support throughout the construction of this thesis. Furthermore, I would like to thank Prof. Stephen Decent and Prof. Kevin Kendall for their support and advice during the initial stages of this project.

The funding from EPSRC through the Doctoral Training Centre in Hydrogen Fuel Cells and Their Applications is also greatly acknowledged.

*“I may not have been sure about what really did interest me, but I was  
absolutely sure about what didn’t.”*

Camus (1998)

# CONTENTS

<b>1</b>	<b>Introduction</b>	<b>1</b>
1.1	What is a fuel cell? . . . . .	1
1.2	Fuel cell history . . . . .	2
1.3	Types of fuel cells . . . . .	4
1.3.1	Proton Exchange Membrane Fuel Cells (PEMFCs) . . . . .	5
1.3.2	Alkaline Fuel Cells (AFCs) . . . . .	6
1.3.3	Phosphoric Acid Fuel Cells (PAFCs) . . . . .	7
1.3.4	Molten Carbonate Fuel Cells (MCFCs) . . . . .	8
1.3.5	Solid Oxide Fuel Cells (SOFCs) . . . . .	9
1.4	Applications . . . . .	10
1.4.1	Portable . . . . .	10
1.4.2	Transportation . . . . .	11
1.4.3	Stationary . . . . .	12
<b>2</b>	<b>Solid Oxide Fuel Cells</b>	<b>13</b>
2.1	Components . . . . .	14
2.1.1	Anode . . . . .	15
2.1.2	Cathode . . . . .	15
2.1.3	Electrolyte . . . . .	16
2.1.4	Interconnect . . . . .	17
2.2	Types of SOFCs . . . . .	18
2.2.1	Planar . . . . .	18
2.2.2	Tubular . . . . .	20
2.3	SOFC fuelling . . . . .	22
2.4	SOFC Modelling . . . . .	24
2.5	Boundary-layer flow review . . . . .	26
2.6	Electrochemistry of fuel cells . . . . .	29
2.7	Aims and Objectives . . . . .	36
<b>3</b>	<b>Heterogeneous Reaction in Boundary-Layer Flow with Electrochemistry</b>	<b>38</b>
3.1	Model description . . . . .	38
3.2	A mathematical model for mass and momentum conservation . . . . .	41

3.3	Model electrochemistry . . . . .	44
3.4	Boundary conditions . . . . .	46
3.5	Non-dimensionalisation . . . . .	48
3.6	Outer region as $Re \rightarrow \infty$ . . . . .	50
3.7	Inner region as $Re \rightarrow \infty$ . . . . .	51
3.7.1	Asymptotic solution for $\xi \ll 1$ . . . . .	53
3.8	Numerical solution for $\xi = \mathcal{O}(1)$ . . . . .	55
3.8.1	Numerical method . . . . .	55
3.9	Results and discussions . . . . .	60
3.10	Validation . . . . .	70
3.11	Chapter Summary . . . . .	70
<b>4</b>	<b>Electrical Model</b>	<b>72</b>
4.1	Current-voltage plot . . . . .	72
4.2	Current-power plot . . . . .	76
<b>5</b>	<b>Heterogeneous Reaction in Boundary-Layer Flow with Electrochemistry with Methane Inlet</b>	<b>81</b>
5.1	Model description . . . . .	82
5.2	Mathematical model . . . . .	84
5.3	Boundary conditions . . . . .	87
5.4	Non-dimensionalisation . . . . .	88
5.5	Outer region as $Re \rightarrow \infty$ . . . . .	90
5.6	Inner region as $Re \rightarrow \infty$ . . . . .	91
5.6.1	Asymptotic solution for $\xi \ll 1$ . . . . .	93
5.7	Results and Discussion . . . . .	98
5.8	Electrical Model . . . . .	104
5.9	Chapter Summary . . . . .	106
<b>6</b>	<b>Compressible Heterogeneous Reaction in Boundary-Layer Flow with Electrochemistry</b>	<b>108</b>
6.1	Model description . . . . .	108
6.2	Mathematical model . . . . .	109
6.3	Boundary conditions . . . . .	113
6.4	Non-dimensionalisation . . . . .	115
6.5	Outer region as $Re \rightarrow \infty$ . . . . .	120
6.6	Inner region as $Re \rightarrow \infty$ . . . . .	120
6.6.1	Asymptotic solution for $\xi \ll 1$ . . . . .	124
6.7	Results and discussion . . . . .	134
6.7.1	Comparison to Incompressible Model . . . . .	141
6.8	Chapter Summary . . . . .	143

<b>7 Electrical model</b>	<b>151</b>
7.1 Current-voltage plot . . . . .	151
7.2 Current-power plot . . . . .	153
7.3 Comparison with experimental data . . . . .	156
<b>8 Conclusions and future work</b>	<b>160</b>
8.1 Future work . . . . .	161
<b>A Derivation of Boundary-Layer Equations</b>	<b>166</b>
<b>B Concept of similarity</b>	<b>171</b>
B.1 Derivation of similarity variable $\eta$ . . . . .	172
<b>C Mixture properties</b>	<b>175</b>

# LIST OF FIGURES

1.1 A diagram of Grove's gas voltaic cell. . . . .	3
2.1 A diagram of the structure and operation of an SOFC. . . . .	14
2.2 Planar SOFC configuration (Stambouli & Traversa, 2002). . . . .	18
2.3 Radial planar SOFC configuration (Stambouli & Traversa, 2002). . . . .	19
2.4 SOFC support configurations (Minh, 2004). . . . .	19
2.5 Flow configurations in planar SOFCs (Singhal & Kendall, 2003). . . . .	21
2.6 Tubular SOFC configuration (Singhal, 2000). . . . .	22
2.7 A view of the formation of a boundary-layer due to flow past a airfoil (Anderson Jr, 2005). . . . .	27
2.8 Typical profile of actual fuel cell voltage. . . . .	34
3.1 A diagram a full SOFC setup including inlet flows and mobile ion transfer. The cell reactions occur on the boundaries between the electrodes and the electrolyte. . . . .	40
3.2 A diagram of the flow in the anode of a planar SOFC, with the coordinate system shown. A schematic of the boundary layer formation within this region is also shown. . . . .	40
3.3 Temperature profile along the axis of an SOFC operating at 1173K (Cooper <i>et al.</i> , 2000). This demonstrates an almost constant temperature, relative to the inlet temperature, throughout the anode region . . . . .	42
3.4 Comparison of numerical (full line) and asymptotic (broken line) solutions for $Y_H(\xi, 0)$ when $U_{cell} = 0.5$ . The result are closely matched for $\xi \ll 1$ and diverge slightly as $\xi$ increase. . . . .	61
3.5 Numerical solution of $\frac{\partial Y_H}{\partial \xi}$ along the surface of the plate for $U_{cell} = 0.5$ . This demonstrates how the reaction rate of hydrogen along the surface of the plate varies. . . . .	61
3.6 $Y_H$ plotted along the surface of the plate for vary values of $\eta$ . This plot demonstrates the reliance of convergence on the value of $\eta$ . . . . .	62
3.7 $Y_H$ plotted against the coordinate system $(\xi, \eta)$ for $U_{cell} = 0.5$ . This demonstrates how the mass fraction of hydrogen varies throughout the flow domain. . . . .	63
3.8 $Y_W$ plotted against the coordinate system $(\xi, \eta)$ for $U_{cell} = 0.5$ . This demonstrates how the mass fraction of water varies throughout the flow domain (This is linked to the mass fraction of hydrogen since $Y_H + Y_W = 1$ ). . . . .	64

3.9	Plot of the surface mass fraction of hydrogen, $Y_H(\xi, 0)$ for $U_{cell}=1, 0.8, 0.6, 0.4, 0.2, 0$ . This demonstrates how the mass fraction of hydrogen along the surface of the plate varies when the cell potential is altered. . . . .	65
3.10	Plot of the surface mass fraction of hydrogen, $Y_H(\xi, 0)$ , against $\xi$ and varying values of $U_{cell}$ . This demonstrates how the surface mass fraction of hydrogen varies for all considered cell potentials. . . . .	66
3.11	Plot of the surface mass fraction of water, $Y_W(\xi, 0)$ , against $\xi$ and varying values of $U_{cell}$ (This follows from Fig 3.10 and from $Y_H + Y_W = 1$ ). . . . .	66
3.12	Plot of the surface mass fraction of hydrogen, $Y_H(\xi, 0)$ , against $\xi$ and varying values of the concentration of oxygen, $Y_O$ , on the air side of the fuel cell. This demonstrates how the surface mass fraction of hydrogen varies when the concentration of oxygen present within the cathode is altered. . . . .	67
3.13	Plot of the surface mass fraction of hydrogen, $Y_H(\xi, 0)$ , against $\xi$ and varying values of the inlet mass fraction of hydrogen $\tilde{Y}_H$ . This demonstrates how the surface mass fraction of hydrogen varies when the inlet composition of the anode is altered. . . . .	68
3.14	Plot of the surface mass fraction of hydrogen, $Y_H(\xi, 0)$ , against $\xi$ and varying values of Temperature $T$ . This demonstrates how the surface mass fraction of hydrogen varies when the operating temperature of the cell is altered . . .	69
3.15	Analytical and numerical model methodology applied to the model developed by Merkin (1996) . . . . .	71
4.1	Average current-voltage plot across the length $0 \leq \xi \leq 1$ . This demonstrates the relationship between the cell voltage and current density for this model. . . . .	74
4.2	Current-voltage plot for varying values of $\xi$ , $\xi=0, 0.2, 0.4, 0.6, 0.8, 1$ , where increasing $\xi$ corresponds to a right to left shift in curves. This demonstrates how the relationship between cell potential and current density varies at different positions along the plate. . . . .	75
4.3	Average current-power plot across the length $0 \leq \xi \leq 1$ . This demonstrates the relationship between the cell power density and current density for this model. . . . .	77
4.4	Current-power plot for varying values of $\xi$ , $\xi=0, 0.2, 0.4, 0.6, 0.8, 1$ , where increasing $\xi$ corresponds to a right to left shift in curves. This demonstrates how the relationship between the cell power density and current density varies at different positions along the plate. . . . .	78
4.5	Power density plotted against varying values of the concentration of oxygen on the air side, $Y_O$ , for $U_{cell}=0.5$ . This demonstrates how the achievable cell power density varies when the oxygen mass fraction within the cathode side of the cell is altered. . . . .	78
4.6	Power density plotted against varying values of the inlet mass fraction of hydrogen, $\tilde{Y}_H$ , for $U_{cell}=0.5$ . This demonstrates how the achievable cell power density varies when the anode inlet composition is altered. . . . .	79

4.7	Power density plotted against varying values of the cell temperature, $T$ , for $U_{cell}=0.5$ . This demonstrates how the achievable cell power density varies well the operating temperature of the cell is altered. . . . .	80
5.1	$Y_f$ plotted against the coordinate system $(\xi, \eta)$ for $U_{cell} = 0.5$ . This demonstrates how the mass fraction of methane varies throughout the flow domain.	99
5.2	$Y_W$ plotted against the coordinate system $(\xi, \eta)$ for $U_{cell} = 0.5$ . This demonstrates how the mass fraction of water varies throughout the flow domain. .	100
5.3	$Y_M$ plotted against the coordinate system $(\xi, \eta)$ for $U_{cell} = 0.5$ . This demonstrates how the mass fraction of carbon monoxide varies throughout the flow domain. . . . .	101
5.4	$Y_H$ plotted against the coordinate system $(\xi, \eta)$ for $U_{cell} = 0.5$ . This demonstrates how the mass fraction of hydrogen varies throughout the flow domain.	101
5.5	Plot of the surface mass fraction of methane, $Y_f(\xi, 0)$ , against $\xi$ and varying values of $U_{cell}$ . This demonstrates how the surface mass fraction of methane varies for all considered cell potentials. . . . .	103
5.6	Plot of the surface mass fraction of water, $Y_W(\xi, 0)$ , against $\xi$ and varying values of $U_{cell}$ . This demonstrates how the surface mass fraction of water varies for all considered cell potentials. . . . .	103
5.7	Plot of the surface mass fraction of carbon monoxide, $Y_M(\xi, 0)$ , against $\xi$ and varying values of $U_{cell}$ . This demonstrates how the surface mass fraction of carbon monoxide varies for all considered cell potentials. . . . .	104
5.8	Plot of the surface mass fraction of hydrogen, $Y_H(\xi, 0)$ , against $\xi$ and varying values of $U_{cell}$ . This demonstrates how the surface mass fraction of hydrogen varies for all considered cell potentials. . . . .	105
5.9	Average current-voltage (blue line) and current-power (black line) curves across the length of the cell $0 \leq \xi \leq 1$ . These plots demonstrate the relationship between the cell voltage and current density as well as the cell power density and current density within this model. . . . .	106
6.1	$Y_H$ plotted against the coordinate system $(\xi, \eta)$ for $U_{cell} = 0.5$ . This demonstrates how the mass fraction of hydrogen varies throughout the flow domain.	135
6.2	Numerical solution of $\frac{\partial Y_H}{\partial \xi}$ along the surface of the plate for $U_{cell} = 0.5$ . This demonstrates how the reaction rate of hydrogen along the surface of the plate varies. . . . .	135
6.3	$Y_W$ plotted against the coordinate system $(\xi, \eta)$ for $U_{cell} = 0.5$ . This demonstrates how the mass fraction of water varies throughout the flow domain. .	136
6.4	$T$ plotted against the coordinate system $(\xi, \eta)$ for $U_{cell} = 0.5$ . This demonstrates how the dimensionless absolute temperature varies throughout the flow domain. . . . .	137
6.5	$\rho$ plotted against the coordinate system $(\xi, \eta)$ for $U_{cell} = 0.5$ . This demonstrates how the dimensionless species mixture density varies throughout the flow domain. . . . .	137

6.6	$P$ plotted against the coordinate system $(\xi, \eta)$ for $U_{cell} = 0.5$ . This demonstrates how the dimensionless pressure varies throughout the flow domain.	138
6.7	Plot of the surface mass fraction of hydrogen, $Y_H(\xi, 0)$ , against $\xi$ and varying values of cell voltage $U_{cell}$ . This demonstrates how the surface mass fraction of hydrogen varies for all considered cell potentials.	139
6.8	Plot of the surface mass fraction of water, $Y_W(\xi, 0)$ , against $\xi$ and varying values of cell voltage $U_{cell}$ . (This follows from Fig 6.7 and from $Y_H + Y_W = 1$ ).	140
6.9	Plot of the surface temperature, $T(\xi, 0)$ , against $\xi$ and varying values of cell voltage $U_{cell}$ . This demonstrates how the dimensionless absolute temperature varies along the surface for all considered cell potentials.	141
6.10	Plot of the surface density, $\rho(\xi, 0)$ , against $\xi$ and varying values of cell voltage $U_{cell}$ . This demonstrates how the dimensionless density along the surface varies for all considered cell potentials.	142
6.11	Plot of the surface pressure, $P(\xi, 0)$ , against $\xi$ and varying values of cell voltage $U_{cell}$ . This demonstrates how the dimensionless pressure along the surface varies for all considered cell potentials.	143
6.12	Plot of the surface mass fraction of hydrogen, $Y_H(\xi, 0)$ , against $\xi$ and varying values of the mass fraction of oxygen on the air side of the cell $Y_O$ . This demonstrates how the surface mass fraction of hydrogen varies when the concentration of oxygen present within the cathode is altered.	144
6.13	Plot of the surface mass fraction of water, $Y_W(\xi, 0)$ , against $\xi$ and varying values of the mass fraction of oxygen on the air side of the cell $Y_O$ . This demonstrates how the surface mass fraction of water varies when the concentration of oxygen present within the cathode is altered.	145
6.14	Plot of the surface temperature, $T(\xi, 0)$ , against $\xi$ and varying values of the mass fraction of oxygen on the air side of the cell $Y_O$ . This demonstrates how the dimensionless absolute temperature along the surface varies when the concentration of oxygen present within the cathode is altered.	146
6.15	Plot of the surface density, $\rho(\xi, 0)$ , against $\xi$ and varying values of the mass fraction of oxygen on the air side of the cell $Y_O$ . This demonstrates how the dimensionless density along the surface varies when the concentration of oxygen present within the cathode is altered.	147
6.16	Plot of the surface pressure, $P(\xi, 0)$ , against $\xi$ and varying values of the mass fraction of oxygen on the air side of the cell $Y_O$ . This demonstrates how the dimensionless pressure along the surface varies when the concentration of oxygen present within the cathode is altered.	148
6.17	Plot of the comparison in the reaction rate of hydrogen between the incompressible and compressible models.	149
7.1	Average current-voltage plot across the length $0 \leq \xi \leq 1$ . This demonstrates the relationship between the cell voltage and current density for this model.	152

7.2	Comparison of current-voltage plots for varying values of $\xi$ , $\xi=0, 0.2, 0.4, 0.6, 0.8, 1$ , where increasing $\xi$ corresponds to a right to left shift in curves. This demonstrates how the relationship between cell potential and current density varies at different positions along the plate. . . . .	153
7.3	Average current-power plot across the length $0 \leq \xi \leq 1$ . This demonstrates the relationship between the cell power density and current density for this model. . . . .	155
7.4	Comparison of current-power plots for varying values of $\xi$ , $\xi=0, 0.2, 0.4, 0.6, 0.8, 1$ , where increasing $\xi$ corresponds to a right to left shift in curves. This demonstrates how the relationship between the cell power density and current density varies at different positions along the plate. . . . .	155
7.5	Average power density plotted against varying values of the mass fraction of oxygen on the air side, $Y_O$ , for $U_{cell} = 0.5$ . This demonstrates how the achievable cell power density varies when the oxygen mass fraction within the cathode side of the cell is altered. . . . .	156
7.6	Comparison of the current-voltage plots of the numerical model (solid line) and experimental data (Verbraeken <i>et al.</i> , 2012) (broken line) for $T_0 = 1173$ and $R_s = 1.007 \times 10^{-4}$ . . . . .	158
7.7	Comparison of the current-power plots of the numerical model (solid line) and experimental data (Verbraeken <i>et al.</i> , 2012) (broken line) for $T_0 = 1173$ and $R_s = 1.007 \times 10^{-4}$ . . . . .	159

# LIST OF TABLES

1.1	Fuel cell types (Fuel Cell Handbook, 2004) . . . . .	5
2.1	SOFC anode reactions. . . . .	23
2.2	Fuel impact on various fuel cells. . . . .	23
2.3	Ideal voltage of various fuel cells (Fuel Cell Handbook, 2004). . . . .	31
3.1	Parameters, their symbols, values and units . . . . .	55
3.2	Definitions of dimensionless parameters and their typical values . . . . .	56
5.1	Parameters, their symbols, values and units . . . . .	97
5.2	Definitions of dimensionless parameters and their typical values . . . . .	98
6.1	Parameters, their symbols, values and units . . . . .	133
6.2	Definitions of dimensionless parameters and their typical values . . . . .	133

# CHAPTER 1

## INTRODUCTION

### 1.1 What is a fuel cell?

A fuel cell is an electrochemical conversion device that utilises the chemical energy of a fuel and an oxidant to form electricity. Fuel cells are similar to batteries in that both contain an electrolyte which is sandwiched between an anode and a cathode and both convert the chemical energy of a fuel into electricity. They differ from the fact that fuel cells require a continuous supply of fuel and oxidant to operate where as a battery uses a stored fuel source. In theory, this would imply that a fuel cell can operate continuously as long as a constant supply of fuel and oxidant is pumped into the cell. A battery, on the other hand, consumes its anode and cathode in the generation of electricity and therefore either needs to be recharged or replaced in order to continue supplying electricity.

Generally, fuel cells consist of three layers which are two electrodes (the anode and cathode) on the outside of an electrolyte. The electrodes consist of a porous material which allows the fuel and oxidant to diffuse into the electrode. The electrolyte is made of a non-porous material to stop the fuel and oxidant mixing during the operation of the cell and to also conduct the charge carrier. Connecting the two electrodes is an interconnect which the produced electrons pass through to generate an electric current.

The interconnect can also be used to connect multiple cells in order to make a fuel cell stack. Furthermore, most fuel cells have gas channels which are used to supply fuel and air to their respective electrodes. As stated above, the fuel and air are not generally allowed to mix during the operation of the cell and therefore these channels must be kept gas tight. Fuel cells combine the fuel and air electrochemically in the cell to produce energy. This method is much more efficient than the general combustion of fuels and air which can produce harmful emissions in the process, depending on the fuel used to operate the cell.

## 1.2 Fuel cell history

Although still relatively unknown to the majority, fuel cells have been around since the early 19<sup>th</sup> century. Sir Humphry Davy was the first to demonstrate the concept of a fuel cell in 1801. Christian Friedrich Schönbein, a German-Swiss chemist, was accredited for inventing the fuel cell itself back in 1838.

One of the greatest pioneers in fuel cell research was Sir William Robert Grove, a Welsh judge and physical scientist. In 1839 he developed the 'gas battery', or the 'Grove cell' as it is known today. What Grove managed to prove from this is that an electrical current could be produced from the electrochemical reaction of hydrogen and oxygen. Figure 1.1 shows the gas voltaic battery cell developed by Grove. A few years later, in 1840, Grove actually demonstrated the first incandescent light, a concept that was later refined by Thomas Edison.

The cell developed by Grove was adapted further by Charles Langer and Ludwig Mond. It was in 1889 that the term 'fuel cell' was first given to their development. It was not until the late 1950s that development into fuel cells began to show significant practical use. In 1959 Francis Thomas Bacon constructed and demonstrated a 5 kW fuel cell system by modifying the Langer and Mond cell. Also in this year Harry Karl Ihrig

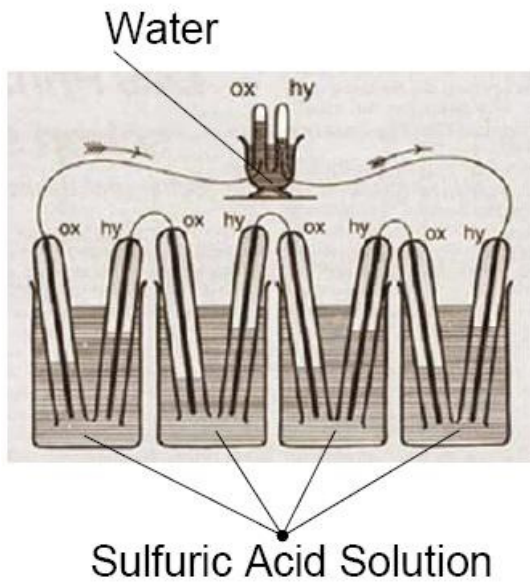


Figure 1.1: A diagram of Grove's gas voltaic cell.

modified the 5 kW system of Bacon and constructed a 15 kW cell stack that was fitted to power a tractor. The company responsible for fitting the fuel cell to the tractor also went on to develop fuel cell powered vehicles and submersible vessels for the US Air Force.

After the developments of Bacon and Ihrig, fuel cells began to make a much greater impact in research and commercial projects. NASA was the first to implement fuel cells as fuel cell generators on its space program in the early 1960s. These fuel cell generators were actually used during the Gemini space program which took place during the middle of the decade. Fuel cells were again used during the Apollo space missions where they provided electrical power and clean drinking water for the astronauts during their space mission. As a result of these missions, fuel cells were developed and incorporated on all space shuttle voyages. Fuel cells were also being developed by the Soviet Union during the period for usage in submarines and, eventually, in space travel.

The 1970s brought about greater interest and development into fuel cell vehicles, mainly due to the increase in environmental concerns and government legislation on vehicle

emissions. General Motors (GM) were one of the first companies to introduce fuel cell electric vehicles but at the time these were for demonstration purposes only. By the end of the century every major car manufacturer around the world had some focus on fuel cell electric cars. However, it would not be until 2008 that fuel cell cars became commercially accessible to the public.

It was during the 1990s where government funding for fuel cells began to become significant as solid oxide fuel cells (SOFCs) and polymer electrolyte fuel cells (PEMFCs) were realised as potential stationary and mobile power sources. This was particularly the case in the area of combined heat and power (CHP) units where the heat and electrical energies are utilised in micro-generation points. A huge push for zero emissions vehicles began in California in 1990 where a mandate was introduced aiming at producing alternative forms of powering vehicles. This decade also saw the introduction of fuel cells in portable devices such as mobile phones and laptops although the mobility of these devices were not on the same level as the standard battery powered comparisons.

### 1.3 Types of fuel cells

There are several different types of fuel cells that are distinguishable by certain properties which include electrolyte material, operating temperature and the conducting ions that pass through the electrolyte. By looking at these features we can determine the type of cell.

Table 1.1(Fuel Cell Handbook, 2004) shows the different types of fuel cells that exist and some of their properties. They vary greatly in temperature from very low temperature cells such as the Polymer Electrolyte Fuel Cell (PEMFC) to much higher temperature fuel cells like the Solid Oxide Fuel Cell (SOFC). In the lower operating temperature fuel cells, expensive catalysts such as platinum are required to promote the reaction. Moreover, in these cells there is a large restriction on the fuels which can be used since certain

fuels do not react at lower temperatures. Furthermore, these fuel cells suffer greatly from degradation if there are low levels of impurities in the fuel and during the reactions. The main benefit of these cells lies in their rapid start up time due to their low operating temperature. With regards to higher operating temperature cells, hydrocarbons can be directly utilized and less expensive catalysts are required. This aids against degradation as impurities from the reactions, such as carbon monoxide, can be used as a fuel in the cell. However, the high operating temperatures bring about difficulties in materials selection and gas tight sealing between cell components.

Fuel cell	Abbreviation	Mobile ion	Operating Temperature
Polymer Electrolyte Fuel Cell	PEMFC	$H^+$	60-80°C
Alkaline Fuel Cell	AFC	$OH^-$	50-200°C
Phosphoric Acid Fuel Cell	PAFC	$H^+$	$\approx 200^\circ C$
Molten Carbonate Fuel Cell	MCFC	$CO_3^{2-}$	$\approx 650^\circ C$
Solid Oxide Fuel Cells	SOFC	$O^{2-}$	600-1000°C

Table 1.1: Fuel cell types (Fuel Cell Handbook, 2004).

### 1.3.1 Proton Exchange Membrane Fuel Cells (PEMFCs)

The fuel cell which operates at the lowest temperature is the Proton Exchange Membrane Fuel Cell (PEMFC). The construction of the PEMFC consists of a very thin polymer membrane electrode, which is ion conducting, sandwiched between two porous carbon electrodes. This construction is often referred to as the membrane electrode assembly (MEA) (Debe *et al.*, 1999). PEMFCs operate at between 60-80°C, although work has been conducted on cells operating up to 200°C(Li *et al.*, 2003), and because of this they require expensive platinum catalyst in order to promote the slow reaction kinetics (Ellis *et al.*, 2001). Due to the presence of a platinum catalyst PEMFCs are required to operate on pure hydrogen as a fuel with less than 50 ppm of carbon monoxide to prevent catalyst poisoning effects (Faur Ghenciu, 2002). As with all types of fuel cells there are anode and

cathode reactions which occur at specific reaction sites within the porous electrodes. The anode reaction within a PEMFC takes the form



and the reaction at the cathode is given by



which gives an overall cell reaction



Through these reactions we can see that PEMFCs have a mobile ion  $H^+$  and that this ion is transferred from anode to cathode via the polymer electrolyte. The main advantage of PEMFCs is their rapid start up time due to the low operating temperatures. This makes them an ideal candidate for utilisation within the automotive sector and a replacement for the current internal combustion (IC) engines. PEMFCs can reach efficiency levels of around 50% when operating at partial load in automotive applications (Barbir & Gómez, 1997). The main disadvantage of PEMFCs is the requirement for expensive catalysts within the reaction kinetics. However, research is being conducted into using Nafion® membranes which reduce the platinum loading of the cell (Curnick *et al.*, 2010).

### 1.3.2 Alkaline Fuel Cells (AFCs)

Alkaline Fuel Cells (AFCs) use aqueous potassium hydroxide as an electrolyte (KOH) and were first introduced in 1902 (Gülow, 2004). AFCs have the ability to operate at temperatures between 50-200°C but can be operated at temperatures around 250°C if a higher concentration of KOH is used for the electrolyte (Fuel Cell Handbook, 2004).

The construction of AFCs can be split into 4 types (Gülgow, 2004): cells with a liquid electrolyte sandwiched between two porous electrodes, cells with a liquid electrolyte fixed to an electrolyte matrix, ELOFLUX (Winsel *et al.*, 1990) cells with a liquid KOH in the pores of gas diffusion electrodes and falling film cells (Tetzlaff *et al.*, 1994) with a liquid electrolyte used as a film between the gas diffusion electrodes.

The benefits of AFCs are that they have much better  $O_2$  kinetics compared to other fuel cells (Fuel Cell Handbook, 2004). Moreover, they have an ability to use liquid fuels which makes them an ideal energy producer for transport applications (Gülgow, 2004). The main drawback to AFCs is the sensitivity of the electrolyte to  $CO_2$ . This means that very pure hydrogen is required for a fuel and  $CO_2$  must be removed from air before this can be used as an oxidant.

The anode reaction within an AFC is given by



and the reaction at the cathode is



which gives the overall cell reaction



### 1.3.3 Phosphoric Acid Fuel Cells (PAFCs)

Phosphoric Acid Fuel Cells (PAFCs) construction consists of two porous carbon electrodes which sandwich a liquid phosphoric acid electrolyte which is saturated within a silicon carbide matrix. On the outside of each of the carbon electrodes is a current collector which

is not only used as a path for electron flow but is also used to cool the fuel cell down by transferring a fluid between the plate (Ellis *et al.*, 2001). PAFCs operating temperatures of around 200°C means that they are able to deal with slight impurities such as CO and  $CO_2$  with levels around 1 – 3% (Dhir, 2008). The anode reaction within a PAFC is given by



where the cathode reaction takes the form



which gives the full cell reaction

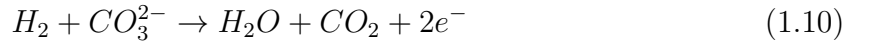


The structure and reactions of a PAFC are comparable to that of a PEMFC. Furthermore, the operating efficiencies of PAFCs are comparable to that of PEMFC but have lower power densities (Ellis *et al.*, 2001)

### 1.3.4 Molten Carbonate Fuel Cells (MCFCs)

Molten Carbonate Fuel Cells (MCFCs) operate at high temperatures of around 650°C. The structure of a MCFC is similar to that of the PAFC where two porous electrodes sandwich a porous matrix which retains molten carbonate. The benefits of operating at such a high temperature means that precious metal catalysts are not required in order to promote the reaction kinetics. Moreover, the need for pure or very low impurity hydrogen is not necessary as these cells are able to operate on hydrocarbons as well as hydrogen through internal reforming. Furthermore, there exist reactions that enable the utilisation

of carbon monoxide and carbon dioxide as fuels within the cell. The anode reaction within a MCFC is represented by



with the reaction at the cathode

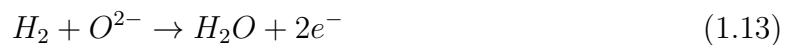


Therefore, we have the full cell reaction



### 1.3.5 Solid Oxide Fuel Cells (SOFCs)

Solid Oxide Fuel Cells (SOFCs) have the highest operating temperature of all the different types of fuel cells, between 600-1000°C. As with MCFCs they do not require expensive metal catalysts in order to promote reactions and they can utilise hydrocarbons as well as CO and  $CO_2$  as fuels within their anode. Furthermore, the heat generated by the exothermic anodic reaction within an SOFC can be utilised in such applications as water heating or combining the cell with a gas turbine. In doing this SOFC can reach operating efficiencies in the range of 85 – 95% (Huang & Goodenough, 2009). SOFCs have a similar structure to the other types of fuel cells with two porous electrodes sandwiching an electrolyte. In the case of SOFCs the electrolyte is now a solid structure which means the cell can be manufactured in a variety of geometries allowing for appropriate designs for different applications. The anode reaction within an SOFC is given by



and the cathode reaction is



giving the full cell reaction



The focus of this thesis is on SOFCs and as such more details of this type of fuel cell can be found in the proceeding chapter.

## 1.4 Applications

We have demonstrated the various types of fuel cells and their characteristics which cover a vast range of operating temperatures, geometries and manufacturing techniques. We would therefore expect there to be a vast array of applications for fuel cells and that each fuel cell would have an optimal application. In general, fuel cell applications are split into 3 main areas: portable, transportation and stationary power (Fuel Cell Today, 2013).

### 1.4.1 Portable

Portable applications of fuel cells are generally defined as those that built into, or charge, products that can be transported by a person for power generation (Fuel Cell Today, 2013). Within this application the power range is between  $5W - 500kW$  and can therefore be utilised in a variety of portable products. Some examples of fuel cells in portable power applications are laptops, mobile phones, hearing aids (fuel cell is used to recharge hearing aid batteries) and they are widely used in military devices. The primary fuel cells used within this sector are PEMFC and DMFC and are implemented to either replace or support current battery systems. The benefit of fuel cells in these situations is that compressed hydrogen (for PEMFCs) or liquid methanol (for DMFCs) can be

easily transported and would be lighter and cheaper than replacement batteries (Ellis *et al.*, 2001). They also allow for rapid recharging when used in conjunction with existing battery system (Fuel Cell Today, 2013).

### **1.4.2 Transportation**

One of the biggest sectors that fuel cells can be applied to is the transportation sector. Fuels cells can be utilised within this sector as either the primary power source for an electrical motor or to supplement a battery stack to extend the range of current battery powered vehicles. Fuel cells are not only restricted to cars but can also be implemented in manned and unmanned aerial vehicles, ferries, trains and any application that currently use an internal combustion (IC) or electrical engine. However, the main driving force is to replace the current IC engines, found in cars worldwide, with fuel cell battery hybrids. A list of fuel cell cars can be found in Fuel Cells (2003) where the reader may find details regarding types of fuel cell, range and fuel types of each vehicle as well as more detailed information. Although fuel cell vehicles have yet to become commonplace in current societies there is an aim from motor companies that 2015 will see initial commercialisation and sales of these types of vehicles (Fuel Cell Today, 2013). One limiting point to the commercialisation of fuel cell vehicles is the lack of appropriate infrastructure for refuelling and the need for pure hydrogen.

PEMFCs are generally regarded as the appropriate fuel cell type for implementation within the transportation sector. As with all fuel cells their efficiencies are much higher than that of the current IC engines. However, the main reason why PEMFCs are best suited for this application is due to their low operating temperature resulting in their start up time being very quick. This is ideal for vehicular use where immediate power is demanded as soon as the user wants to operate their vehicle.

### **1.4.3 Stationary**

The concept of stationary power is that which produces energy, with the possibility of supplementary heat, from a source which cannot be moved. Current stationary power, in the form of power stations, produces electricity at specific sites before distributing it to those who demand it. The heat supply for these locations is generally produced locally via some type of boiler system. One system being developed to change the way energy is produced and distributed is the combined heat and power (CHP) system. The basic idea of this system is that electricity and heat are produced from a fuel cell locally in a system that resembles a traditional boiler. These CHP systems range from 0.5kWe and 10kWe and can produce overall efficiencies of between 80-95% when both electrical and thermal powers are utilised (Fuel Cell Today, 2013). CHP units are being implemented widely in East Asia, particularly in Japan and South Korea, but they rely heavily on government funding to be commercially affordable.

Stationary power applications rely upon the continual (or relatively continual) operation of fuel cells to meet the constant power and heat demands. This allows us to negate the issue of rapid start up times that we required for transportation use. Therefore, SOFCs, MCFCs and PEMFCs are applicable fuel cells here with SOFCs and PEMFCs being more commercially utilised. One advantage of an SOFC system is that it is able to operate on natural gas which makes incorporating it into current infrastructure a much easier task both from a financial and a time scale point of view.

# CHAPTER 2

## SOLID OXIDE FUEL CELLS

Like normal fuel cells, SOFCs are built up of an electrolyte sandwiched between an anode and cathode. The electrolyte, in this case, conducts oxygen ions ( $O^{2-}$ ) from the cathode side, through the electrolyte, to the anode side. On the anode side, the oxidation of the fuel occurs. SOFCs work on either hydrogen or hydrocarbons for the fuel source and air, generally, as the oxidant. A large majority of the research has been done into using methane ( $CH_4$ ) as the fuel source rather than the cleaner hydrogen. This is because methane operates better at higher temperatures compared to hydrogen and it is much more accessible and cheaper to get hold of. Moreover, oxygen is generally used as the oxidant due to its abundance in the atmosphere. Fig. 2.1 shows the general operation of an SOFC.

As can be see from Fig. 2.1 oxygen gets pumped into the cathode side where it reacts with the catalyst and electrons to reduce into oxygen ions ( $O^{2-}$ ). These ions are then conducted by the electrolyte where they move through to the anode side. Here the fuel is pumped in and becomes oxidized, by the oxygen ions, to form water as well as other by-products (depending on the fuel this could be carbon monoxide or in the case of hydrogen this would just be water), and electrons. These electrons then get forced through the interconnect from the anode to the cathode which generates an electric current. The

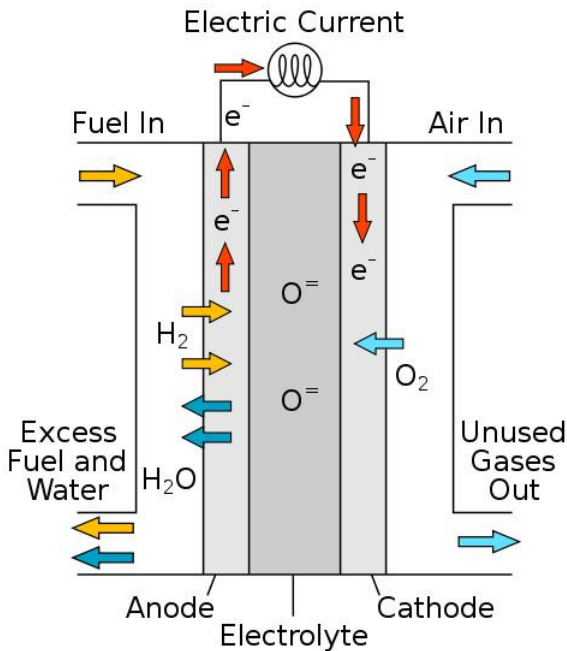


Figure 2.1: A diagram of the structure and operation of an SOFC.

by-products from the reactions and excess inlet species are then removed from the cell.

## 2.1 Components

As we have stated, the general construction of an SOFC is a solid electrolyte which is sandwiched between two porous electrodes. An additional cell component is the interconnect which facilitates the transfer of electrons from anode to cathode as well as connecting multiple cells in a fuel cell stack. Selecting the appropriate materials for each of the cell components is a difficult task since one needs to consider the electrocatalytic, electrochemical and thermomechanical properties, with particular focus on matching the thermal expansion coefficients of adjoining materials due to the high operating temperatures (Tietz, 1999).

### **2.1.1 Anode**

Within an SOFC the anode plays a vital role in the efficient operation of the cell. It must be porous to allow species to be transferred to the reaction sites and allow byproducts to be transferred away from them. Furthermore, it must have some level of electrical conductivity to transfer the produced electrons from the reaction sites to the interconnect. Finally, it must have good levels of ionic conductivity in order for the electrochemical oxidation reaction to take place. Hence, selecting an appropriate material with which to construct the anode is a very important task.

The most commonly used anode material is a nickel-yttria stabilized zirconia (Ni-YSZ) cermet. This material has several benefits which include: low cost, low charge resistance, excellent reforming catalyst (nickel), electrical conductivity (nickel), ion conductivity (YSZ) and the ability to match thermal expansion coefficients with other cell components by managing the ratio of YSZ to nickel (Zhu & Deevi, 2003b). The major drawback of using this material is that the nickel can be seriously affected by coking (carbon build up), re-oxidation and deactivation due to contaminants in the fuel (in the case of SOFCs this is sulfur poisoning)(Liu *et al.*, 2011).

Due to the issues described above, research has been conducted into nickel free anode material. The main focus of this research has been in ceria based anodes since they have shown to produce similar power densities when operating on  $CH_4$  compared to fuel cells operating on  $H_2$  (Murray *et al.*, 1999).

### **2.1.2 Cathode**

The cathode of an SOFC, like all other components, plays a significant role in the overall functionality of the cell and as such choosing an appropriate material to compose the cathode out of is a difficult choice. The material is required to be conductive of electrons in order to promote the oxygen reduction reaction and conduction of oxygen ions so that

these can be transferred to the electrolyte. Moreover, it is required to be porous to allow the oxidant to be transported to the reaction sites whilst also removing and unreacted species.

The majority of cathode materials are lanthanum-based perovskites and in the case of high temperature SOFCs it is common to use strontium doped lanthanum manganite. This material does not perfectly fit into the criteria required from a cathode but it does have several advantages which include: close thermal expansion coefficients to YSZ, adequate electronic and ionic conductivities (inadequate conductivities at low temperatures), chemical stability and relatively high activity (Fuel Cell Handbook, 2004). This results in high polarisation effects and energy loss within the cathode where implementation of new materials is hampered due to the fact that it is not proven to have long term stability and compatibility (Liu *et al.*, 2011). Studies have been conducted into changing the composition to include more strontium or adding in cobalt or iron (Simner *et al.*, 2003). Although adding materials such as cobalt can increase the electrical and ion conductivity they also increase the thermal expansion coefficient which can cause delamination between the cathode and the electrolyte (Ivers-Tiffé *et al.*, 2001).

### 2.1.3 Electrolyte

The solid electrolyte structure can be constructed out of a number of different materials, each with their advantages and disadvantages. The main purpose of the electrolyte is to transfer oxygen ions from anode to cathode at high temperatures whilst maintaining similar thermal expansion coefficients to both of these electrode compositions. Here we will only consider the most common electrolyte materials.

In our case of ion conducting SOFCs the most commonly used electrolyte materials are: doped zirconia (generally of the form yttria stabilized zirconia (YSZ)), ceria based conductors and lanthanum gallate (Ivers-Tiffé *et al.*, 2001; Liu *et al.*, 2011). The most

common electrolyte material is YSZ due to its high ion conductivity in the range of temperatures that SOFCs operate in (Fuel Cell Handbook, 2004). This material also demonstrates good mechanical stability as well as an abundance of raw materials for manufacture (Ivers-Tiffé *et al.*, 2001). Ceria based conductors such as gadolinium-doped ceria are more conductive than the YSZ electrolyte which make them an ideal candidate for SOFCs operating at lower temperatures above 600°C (Wang *et al.*, 2000; Fuentes & Baker, 2008). Lanthanum gallate electrolytes have the ability to be utilised in SOFCs that operate at around 600°C (Fuel Cell Handbook, 2004). Furthermore, they have been shown to have more than twice the electrical conductivity of YSZ electrolytes and have comparable thermal expansion coefficients to that of cathode materials (Lee *et al.*, 2007).

#### 2.1.4 Interconnect

The interconnect within an SOFC is one of the most important parts of the cell. This is due to the fact the the interconnect carries the charge from the anode and out of the cell, generally to a neighboring cathode. Moreover, the interconnect is exposed to the species, reactions and temperatures of all the other cell components. This makes choosing an optimal material for the interconnect an extremely difficult task.

When selecting an interconnect material there are several criteria that need to be satisfied. Some of these criteria include: high electrical conductivity, thermal expansion coefficients close to those of other cell components, resistance to oxidation, sulfidation and carburisation, stability at high temperatures, simple fabrication and low permeability to oxygen and hydrogen (Zhu & Deevi, 2003a).

As with all of the cell components there are several possible materials and combination of materials which can be used as an interconnect. Lanthanum chromite ( $LaCrO_3$ ) is the most commonly used ceramic interconnect material (Minh & Takahashi, 1995). The conductivity of  $LaCrO_3$  is not high enough to be utilised as an interconnect material so

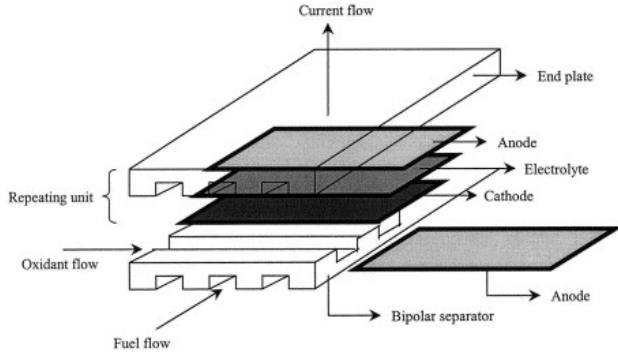


Figure 2.2: Planar SOFC configuration (Stambouli & Traversa, 2002).

it is usually doped with strontium or calcium (Fergus, 2004).

## 2.2 Types of SOFCs

There are two main design types of SOFCs which are planar and tubular. Each of these designs have their own subdesign configurations. In the case of planar cells we can have radial or the standard square plate design. In the case of tubular cells we have tubular and micro-tubular design.

### 2.2.1 Planar

The two main designs of planar SOFCs are the square plate and radial plate configurations shown in Fig. 2.2 and Fig. 2.3 (Stambouli & Traversa, 2002). The planar design configuration of a single cell consists of flat plates (either rectangular or circular) which are connected in an electrical series (Minh, 2004). Within each of these designs there exists configurations that determine which component of the cell supports the cell. The supporting component within the cell can be one of the following: Electrolyte, Cathode, Anode, Porous-Substrate, Interconnect. The way in which these configurations might be constructed are depicted in Fig. 2.4 (Minh, 2004) .

Early SOFC configurations utilised an electrolyte support where a thick electrolyte

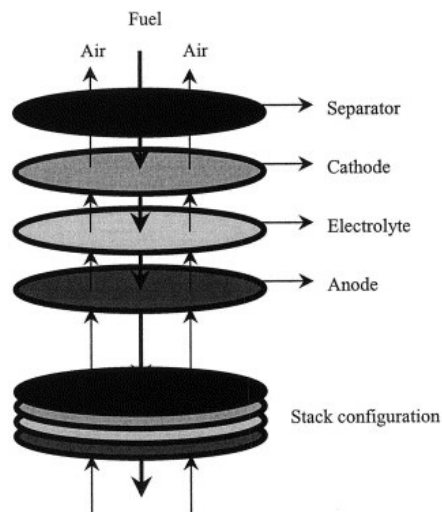


Figure 2.3: Radial planar SOFC configuration (Stambouli & Traversa, 2002).

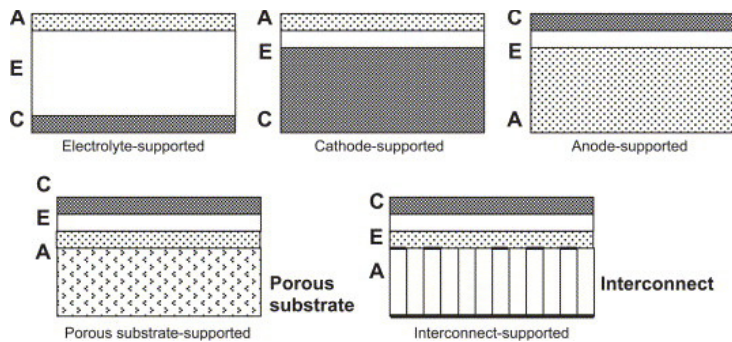


Figure 2.4: SOFC support configurations (Minh, 2004).

of  $> 200\mu m$  is used (Fuel Cell Handbook, 2004). The benefit of having an electrolyte supported cell is the structural stability it offers. However, there is a requirement for a cell of this type to operate at a higher temperatures in order to minimise ohmic losses (Singhal & Kendall, 2003). Anode supported cells have a porous anode between 0.5-1 mm thick and a thin electrolyte which gives a highly conductive substrate but can also lead to reoxidation of the anode and mass transport issues due to the thickness of this part of the cell (Singhal & Kendall, 2003). Cathode supported SOFCs are considered to be inferior to that of anode supported cells (Fuel Cell Handbook, 2004) so we will not give details of this type of cell here. Within the electrolyte supported cells we have electrodes approximately  $50 \mu m$  thick and an electrolyte which is  $5 - 15 \mu m$  thick (Fuel Cell Handbook, 2004). This enables a reduction in the operating temperature and alleviates mass transport issues but can cause oxidation of the interconnect as well as flowfield design limitations due to the support requirement of the cell (Singhal & Kendall, 2003).

The most important design feature of planar SOFCs is gas flow configuration and gas manifolding. Flowfields are used in planar SOFCs to uniformly distribute gas and promote heat and mass transfer within the cell (Singhal & Kendall, 2003). The different configurations of flowfields can be seen in Fig. 2.5 (Singhal & Kendall, 2003) where the shape and design of each of the flow fields effects the distribution of current and temperature and can be used to optimise stack designs.

### 2.2.2 Tubular

There are two main types of tubular SOFCs, those which have a large diameter ( $> 15 mm$ ) and microtubular SOFCs which have a very small diameter ( $< 5 mm$ ). The large diameter tubular cells use the Siemens Westinghouse design as depicted in Fig. 2.6 (Singhal, 2000). In this design the cells are  $> 15 mm$  in diameter and up to  $600 mm$  in length. The microtubular design was introduced in 1990 (Singhal & Kendall, 2003) and initial

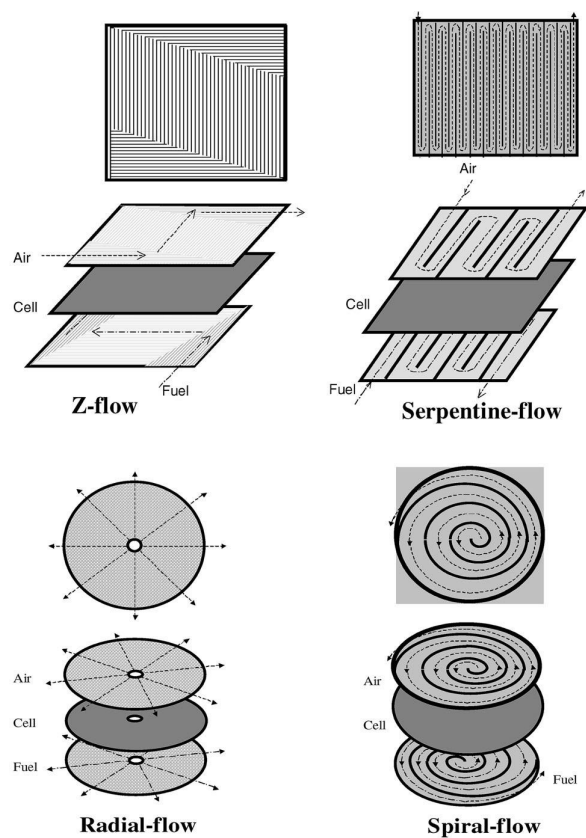


Figure 2.5: Flow configurations in planar SOFCs (Singhal & Kendall, 2003).

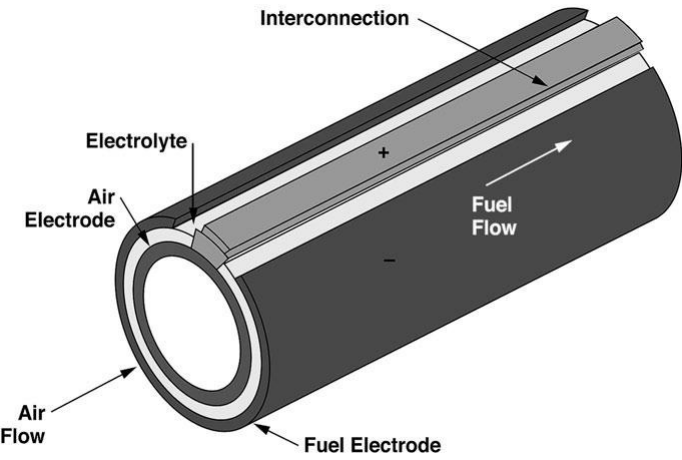


Figure 2.6: Tubular SOFC configuration (Singhal, 2000).

electrochemical testing was conducted at the University of Middlesex (Kendall, 1993).

The support designs that were outlined in section 2.2.1 are also applicable to tubular SOFCs. The electrolyte supported cells have a similar design to that for planar SOFCs, with the exception that the electrolyte is constructed as a tube shape rather than a flat plate. For electrode supported cells, mainly anode supported, the electrode is between  $500 - 3000 \mu m$  thick for standard tubes and between  $200 - 500 \mu m$  thick for microtubular cells. As with planar cells increasing the thickness of the electrodes does enable a lower operating temperature to be adopted but it also increases mass transport issues. Porous and interconnect supported SOFCs have the same characteristics for both planar and tubular design apart from their obvious construction.

## 2.3 SOFC fuelling

As mentioned in section 1.3.5, SOFCs have the ability to operate on hydrocarbons as well as hydrogen. Moreover, they are able to utilise species such as  $CO$  and  $CO_2$  as fuels which gives SOFCs a huge advantage over fuel cells operating at a lower temperature. Apart from hydrocarbons SOFCs have the ability to operate on liquid fuels such as methanol, ethanol, dimethyl ether, liquified petroleum gas and other conventional liquid fuels (Cimenti &

Hill, 2009). For the purpose of this study, however, we will concentrate solely on pure hydrogen and methane as possible anode inlet fuels. Table 2.1 (Akhtar, 2009; Dhir, 2008) gives details of the possible reactions that can occur within the anode of an SOFC.

Reaction	Equation
Methane steam reforming	$CH_4 + H_2O \rightarrow 3H_2 + CO$
Methane dry reforming	$CH_4 + CO_2 \rightarrow 2H_2 + 2CO$
Shift reaction	$CO + H_2O \rightarrow H_2 + CO_2$
Methane full combustion	$CH_4 + 2O_2 \rightarrow 2H_2O + CO_2$
Methane partial oxidation	$CH_4 + \frac{1}{2}O_2 \rightarrow 2H_2 + CO$
Hydrogen full combustion	$H_2 + \frac{1}{2}O_2 \rightarrow H_2O$
Carbon monoxide full combustion	$CO + \frac{1}{2}O_2 \rightarrow CO_2$
Methane electrochemical oxidation	$CH_4 + 4O^{2-} \rightarrow 2H_2O + CO_2 + 8e^-$
Carbon monoxide electrochemical oxidation	$CO + O^{2-} \rightarrow CO_2 + 2e^-$
Hydrogen electrochemical oxidation	$H_2 + O^{2-} \rightarrow H_2O + 2e^-$
Methane cracking	$CH_4 \rightarrow 2H_2 + C$
Boudouard reaction	$2CO \rightarrow CO_2 + C$
Steam gasification	$H_2O + C \rightarrow H_2 + CO$

Table 2.1: SOFC anode reactions.

SOFCS are not completely immune to the effects of species poisoning but they are the most resistive fuel cell type. The impact of certain fuels on the different types of fuel cells can be found in Table 2.2 (Fuel Cell Handbook, 2004).

Fuel	PEMFC	AFC	PAFC	MCFC	SOFC
$H_2$	fuel	fuel	fuel	fuel	fuel
$CO$	poison	poison	poison	fuel	fuel
	(50ppm per stack)		(< 0.5%)		
$CH_4$	diluent	poison	diluent	diluent	fuel
$CO_2 & H_2O$	diluent	poison	diluent	diluent	diluent
$S$		poison	poison	poison	poison
			(< 50ppm)	(< 0.5ppm)	(< 1ppm)

Table 2.2: Fuel impact on various fuel cells.

## 2.4 SOFC Modelling

Over recent decades much emphasis has been put on developing accurate models for the different phenomena occurring in SOFCs, which has brought about a large amount of published work. Due to the complexity of modelling fuel cell operations in a 3 dimensional framework much of the work that is done has typically used computational fluid dynamics (CFD). Below is a review of some of the modelling work that has been conducted.

Lehnert *et al.* (2000) developed a one-dimensional numerical simulation to describe the transport of gases inside an SOFC anode. The authors were particularly interested in internal steam reforming and the inhomogeneous temperature distributions that could lead to thermal stress and materials failure. Moreover, they used experimentally derived reaction rates and structural material properties in order to gain accurate results. The authors conducted a sensitivity analysis of the structural properties of the anode in order to gain an understanding of the methane conversion rate. They found that reducing the structural parameter  $\psi$ , where  $\psi$  is the ratio of the porosity to the tortuosity, lowered the overall methane conversion rate. Since the fast reforming reaction is linked to the inhomogeneous temperature distribution, decreasing the structural parameter would lead to a decrease in the thermal stress on the anode.

A mathematical model for a full tubular solid oxide fuel cell was developed by Bessette *et al.* (1995). The authors used a complete set of electrochemical and thermal factors with experimental validation of a single cell test from Westinghouse. However, no link was made between the electrochemical and thermal factors and the reaction rate of species. The developed model showed good correlation with that of the test cell, around 5% with some results much better than that of the cell. Their model results showed a much higher voltage for a hydrogen/carbon monoxide fuel mixture compared to just hydrogen, and a similar results was found with oxygen rather than air as an oxidant.

More rigorous mathematical models for fuel cells, in particular SOFCs, are very limited. Copcutt *et al.* (1996) generated a mathematical model for the reaction and diffusion inside a circular planar SOFC using methane and oxygen as the relevant fuel and oxidant, respectively. An extension of this model was presented by Billingham *et al.* (1999) where a much greater focus on the electrochemistry that occurs during fuel cell reactions was given. The authors introduced the ability to draw a current from the fuel cell model as well as ohmic effects on cell potential. Cooper *et al.* (2000) developed a mathematical model for the advection, diffusion and reaction within a tubular SOFC operating on a methane and water initial anode mixture. The authors used a method of matched asymptotics to solve for the mass fractions of the chemical species and confirmed these asymptotics with a numerical solution to the nonlinear problem using finite differences. Comparisons were made with experimental data for the mass fractions of species, for varying values of the cell potential, in the exhaust and were shown to be closely matched. This model was extended slightly by Andrews (2008) to examine the inlet flow when the radius of the inlet tube is smaller than the inner radius of the tubular cell.

An extensive three-dimensional model for an SOFC was produced by Bove & Uber-tini (2006). They constructed a time dependent numerical model which considered all phenomena occurring in each component of the cell, with all equations independent of cell geometry. Like in many SOFC modelling literature, the TPB is limited to a finite space and so equations in this region are generally treated as boundary conditions. The model has been numerically solved using the fuel cell module within the CFD software FLUENT<sup>®</sup> in order to obtain results in three-dimensions. The results of this model showed current density distributions in a micro-tubular SOFC when the current collector position is varied from the ends of the tube to thin wire wrapped around the tube. They showed for current collectors at the end of the tube that the current density distribution was along the whole tube, therefore, leading to an increase in ohmic resistance. Thus,

leading to the conclusion that wires wrapped round the tube are a better design for the current collector.

## 2.5 Boundary-layer flow review

An important factor of this work lies within a subsection of mathematics known as boundary-layer flow. Throughout this thesis we will continually refer to boundary-layer flow or indeed the boundary-layer equations. Here we give a brief overview of the concept of boundary-layer flow, some interesting properties and the theory and the construction of the boundary-layer equations.

Boundary-layer flow is the theory of the influence of viscosity, in fluid flow over a body, at a small distance away from a solid wall for large Reynolds numbers, which we will define later in this section. The concept of boundary layer flow is that the fluid adjacent to a solid boundary adheres to the boundary and thus moves at the same velocity as the boundary, known as the no-slip condition. The idea was first introduced by Ludwig Prandtl in 1904 during his presentation at the Third Mathematics Congress and later in his published work (Prandtl, 1904). Since its introduction, the areas of fluid dynamics and aerodynamics have consistently used the idea of boundary-layer development within flows over solid bodies and the extension over porous bodies.

Ludwig Prandtl's paper gave the first view into this new method on the effects of friction on the fluid which was in immediate contact with a solid surface. He showed using experimental and theoretical considerations that the flow past a body could be separated into two regions, a very thin region close to the solid body and the remaining flow outside of this region. He found that in this thin region (boundary-layer) the viscosity has an effect of the flow, even for an almost inviscid fluid like air. Outside of this region the frictional effects were negligible and thus need not be considered. Fig. 2.7 (Anderson Jr,

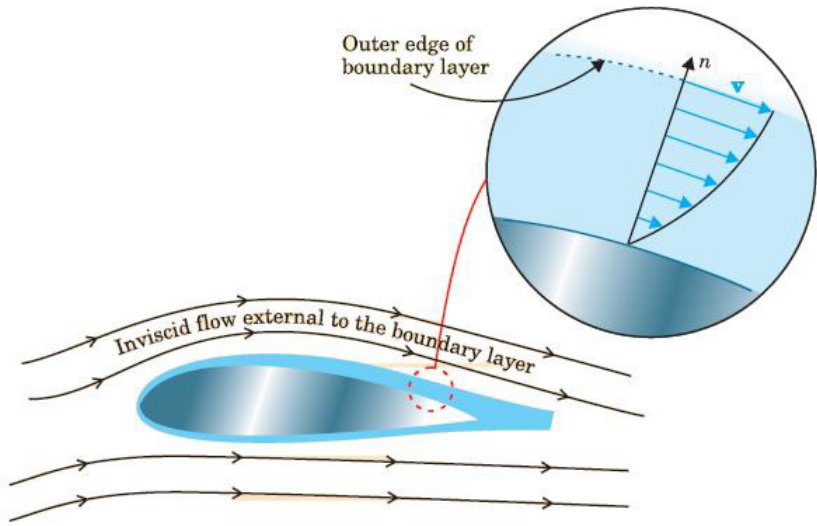


Figure 2.7: A view of the formation of a boundary-layer due to flow past a airfoil (Anderson Jr, 2005).

2005) shows the basic outline of boundary-layer theory for flow past a thin airfoil. We can see that in this thin region the velocity changes from the velocity of the body to the free stream velocity in a very short distance. Hence, in this region there is a large velocity gradient and thus, due to the relationship between velocity gradients and shear stress, the shear stress within this region can be large and hence cannot be neglected.

The thickness of such a boundary layer can be approximated if the flow remains laminar, which depends on the Reynolds number as will be shown later. So if the Reynolds number does not exceed that of the transition values to turbulent flow we can calculate the boundary layer thickness at a distance  $x$  from the forward edge of the body to be

$$\delta(x) = \frac{x}{Re^{\frac{1}{2}}}, \quad (2.1)$$

where  $Re$  is the Reynolds number given by

$$Re = \frac{U_0 x}{\nu}, \quad (2.2)$$

where  $U_0$  is the freestream velocity outside of the boundary layer and  $\nu$  is the kinematic viscosity

An interesting property of boundary-layers is that under certain geometries, of flow or of the body, the boundary layer can separate from the surface of the body and move downstream. Separation is caused when the fluid flow moves against a pressure gradient and the energy and momentum of the flow become too small to counteract the viscosity. Therefore, the fluid is brought to rest and the fluid separates from the wall at the point where

$$\frac{\partial u}{\partial y} = 0. \quad (2.3)$$

This separation causes the formation of eddies in the wake of the body and changes the pressure distribution over the body. In fact, the change in pressure distribution creates pressure drag on the body which can be calculated through the application of boundary-layer theory. An example of this is flow in a pipe with an increasing cross section. Hence, boundary-layer theory is able to give results on the optimal shape of a body in order to reduce or avoid this separation occurring. Boundary-layer theory also has applications to many industrial processes such as calculating the point of maximum lift of an airfoil and applications of heat transfer between a solid and a fluid flow. Other examples of boundary-layer flow and solutions can be found in Schlichting & Gersten (2004).

The flow within a boundary-layer might not always be laminar over the whole body. More specifically, under certain conditions a transition phase from laminar flow to turbulent flow can occur. This transition phase is dependent on the value of the Reynolds number, which defines the ratio between the viscous and inertia terms. For the flow past

a semi-infinite flat plate, we can express the region in which the boundary-layer becomes turbulent as a function of the position along the plate (Meksyn, 1961)

$$Re_x = \frac{Ux}{\nu} \sim 3 \times 10^5, \quad (2.4)$$

Turbulence can also depend on the thickness of the boundary-layer and via the Reynolds number we can define the region in which the flow becomes turbulent

$$Re_\delta = \frac{U\delta}{\nu} \sim 1000, \quad (2.5)$$

where  $\delta$  is the boundary-layer thickness.

Details of how one can simplify the equations of motion into the boundary-layer equations can be seen in appendix A. We will utilise these derived boundary-layer equations throughout the model development within this thesis. For more details on the construction, properties and solutions to various models which use boundary-layer flow we point the reader in the direction of Schlichting & Gersten (2004), Rosenhead (1963) and Meksyn (1961).

## 2.6 Electrochemistry of fuel cells

We are now going to introduce the relevant electrochemistry involved in SOFC modelling. Electrochemistry is a key factor to consider in any fuel cell model and so it must be discussed in detail before we can proceed further.

### Gibb's Free Energy.

An electrochemical reaction, within a fuel cell, operating at a constant temperature and

pressure has a maximal amount of work done, with the rest forming temperature losses. This work done, or useful energy, is given by the Gibb's Free Energy equation (Fuel Cell Handbook, 2004)

$$\Delta G = \Delta H - T\Delta S, \quad (2.6)$$

where  $\Delta G$  is the free energy (useful energy),  $\Delta H$  is the reaction enthalpy change,  $T$  is the absolute temperature, and  $\Delta S$  is the change in entropy. Under standard state conditions (temperature of 298 K and pressure of 1 atm) we may write (2.6) as

$$\Delta G^0 = \Delta H^0 - T\Delta S^0. \quad (2.7)$$

### **Ideal Voltage.**

The ideal voltage of a fuel cell is the maximum energy that can be converted into electrical energy. Obviously, this is related to the Gibb's Free Energy by

$$U^0 = -\frac{\Delta G}{zF}, \quad (2.8)$$

where  $U^0$  is the ideal voltage,  $z$  is the number of electrons transferred during the electrochemical reaction, and  $F$  is Faraday's constant ( $96485.33 \text{ C mol}^{-1}$ ). The ideal voltage for each different type of fuel cell and temperature are listed in Table 2.3 (Fuel Cell Handbook, 2004)

### **Nernst Open Circuit Voltage.**

The ideal voltages shown in Table 2.3 are taking into account an idealised system and therefore not a realistic electrochemical cell. During fuel cell operation, high temperature

Fuel cell	Temperature	Ideal Voltage
Polymer Electrolyte Fuel Cell	353K	1.17
Alkaline Fuel Cell	373K	1.16
Phosphoric Acid Fuel Cell	478K	1.14
Molten Carbonate Fuel Cell	923K	1.03
Intermediate Temperature Solid Oxide Fuel Cells	1073K	0.99
High Temperature Solid Oxide Fuel Cells	1373K	0.91

Table 2.3: Ideal voltage of various fuel cells (Fuel Cell Handbook, 2004).

gradients and pressure changes can alter the total cell voltage from this open circuit voltage. Furthermore, if the fuel and oxidant entering the cell are not pure then the voltage will deviate from the open circuit voltage (OCV). The OCV is the voltage of the cell when no current is drawn from it. Walther Nernst, the German Nobel Prize winning physical chemist, was the first to developed the equation that gives details of the full cell voltage in an electrochemical cell. The Nernst equation can appear in many different forms with dependence on pressure, concentration etc. but the most general form is given by (Fuel Cell Handbook, 2004)

$$U^N = U^r + \frac{RT}{zF} \ln \frac{\Pi[\text{reactant fugacity}]}{\Pi[\text{product fugacity}]}, \quad (2.9)$$

where  $R$  is the gas constant ( $8.314 \text{ J mol}^{-1}\text{K}^{-1}$ ) and fugacity denotes the gases real pressure and is therefore different from the ideal gas law pressure. An alternative way to describe the cell voltage is to examine the driving force for the migration of oxide ions from cathode to anode. In single and dual chamber SOFCs this migration of ions is a result of the oxygen chemical potential or oxygen partial pressure gradients between the two electrodes. Thus, we may express the Nernst equation in the following form

$$U^N = \frac{RT}{zF} \ln \left( \frac{P_{O_2,\text{cat}}}{P_{O_2,\text{an}}} \right), \quad (2.10)$$

where  $P_{O_2}$ , in the above equation, represents the partial pressure of oxygen at the cathode

and anode.

### Fuel Utilisation.

Utilisation of fuel is a highly important aspect of cell performance, and being able to accurately estimate this value will enable a greater estimate of fuel cell performance. There are two approaches to accurately predict fuel utilisation, both given in Akhtar *et al.* (2009)

$$\eta_U = \frac{\dot{m}_{f,reacted}}{\dot{m}_{f,in}} = \frac{M j_{tot}}{z F \dot{m}_{f,in}}, \quad (2.11)$$

where  $\dot{m}_{f,reacted}$  is the mass flow rate of fuel reacted in the cell ( $kg\ s^{-1}$ ),  $\dot{m}_{f,in}$  is the mass flow rate of fuel into the cell,  $M$  is the molar mass of the fuel ( $kg\ mol^{-1}$ ),  $j_{tot}$  is the total current at peak power density ( $A$ ). Further to this, another representation of fuel utilisation is given by

$$\eta_U = 1 - \frac{\dot{m}_{f,out} \Delta h_{f,out}}{\dot{m}_{f,in} \Delta h_{f,in}}, \quad (2.12)$$

where  $\dot{m}_{f,out}$  is the mass flow rate of fuel leaving the cell,  $\Delta h_{f,out}$  and  $\Delta h_{f,in}$  are the specific enthalpies associated with completely oxidizing the exhaust and inlet fuel, respectively.

Each of the above fuel utilisation equations has its own advantages and disadvantages. The first, equation (2.11), only considers the amount of fuel that is available to be converted into useful electrical energy, within its application. Therefore, it does not consider heating effects, polarisations or any other losses in energy which result in unavailable energy for useful, electrical generation. Furthermore, the current collector efficiency plays a vital role in determining peak power density and current. The main advantage of using this form of fuel utilisation equation is its ease of calculation.

The second representation of fuel utilisation, (2.12) does take into account the thermal

losses by examining the ratio between the outlet and inlet heating values. However, this is not application specific, as for in the case of combined heat and power, heat energy would be deemed a useful energy output and would therefore be represented as utilisation of fuel. It is because of this anomaly that Equation (2.11) is more commonly used.

### **Fuel Cell Losses.**

As has been described with voltage, an electrochemical cell is not an idealised system and so losses in voltage occur due to these imperfections. These imperfections come in the form of polarisations (or overpotentials) which consist of ohmic, activation, and concentration polarisations. Therefore, the actual operating cell voltage is less than the cell voltage described by the Nernst equation due to these additional losses, and can be expressed as (Mounir *et al.*, 2010)

$$U_{cell} = U^N - (\eta_{ohm} + \eta_{act} + \eta_{conc}), \quad (2.13)$$

where  $U_{cell}$  is the total cell voltage,  $U^N$  is the Nernst cell voltage and  $\eta_i$  are the polarisations to be described below. The effects of each polarisation and the range of current densities for which they occur can be seen in the typical IV curve shown in Fig. 2.8.

### **Concentration Polarisations.**

Concentration polarisations are voltage reductions due to slow mass transport through the porous anode or cathode. It is obvious to note that the concentration within the porous media is much less than that of the gas channel and that there is a significant mass transport gradient between the two. We can calculate the concentration overpotential by examining the voltage reduction between the gas channel region and the reaction,

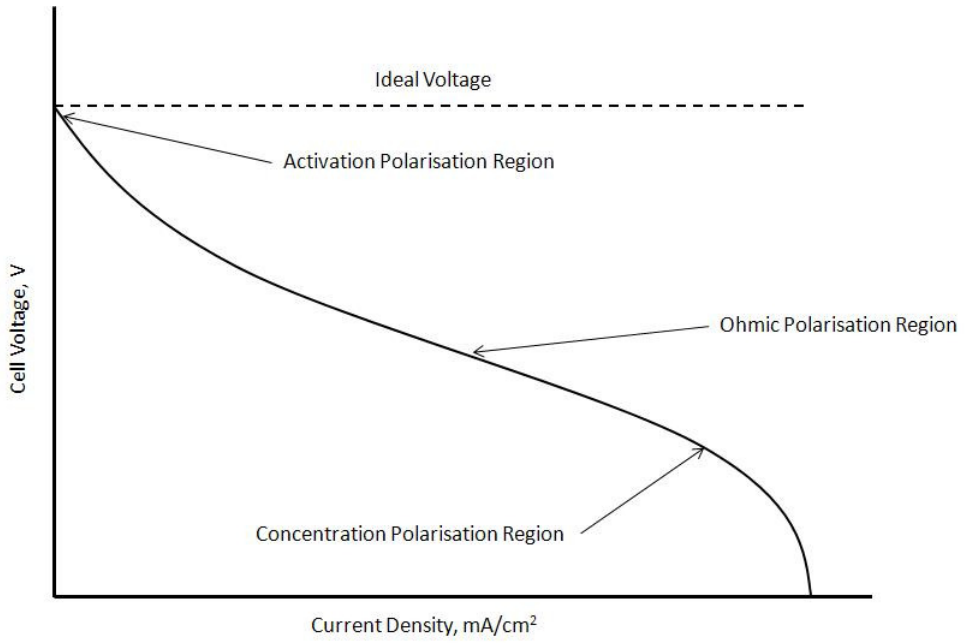


Figure 2.8: Typical profile of actual fuel cell voltage.

or porous anode, region (Bove & Ubertini, 2006)

$$\eta_{conc} = OCV_{bulk} - OCV_{react} = \frac{RT}{zF} \ln \left( \frac{P_{H_2}^{bulk} P_{H_2O}^{react}}{P_{H_2}^{react} P_{H_2O}^{bulk}} \right) + \frac{RT}{2zF} \ln \left( \frac{P_{O_2}^{bulk}}{P_{O_2}^{react}} \right) \quad (2.14)$$

where the term “bulk” refers to the gas channel region and the term “react” refers to the reaction region.

### Ohmic Polarisations.

Ohmic losses, or polarisations, occur due to a resistance against the movement of ions and electrons through their respective conducting media. Electrolytes provide resistance against ionic movement, and therefore reducing the distance between the electrodes will reduce the polarisation effect. The ohmic losses can be expressed in terms of current and resistance by

$$\eta_{ohm} = iR_c, \quad (2.15)$$

where  $i$  is current, and  $R_c$  is the total cell resistance. The total cell resistance includes the electronic, ionic, and contact resistances

$$R_c = R_{electronic} + R_{ionic} + R_{contact}. \quad (2.16)$$

Depending on the design of the fuel cell, each of the above could be the dominant ohmic resistance.

### **Activation Polarisations.**

Activation polarisations occur at the electrode/electrolyte interface and are a result of electrochemical reaction steps. Each electrochemical reaction has an associated activation energy, being the minimum energy required for a reaction to begin. Every electrochemical reaction step can have a different activation energy and reaction rate, and this is what dictates the voltage drop on the specific electrode. The activation polarisation is related to the current via the Butler-Volmer equation, which takes a separate form for the anode and cathode (Aguiar *et al.*, 2004)

$$j = j_{0,electrode} \left[ \exp\left(\frac{\alpha zF}{RT} \eta_{act,electrode}\right) - \exp\left(-\frac{(1-\alpha)zF}{RT} \eta_{act,electrode}\right) \right], \quad (2.17)$$

where  $j_0$  is the exchange current density,  $\alpha$  is the transfer coefficient with  $0 \leq \alpha \leq 1$  and  $\eta_{act}$  is the activation polarisation. The exchange current density can be represented in several ways (Aguiar *et al.* (2004), Costamagna *et al.* (2004), Newman & Thomas-Alyea (2004)).

## 2.7 Aims and Objectives

We have given an overview of the current literature within the field of fuel cell modelling. A limitation of current modelling is the lack of rigorous mathematical methodologies in the construction, analysis and numerical solutions of SOFCs. This leads to a system which does not fully account for the natural phenomena occurring with a fuel cell, particularly within the fluid flow. Hence, solutions are obtained based on equations which cannot be defined as accurate within the full model. Moreover, complex model constructions and limited mathematical analysis lead to high computational times in calculating a numerical solution to the problem. This is not only an inefficient method for computing a solution but also does not align with the commercial requirement of producing accurate solutions quickly.

The aims of this thesis are to construct a model for a planar SOFC from first principles applying the necessary model equations. The purpose of this is to construct an analytical framework to accurately model the natural phenomena occurring in SOFC flow fields and chemical reactions. From this we can construct a numerical framework which can compute highly accurate solutions in a matter of seconds or low level minutes. This analytical and numerical framework will then be applied to a more complex system more indicative of an operating SOFC to give solutions which are almost exactly comparable with experimental data.

This modelling approach and analysis will provide several important benefits and additions to the literature on fuel cell modelling. The first of these is that the approach will provide solutions which can be viewed with confidence as they have taken into account complications within the flow and reactions. Further to this, first principles modelling will allow us to examine the influence that certain model parameters have on numerical results. This informs the reader of the most important fuel cell parameters and the

influence they have on an operational cell. Finally the numerical efficient model will align with the industrial demand to obtain accurate fuel cell results very quickly. This is an important result for the progression of fuel cells in commercial markets and will aid the implementation of fuel cells into current markets.

# CHAPTER 3

## HETEROGENEOUS REACTION IN BOUNDARY-LAYER FLOW WITH ELECTROCHEMISTRY

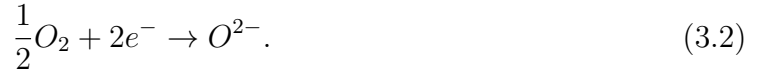
### 3.1 Model description

In this chapter we wish to formulate a model for the full set of reactions within a planar SOFC. Fig. 3.1 shows the full SOFC structure including inlet flows and mobile ion transfer. The model and flow setup which we consider in this chapter is a reduced form of the overall SOFC and is depicted in Fig. 3.2. The input flow to the anode is considered to be humidified hydrogen, which consists of 97% hydrogen and 3% water, with the flow mixture pre heated to 1000K as it approaches the anode. The first-order step reaction which will be considered within this model is given by



This reaction is more commonly known as the hydrogen oxidation reaction (HOR) and can only occur in the presence of oxygen ions. We will assume that this reaction only

occurs along the substrate and that no homogeneous reaction is present. These oxygen ions are conducted from the cathode through a solid electrolyte, where they are generated in a separate reaction known as the oxygen reduction reaction (ORR)



Zirconia promotes the conduction of oxygen ions at high temperatures which makes it an attractive material to use (Kawada & Yokokawa, 1996), and one which we will assume for our substrate in this model. It should be noted that the ORR can only take place in the presence of electrons transferred through an interconnect from the anode. Therefore, fuel cell operation can be thought of as a closed loop where the reaction rates are dependent on the electron (or ion) production and transport. The inlet mixture on the cathode side of the cell is taken to be air, where the only reacting component is that of oxygen. For this reason we assume the oxygen concentration to be constant on the cathode side and therefore we only need consider the anodic reaction within this model. Combining reactions (3.1) and (3.2) gives the full cell reaction



In the construction of this model we will make the following assumptions:

- The HOR reaction (3.1) will be assumed to be isothermal along the zirconia substrate;
- The substrate will be assumed to be flat, semi-infinite and impermeable;
- the initial flow will be of humidified hydrogen;
- The initial velocity is uniform as it approaches the plate with velocity  $u = U_0$ , where  $u$  is the streamwise velocity component;

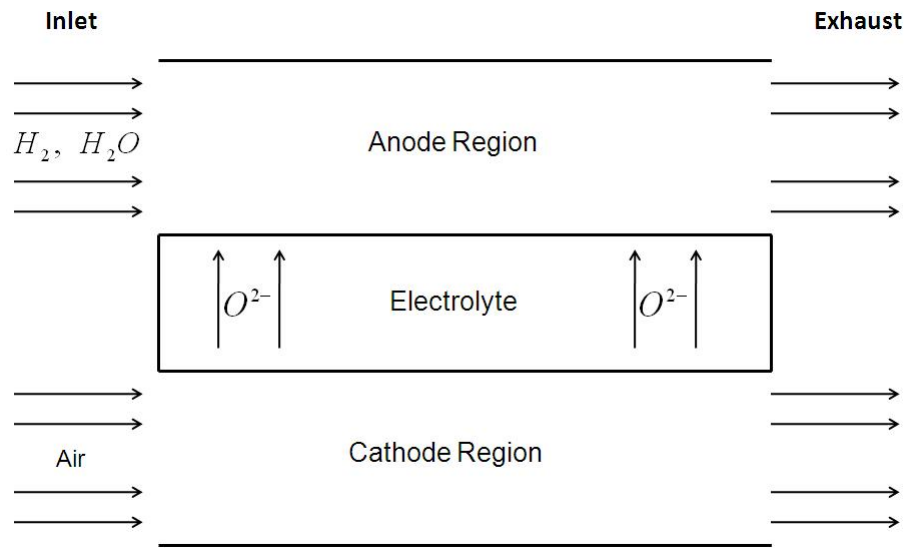


Figure 3.1: A diagram of a full SOFC setup including inlet flows and mobile ion transfer. The cell reactions occur on the boundaries between the electrodes and the electrolyte.

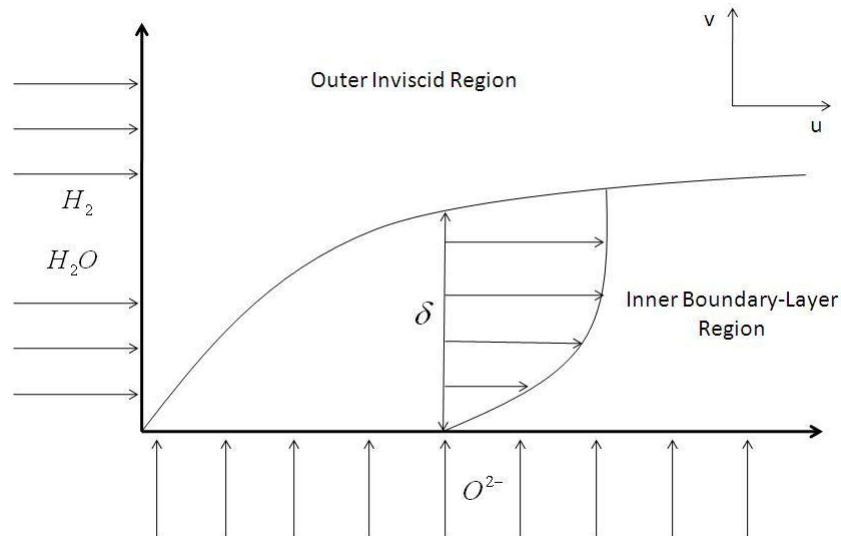


Figure 3.2: A diagram of the flow in the anode of a planar SOFC, with the coordinate system shown. A schematic of the boundary layer formation within this region is also shown.

- The length of the plate will be assumed to be  $L$ ;
- The flow has a constant mixture density, yielding an incompressible flow;
- Constant pressure;
- Non-zero viscosity resulting in a boundary-layer forming across the plate, proceeding from the leading edge;
- The flow is operating under steady state conditions and is therefore well mixed in the uniform stream before it reaches the plate.

The assumption that the model will consider the HOR under isothermal conditions requires some explanation before we can accept it as valid. Temperature variations occur throughout every fuel cell due to the exothermic and endothermic nature of the reactions present. However, within an SOFC we have an extremely high operating temperature, usually around 1000K. Therefore, even the largest variations in temperature are likely to seem negligible when looking at the spatial temperature of the whole cell. Fig. 3.3 (Cooper *et al.*, 2000) shows how the temperature profile within the reaction region is close to isothermal with respect to the overall operating temperature.

## 3.2 A mathematical model for mass and momentum conservation

We now consider establishing a mathematical model for the conservation of mass and momentum within the bulk region of our domain. We can calculate the velocity throughout the flow through solving the conservation of momentum equation, which is given by

$$\frac{\partial \mathbf{u}}{\partial t} + (\mathbf{u} \cdot \nabla) \mathbf{u} = -\frac{\nabla p}{\rho} + \nu \nabla^2 \mathbf{u}, \quad (3.4)$$

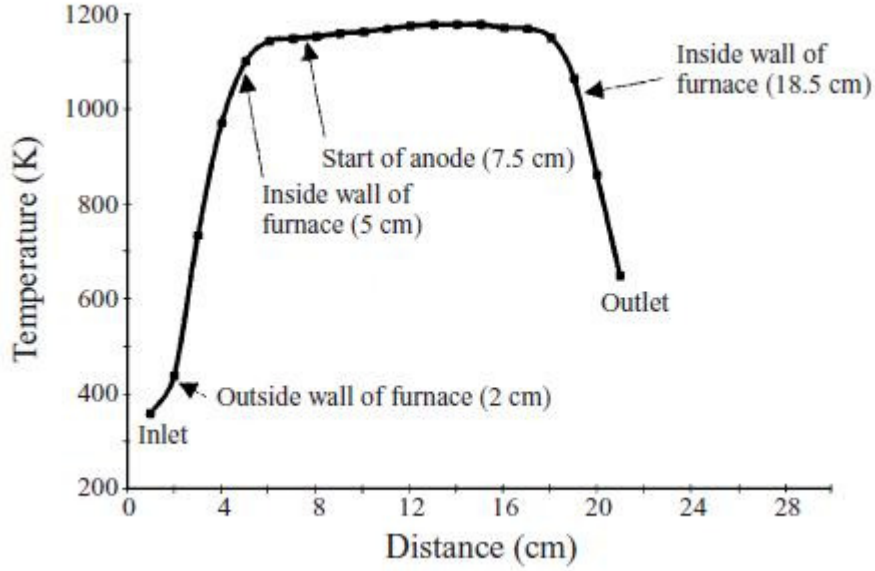


Figure 3.3: Temperature profile along the axis of an SOFC operating at 1173K (Cooper *et al.*, 2000). This demonstrates an almost constant temperature, relative to the inlet temperature, throughout the anode region

where  $\mathbf{u}$  is the two dimensional velocity vector,  $p$  is the pressure and  $\nu$  is the kinematic viscosity. For more details regarding the construction and theoretical meaning of (3.4) we point the reader in the direction of Acheson (1990). Here we will only be considering the steady state case and thus the first term in (3.4) is neglected. Since we assume that the plate is coated with a catalyst, which leads to a reaction on the plate, it is the dynamics near the surface of the plate which we consider in detail here. Near the plate the equations of motion simplify into the boundary-layer equations, see section 2.5, appendix A, Prandtl (1904) and Blasius (1908) for analysis and construction. For simplicity we will state these equations

$$u \frac{\partial u}{\partial x} + v \frac{\partial u}{\partial y} = \nu \frac{\partial^2 u}{\partial y^2}, \quad (3.5)$$

where  $u$  and  $v$  are the streamwise and transverse velocity components, respectively, and  $x$  and  $y$  are the streamwise and transverse coordinates to the plate.

When dealing with the mass conservation we chose to work with the mass fraction  $Y_i$  of each of the reactant and product species. We are able to relate the mass fraction of the species to its concentration  $C_i$ , molecular mass  $m_i$  and the total mixture density  $\rho$  by

$$Y_i = \frac{m_i C_i}{\rho}, \quad (3.6)$$

Since we are only dealing with two species we can denote the subscript  $i$  by the following: H(hydrogen) and W(water). Due to the high temperatures reached in the operation of the cell we assume that the species remain in gas phase throughout the flow. The general expression for the conservation of mass is

$$\nabla \cdot (\rho \mathbf{u}) = 0, \quad (3.7)$$

where the right hand side is set to zero since there is no homogeneous reaction taking place. Since we are assuming an incompressible flow this enables us to reduce this equation to the volumetric continuity equation

$$\nabla \cdot \mathbf{u} = 0. \quad (3.8)$$

The conservation of mass equation for each of the chemical species in question is given by

$$\nabla \cdot (\rho Y_i \mathbf{u}_i) = \omega_i, \quad (3.9)$$

where  $\mathbf{u}_i$  is the velocity of species  $i$  and  $\omega_i$  is the rate of consumption of species  $i$ . Since there are no homogeneous reactions within our model we can assume that  $\omega_i = 0$ . By introducing the relationship

$$\mathbf{U}_i = \mathbf{u}_i - \mathbf{u}, \quad (3.10)$$

where  $\mathbf{U}_i$  is the diffusion velocity of species  $i$  and  $\mathbf{u}$  is the mixture velocity. The conservation of mass equation (3.9) becomes

$$\nabla \cdot [\rho Y_i (\mathbf{U}_i + \mathbf{u})] = 0 \quad (3.11)$$

Performing the differentiation within (3.11) and satisfying the volumetric continuity equation (3.8) we obtain

$$\nabla \cdot (\rho Y_i \mathbf{U}_i) + \rho (\mathbf{u} \cdot \nabla) Y_i = 0 \quad (3.12)$$

and if we apply Fick's law of diffusion to (3.12) we obtain the conservation of mass for the species within the bulk mixture

$$(\mathbf{u} \cdot \nabla) Y_i = D_i \nabla^2 Y_i \quad (3.13)$$

This equation is valid for all species considered within this model.

### 3.3 Model electrochemistry

In chapter 2 we gave some details for the generic electrochemistry involved in fuel cell operation. It is now necessary to apply this theory towards the current model which we are examining.

Within the cell we will make the assumption that the cell potential is a variable. For the purpose of modelling we can take either the cell potential or the current density as our electrochemical variable. However, during fuel cell operation it is common to set the cell potential to the desired level and then measure the current density output. Thus, the cell potential is the appropriate choice to take as our variable.

The current density of the cell is proportional to the ion flux rate since the ion flux rate determines the electron production rate through reaction (3.1). This relationship is

given by

$$i(x) = 2Fq_e(x), \quad (3.14)$$

where  $F$  is the Faraday constant,  $i(x)$  is the local current density and  $q_e(x)$  is the local ion flux rate. The factor  $2F$  corresponds to the number of electrons transferred per mole of hydrogen multiplied by the magnitude of electric charge per mole of electrons. We now introduce the Nernst Potential, or reversible potential, for the full cell reaction (3.3), which is given by

$$U^N = U^r + \frac{RT}{2F} \ln \left( \frac{P_H P_O^{\frac{1}{2}}}{P_W} \right), \quad (3.15)$$

where  $U^r$  is the ideal potential,  $R$  is the gas constant,  $T$  is the absolute temperature and  $P_i$  is the partial pressure of the  $i^{th}$  species. If we assume that the species satisfy a gas law of the form  $P_i = \rho RT Y_i / m_i$ , where  $\rho$  is the mixture density and  $m_i$  is the molecular mass of the  $i^{th}$  species, then we obtain the reversible potential for the anode of the cell, given by

$$U^N = U^r + \frac{RT}{2F} \ln \left( \frac{Y_H Y_O^{\frac{1}{2}} m_W (\rho RT)^{\frac{1}{2}}}{Y_W m_H m_O^{\frac{1}{2}}} \right) \quad (3.16)$$

$Y_O$  is a constant equal to the mass fraction of oxygen in air, which we will take to be  $Y_O = 0.23$ . The Nernst potential (3.16) does not take into account losses in potential due to non-uniform cell fabrication and species transport during operation. These losses are the cell overpotentials and including these within the potential equation give us an overall cell potential

$$U_{cell} = U^N - \sum_i \eta_i, \quad (3.17)$$

where  $\eta_i$  are the overpotentials. In the case of this model we will assume that the activation and concentration overpotentials are negligible due to the restriction that the reaction occurs on a flat substrate rather than inside a porous medium. Therefore, we write the total cell potential as

$$U_{cell} = U^N - i(x)R_s, \quad (3.18)$$

where the term  $i(x)R_s$  corresponds to an ohmic overpotential and  $R_s$  is the specific resistance of the substrate to the ion conduction. We may now write the ion flux rate variable  $q_e(x)$  as

$$q_e(x) = \frac{RT}{4F^2 R_s} \left[ \ln \left( \frac{Y_H Y_O^{\frac{1}{2}}}{Y_W} \right) + \ln \left( \frac{m_W (\rho RT)^{\frac{1}{2}}}{m_H m_O^{\frac{1}{2}}} \right) + \frac{2F}{RT} (U^r - U_{cell}) \right] \quad (3.19)$$

We now have an expression for the flux density of ions in terms of the mass fractions of the species and the cell potential. Thus we have a direct link between measuring the current density of the cell for varying values of the cell potential.

### 3.4 Boundary conditions

We now look to establish an accurate set of boundary conditions which depict the flow and reaction within the model. The input gas consists of humidified hydrogen and the flow is assumed to be uniform, with respect to the streamwise coordinate. Hence, the input boundary conditions are given by

$$Y_H = \tilde{Y}_H, \quad Y_W = \tilde{Y}_W, \quad u = U_0, \quad v = 0 \quad \text{on} \quad x = 0, \quad y > 0, \quad (3.20)$$

where  $\tilde{Y}_H$  and  $\tilde{Y}_W$  represent the input mass fractions of hydrogen and water, respectively. The boundary conditions far from the plate can be represented by

$$Y_H \rightarrow \tilde{Y}_H, \quad Y_W \rightarrow \tilde{Y}_W, \quad u \rightarrow U_0, \quad v \rightarrow 0 \quad \text{as} \quad y \rightarrow \infty, \quad x > 0 \quad (3.21)$$

Due to the non-zero viscosity of the fluids, we have a no-slip condition at the plate for the velocity

$$u = 0, \quad v = 0 \quad \text{on} \quad y = 0, \quad x > 0 \quad (3.22)$$

Further to these conditions we introduce a continuity condition on the mass fractions of the species

$$\sum_i Y_i = 1 \quad \text{and} \quad \sum_i \frac{\partial Y_i}{\partial y} = 0, \quad (3.23)$$

which imposes an initial mass fraction condition of

$$\tilde{Y}_H + \tilde{Y}_W = 1 \quad (3.24)$$

We have yet to introduce conditions for the mass-flux boundary conditions at the plate. At each point along the surface of the plate the amount of each reactant or product species must be equally balanced by the amount transported through normal diffusion. The reaction rates of the species are proportional to the current density, as can be seen in Bove & Ubertini (2006). Therefore, we introduce the mass-flux boundary conditions

$$D_H \frac{\partial Y_H}{\partial y} = \frac{q_e(x)m_H}{\rho}, \quad (3.25)$$

$$D_W \frac{\partial Y_W}{\partial y} = - \frac{q_e(x)m_W}{\rho}, \quad (3.26)$$

We can see that, as described in section 3.3, the reaction rate term has a significant dependence on the current density, in the form of the ion flux density.

### 3.5 Non-dimensionalisation

We have now established the model for the governing equations of the flow (3.5), (3.8) and (3.13) along with their corresponding boundary conditions (3.20)-(3.22),(3.25) and (3.26) in dimensional form. We therefore introduce the following non-dimensional variables

$$\begin{aligned}\overline{m_i} &= \frac{m_i}{m_H}, \quad \bar{\rho} = \frac{\rho}{\rho_{in}}, \quad u = U_0 \bar{u}, \quad v = U_0 Re^{-\frac{1}{2}} \bar{v}, \quad \bar{x} = \frac{x}{L}, \quad \bar{y} = \frac{y Re^{\frac{1}{2}}}{L}, \\ \bar{q}_e(x) &= \frac{4F^2 R_s}{RT} q_e(x), \quad Re = \frac{U_0 L}{\nu}\end{aligned}\quad (3.27)$$

where we use the length,  $L$ , of the plate to nondimensionalise spatial coordinates, the velocity,  $U_0$ , at the inlet of the plate to nondimensionalise the velocity components and include a factor of  $Re^{\frac{1}{2}}$  to take into account the length of the boundary-layer within the normal velocity and spatial components. Applying these new variables transforms the ion flux rate to give (on dropping the bars from here on in for convenience)

$$q_e(x) = \ln \left( \frac{Y_H Y_O^{\frac{1}{2}}}{Y_W} \right) + \sigma \quad (3.28)$$

where  $\sigma$  is a non-dimensional parameter defined to be

$$\sigma = \ln \left( \frac{m_W (\rho_{in} RT)^{\frac{1}{2}}}{m_H^{\frac{1}{2}} m_O^{\frac{1}{2}}} \right) + \frac{2F}{RT} (U^r - U_{cell}) \quad (3.29)$$

Under the assumption that the flow is incompressible we have the  $\bar{\rho} = 1$ . We are now able to obtain dimensionless equations for the momentum and mass conservation within the model, given by

$$\frac{\partial u}{\partial x} + \frac{\partial v}{\partial y} = 0, \quad (3.30)$$

$$u \frac{\partial u}{\partial x} + v \frac{\partial u}{\partial y} = \frac{\partial^2 u}{\partial y^2}, \quad (3.31)$$

$$u \frac{\partial Y_H}{\partial x} + v \frac{\partial Y_H}{\partial y} = \frac{1}{S_c} \frac{\partial^2 Y_H}{\partial y^2}, \quad (3.32)$$

$$u \frac{\partial Y_W}{\partial x} + v \frac{\partial Y_W}{\partial y} = \frac{\delta}{S_c} \frac{\partial^2 Y_W}{\partial y^2}, \quad (3.33)$$

where  $S_c$  is defined to be the Schmidt number, with  $S_c = \nu/D_H$ . The Schmidt number measures the ratio between viscous and diffusive terms throughout the flow domain. The value of the Schmidt number must be at *least*  $\mathcal{O}(1)$  within the boundary-layer region, since viscous terms will dominate that of diffusion. Outside of the boundary-layer we would expect the Schmidt number to be at *most*  $\mathcal{O}(1)$  since diffusion will now dominate the flow. The parameter  $\delta$  is a measure of the ratio between diffusive terms of the species and we define it to be  $\delta = D_W/D_H$ . The Reynolds number,  $Re$ , is large in this case which also reduces the equations of motion into the boundary-layer equations. The dimensionless boundary conditions for the mass-flux at the plate take the form

$$\frac{\partial Y_H}{\partial y} = Re^{-\frac{1}{2}} E q_e(x), \quad (3.34)$$

$$\frac{\partial Y_W}{\partial y} = - \frac{Re^{-\frac{1}{2}} E q_e(x) m_W}{\delta} \quad (3.35)$$

where we define the dimensionless parameter  $E$  to be

$$E = \frac{LRTm_H}{4F^2 R_s \rho_{in} D_H} \quad (3.36)$$

If we sum (3.34) and (3.35) we see that the left hand side becomes zero due to (3.23). Therefore, in order to balance the summation of the reaction terms we require that  $m_W/\delta = 1$  which implies that  $\delta = 9$ . Taking the value  $\delta = 9$  should be considered as a model requirement and not something that will always be physically represented in empirical work. The reason for this is due to the model not considering the mass of oxygen on the anode side of the cell. Therefore, in operational cells there is a creation of oxygen mass within the anode which will effect the mass balance condition and hence the value of  $\delta$ . The remaining dimensionless boundary conditions are given by

$$Y_H = \tilde{Y}_H, \quad Y_W = \tilde{Y}_W, \quad u = 1, \quad v = 0 \quad \text{on} \quad x = 0, \quad y > 0 \quad (3.37)$$

$$Y_H \rightarrow \tilde{Y}_H, \quad Y_W \rightarrow \tilde{Y}_W, \quad u \rightarrow 1, \quad v \rightarrow 0 \quad \text{as} \quad y \rightarrow \infty, \quad x > 0 \quad (3.38)$$

$$u = 0, \quad v = 0 \quad \text{on} \quad y = 0, \quad x > 0 \quad (3.39)$$

### 3.6 Outer region as $Re \rightarrow \infty$

We now seek a solution for the outer inviscid region within the flow. Since there is no homogeneous reaction present within our model, the species present within the region outside the boundary-layer are only subject to convection and diffusion. Moreover, we may assume that within this region there is no feedback from the heterogeneous reaction (3.1) into the bulk flow. Therefore, within the outer region we drop the mass-flux boundary conditions (3.34), (3.35) and (3.39). As a result we can obtain an exact solution within this region, given by

$$u = 1, \quad v = 0, \quad Y_H = \tilde{Y}_H, \quad Y_W = \tilde{Y}_W \quad (3.40)$$

The outer solution represents a uniform flow of reactants without the presence of a reaction. This exactly conforms with the fact that the outer solution is outside of the boundary-layer region and is not affected by the heterogeneous reaction.

### 3.7 Inner region as $Re \rightarrow \infty$

Due to the heterogeneous reaction, within the inner region of the boundary layer we are required to satisfy the above dropped conditions. Therefore, we seek a solution to equations (3.30)-(3.33) subject to the boundary conditions (3.34)-(3.39). Hence, we make a transformation inspired by the Blasius solution (Blasius, 1908; Meksyn, 1961)

$$\psi = \xi^{\frac{1}{2}} f(\eta), \quad \text{with} \quad \eta = \frac{y}{x^{\frac{1}{2}}} \quad \text{and} \quad \xi = x, \quad (3.41)$$

where the stream function  $\psi$  is defined by

$$u = \frac{\partial \psi}{\partial y}, \quad v = -\frac{\partial \psi}{\partial x} \quad (3.42)$$

In deriving an expression for  $\psi$  we have used the theory of self similar solutions. Self similar (or similarity) solutions arise from the velocity component  $u$  having the same scaled profile as some common form along any transverse section at every point along  $x$ . The concept of similarity and derivation of the similarity variable can be found in appendix B, with some classical problems and solutions found in Rosenhead (1963). One direct consequence of introducing the stream function is that the volumetric continuity equation (3.30) is automatically satisfied. Applying this transformation to the momentum equation (3.31) yields the Blasius equation

$$f''' + \frac{1}{2} f f'' = 0 \quad (3.43)$$

where the primes denote differentiation with respect to the similarity variable  $\eta$ . The boundary conditions for momentum, under this transformation, become

$$f'(\infty) = 1, \quad f(0) = f'(0) = 0 \quad (3.44)$$

It should be noted here that the equation and boundary conditions for  $f$  are completely decoupled from the mass fractions of the species. Therefore, a solution for the values of  $f$  can be obtained independently without consideration for the conservation of mass equations and boundary conditions.

We now seek to apply this transformation to the conservation of mass equations (3.32) and (3.33) and the mass-flux boundary conditions (3.34) and (3.35). It must be stated here that we only need consider the solution for one of the species since the other solution can be obtained from (3.23). Henceforth, we will only consider the solution for  $Y_H$ . To obtain the transformed equations we must note the coordinate transformation for the mass fraction of species

$$Y_i = Y_i(\xi, \eta) \quad (3.45)$$

and the transformation (3.41) alters the derivatives with respect to  $x$  and  $y$  via

$$\frac{\partial Y_i}{\partial y} = \frac{\partial \eta}{\partial y} \frac{\partial Y_i}{\partial \eta}, \quad \frac{\partial Y_i}{\partial x} = \frac{\partial \xi}{\partial x} \frac{\partial Y_i}{\partial \xi} + \frac{\partial \eta}{\partial x} \frac{\partial Y_i}{\partial \eta} \quad (3.46)$$

Therefore, under this transformation we obtain the conservation of mass equation

$$\frac{1}{S_c} \frac{\partial^2 Y_H}{\partial \eta^2} + \frac{1}{2} f \frac{\partial Y_H}{\partial \eta} - x \frac{df}{d\eta} \frac{\partial Y_H}{\partial \xi} = 0 \quad (3.47)$$

subject to the mass-flux boundary condition

$$\frac{\partial Y_H}{\partial \eta} = \xi^{\frac{1}{2}} Re^{-\frac{1}{2}} E q_e(\xi), \quad (3.48)$$

and the remaining boundary conditions

$$Y_H = \tilde{Y}_H \quad \text{on} \quad \xi = 0, \quad \eta > 0 \quad (3.49)$$

$$Y_H \rightarrow \tilde{Y}_H \quad \text{as} \quad \eta \rightarrow \infty, \quad \xi > 0 \quad (3.50)$$

We have established the transformed equations and boundary conditions which we are required to solve. We now wish to construct a set of equations to solve for the mass fractions of species around the point of singularity within the flow.

### 3.7.1 Asymptotic solution for $\xi \ll 1$

We seek a solution to equations (3.47)-(3.50) for small values of  $\xi$  close to the leading edge of the plate. The point  $\xi = 0$  is a singularity within the flow since this is where the uniform stream initially contacts the stationary plate. Therefore, this is the point where the velocity changes from the free stream velocity to zero instantaneously. We note from (3.28) that  $q_e(\xi) \sim \mathcal{O}(1)$  and so the boundary condition (3.48) suggests that we should look for an expansion of the form

$$Y_H(\xi, \eta) = a_0 + \xi^{\frac{1}{2}} a_1(\eta) + \xi a_2(\eta) + \xi^{\frac{3}{2}} a_3(\eta) + \dots, \quad (3.51)$$

where the functions  $a_i$  are  $\mathcal{O}(1)$  as  $\xi \rightarrow 0$  and  $a_0 = \tilde{Y}_H$ , which can be shown from the initial condition for  $Y_H$  at the inlet (3.49). Since we introduced the continuity condition (3.23) we are only required to solve for  $Y_H$ , from which we can calculate  $Y_W$  via

$$Y_W = 1 - Y_H \quad (3.52)$$

Therefore, we concentrate our attention on obtaining an asymptotic solution for the values of  $a_i(\eta)$  and solve for  $Y_W$  once we have the solution for  $Y_H$ . Substituting the expansion (3.51) into the conservation of mass equation (3.47) yields the following system of equations in ascending orders of  $\xi$ , for  $\mathcal{O}(\xi^{\frac{1}{2}})$ ,  $\mathcal{O}(\xi)$  and  $\mathcal{O}(\xi^{\frac{3}{2}})$

$$\frac{1}{S_c}a_1'' + \frac{1}{2}fa'_1 - \frac{1}{2}f'a_1 = 0, \quad (3.53)$$

$$\frac{1}{S_c}a_2'' + \frac{1}{2}fa'_2 - f'a_2 = 0, \quad (3.54)$$

$$\frac{1}{S_c}a_3'' + \frac{1}{2}fa'_3 - \frac{3}{2}f'a_3 = 0, \quad (3.55)$$

subject to the mass-flux boundary conditions, again given in ascending orders of  $\xi$

$$a'_1(0) = Re^{-\frac{1}{2}}E \left( a_0 + \frac{1}{2}a_0^2 + \frac{1}{2}\ln(Y_O) + \sigma \right), \quad (3.56)$$

$$a'_2(0) = Re^{-\frac{1}{2}}E \left( \frac{a_1(0)}{a_0} + a_1(0) + a_0a_1(0) \right), \quad (3.57)$$

$$a'_3(0) = Re^{-\frac{1}{2}}E \left( \frac{a_2(0)}{a_0} - \frac{a_1^2(0)}{2a_0^2} + a_2(0) + \frac{a_1^2(0)}{2} + a_2(0)a_0 \right), \quad (3.58)$$

and the far field conditions

$$a_1(\eta) \rightarrow 0, \quad a_2(\eta) \rightarrow 0, \quad a_3(\eta) \rightarrow 0 \quad \text{as} \quad \eta \rightarrow \infty \quad (3.59)$$

It should be stated that (3.43), (3.44) and (3.53)-(3.59) constitute a set of boundary value problems for the momentum and different orders of the mass fraction of hydrogen in (3.51). All of these equations must be solved together in order to obtain a solution for  $Y_H$  and subsequently  $Y_W$ . We solve the boundary value problems at each order using the shooting method where the parameter and dimensionless parameter values are given in

Parameter	Symbol	Value	Units
Molar mass of chemical species	$m_i$	$m_H=0.002$ $m_W=0.018$	$kg\ mol^{-1}$ $kg\ mol^{-1}$
Inlet mass fractions of species	$\tilde{Y}_i$	$\tilde{Y}_H = 0.97$ $\tilde{Y}_W = 0.03$	
Hydrogen diffusivity	$D_H$	$10^{-4}$	$m^2\ s^{-1}$
Faraday's constant	$F$	96485	$C\ mol^{-1}$
Gas constant	$R$	8.314	$J\ K^{-1}\ mol^{-1}$
Temperature	$T$	1000	$K$
Input gas density	$\rho_{in}$	$O(10^{-1})$	$kg\ m^{-3}$
Anode length	$L$	$O(10^{-1})$	$m$
Specific resistance of zirconia	$R_s$	$1.707 \times 10^{-4}$	$\Omega\ m^2$
Viscosity	$\mu$	$4.606 \times 10^{-5}$	$kg\ m^{-1}\ s^{-1}$
Inlet velocity	$U_0$	$O(10^{-1}) - O(1)$	$m\ s^{-1}$
Ideal potential	$U^r$	0.99	$V$
Cell potential	$U_{cell}$	0-1.2	$V$

Table 3.1: Parameters, their symbols, values and units

Tables 3.1 and 3.2. A plot representing the asymptotic solution for the mass fraction of hydrogen at the plate is shown in Fig. 3.4. A method for obtaining the full numerical solution is explained in the next section.

## 3.8 Numerical solution for $\xi = \mathcal{O}(1)$

Now we have established an asymptotic solution for the momentum and mass fractions around the point of singularity, we seek a full numerical solution for  $\xi = \mathcal{O}(1)$ . The asymptotic solution is no longer valid within this region so we require an alternate solution to the equations and boundary conditions (3.43)-(3.50).

### 3.8.1 Numerical method

#### Numerical Method Review

Before we construct the appropriate numerical method for the above model it is worth giving details regarding the options available including details of the benefits and drawbacks

Symbol	Typical value	Description
$Re$	$O(10^2)$	Reynolds Number = $\frac{\text{inertial forces}}{\text{viscous forces}}$
$S_c$	$O(1)$	Schmidt number = $\frac{\text{viscous forces}}{\text{diffusive forces}}$
$\sigma$	$24.65 - (-3)$	
$E$	0.02	$\frac{\text{electrochemical flux of hydrogen}}{\text{diffusive flux of hydrogen}}$

Table 3.2: Definitions of dimensionless parameters and their typical values

of each.

A review of numerical methods for non-linear PDEs was conducted by Tadmor (2012). The methods for consideration were finite difference (FDM), finite element (FEM) and finite volume (FVM). The benefits of the FDM are its versatility, easy of use, applicability to the full spectrum of linear and non linear PDEs and is considered an ideal method for boundary value problems (like those considered within this model). Due to its construction, the FDM becomes difficult to use within complex geometries. The FEM has advantages in complex geometries due to its flexibility in grid construction. The applicability of the FEM is to boundary value PDEs which are expressed in different formations (weak, saddle point etc). The FVM utilised the same grid construction as FEM but works with cell averages rather than cell nodes. Once again this method is very versatile to complex geometries. Although the FEM and FVM methods have advantages, they are more computationally inefficient compared to the FEM method

Arima (2006) presented a numerical method for a chemically reacting fluid flow incorporating density and thermal variations. The method was based on a forward finite-difference Crank-Nicholson method alongside the Newton-Raphson method for convergence of a solution. The numerical scheme was validated for varying density values. Therefore, a method aligning to this would be appropriate for compressible models.

In Peters (1976) the authors examined a model of the hydrogen-oxygen diffusion flame in a flat boundary layer. It was found that for high Damkohler numbers (ratio of reac-

tion rate to convective mass transport) only a Newton-Raphson iteration within a finite difference discretisation gave satisfactory results. The hydrogen oxidation reaction has been shown to have a very fast reaction rate (Ó Conaire *et al.*, 2004) and so within this reaction high Damkohler numbers are present. Therefore, this is an approach we can feel confident with using within our model.

### Numerical Framework Construction

In order to solve the system of equations and boundary conditions (3.43)-(3.50) for larger values of  $\xi$  we are required to implement a numerical scheme. As with all numerical methods, we desire one which is not only computationally efficient but also has a high order of accuracy. We can see from the above model equations that we do not have a full set of boundary conditions for the domain. More specifically, we do not have a boundary condition for the velocity and mass fractions at the end of the plate, or outlet of the flow (as  $\xi \rightarrow \infty$ ). Therefore, in order to solve the above system of equations we are required to implement a numerical step-by-step method, also known as a marching scheme. For our model, the numerical marching scheme method begins at the leading edge, or inlet of the flow, and progresses along the  $\xi$  coordinate until the end of the plate, for a desired length scale in  $\xi$ . At each point along the  $\xi$  coordinate we adopt Newton's method along the points in  $\eta$  to find a convergent solution. Once a convergent solution has been found, to within a degree of accuracy at our disposal, we then move onto the next point along  $\xi$  and use an identical method, until we reach our desired end value. The iterative parameter, which is used to alter the values at the grid points along  $\eta$  on each iteration, is used as a tolerance of convergence, where we take the difference between two sets of iterations to be at most  $\mathcal{O}(10^{-3})$ , say.

To numerically solve the model within our relevant domain we first must establish a numerical grid and define grid nodes at which the model equations can be solved. We do this by implementing a uniform grid with the  $\xi$  coordinate, where the grid nodes will be

separated by a grid step size of  $\Delta\xi$ , which we can vary for computational efficiency and accuracy. Due to the reaction occurring near the plate we expect significant variations in the mass fractions of species within this region. Therefore, a non-uniform grid with a greater amount of grid nodes close to the plate is more appropriate, with grid nodes becoming more sparse as  $\eta \rightarrow \infty$ . To do this we introduce an initial grid step size  $\Delta\eta_1$ , at the plate, where each subsequent grid step size is calculated via

$$\Delta\eta_{j+1} = k\Delta\eta_j, \quad (3.60)$$

where  $k$  is an amplification factor, which we take as  $k > 1$ , and  $j$  is the suffix corresponding to the  $\eta$  coordinate. Using this method of grid step size generation results in adjacent grid step sizes increasing as we move further away from the wall whilst maintaining more grid points close to the plate compared with uniform grid generation. We can calculate the grid points along  $\eta$  by the relationship

$$\eta_{j+1} = \eta_j + \Delta\eta_j. \quad (3.61)$$

One drawback of using a non-uniform grid is the difficulty in discretising higher order equations, compared to using a uniform grid. However, since all equations are of maximum order 2 this should not be regarded as a time consuming process.

We have now established the basis for our numerical scheme and grid generation. It is now necessary to discretise our system of equations so that they can be solved numerically. To do this we use finite difference approximations in both coordinates. In the streamwise coordinate, since we are using a marching scheme, we adopt the forward finite difference method, given by

$$\frac{\partial F}{\partial \xi} = \frac{F_{i+1,j} - F_{i,j}}{\Delta\xi}, \quad (3.62)$$

where  $i$  is the suffix corresponding to the  $\xi$  coordinate and  $F$  is variable which is being discretised. Now, for the transverse coordinate  $\eta$  we have a full set of boundary conditions for each grid step  $i$  in  $\xi$ . Therefore, the first order derivative can be discretised using the central difference approximation

$$\frac{\partial F}{\partial \eta} = \frac{F_{i,j+1} - F_{i,j-1}}{\eta_{j+1} - \eta_{j-1}}. \quad (3.63)$$

When it comes to defining the second order derivative in the  $\eta$  coordinate we have to give more consideration to the non-uniform grid step size. This is because the second order derivative requires evaluation at 3 grid nodes when using a central difference approximation. Using 3 grid nodes means we have to consider 2 non-equal grid step sizes, making the discretisation slightly more difficult. Therefore, we express the second order derivative in  $\eta$  via the equation

$$\frac{\partial^2 F}{\partial \eta^2} = \frac{2}{\eta_{j+1} - \eta_{j-1}} \left[ \frac{F_{i,j+1} - F_{i,j}}{\eta_{j+1} - \eta_j} - \frac{F_{i,j} - F_{i,j-1}}{\eta_j - \eta_{j-1}} \right]. \quad (3.64)$$

The discretisations (3.63) and (3.64) are second order accurate which implies that the order of accuracy is  $\Delta\eta^2$ . In order to keep this order of accuracy within the surface boundary conditions we introduce the one-sided difference as the discretisation method along these points

$$\left. \frac{\partial F}{\partial \eta} \right|_{\eta=0} = \frac{-3F_{i,j} + 4F_{i,j+1} - F_{i,j-1}}{\eta_{j+1} - \eta_{j-1}}. \quad (3.65)$$

We have established the discretisations for the derivatives within our model. We can see that the discretisations in the  $\eta$  coordinate are second order accurate and are first order accurate within the  $\xi$  coordinate, due to the marching scheme. Therefore, to keep the level of accuracy high we require more grid points in the  $\xi$  coordinate. Furthermore, for convergence in the  $\eta$  coordinate we must be careful when setting the range of  $\eta$ . After

extensive numerical attempts it was determined that a value of  $\eta_{max} \approx 12$  was sufficiently large enough to produce convergent solutions.

### 3.9 Results and discussions

The above numerical method has been implemented and data has been extracted from this. Before we analyse this data it is worth stating that the efficiency of this model is to the order of seconds for both asymptotic and full numerical solutions on a single high-speed PC. This is a vast improvement to many numerical models where computational times have been reported to take 2-3 h working on 10 parallel machines or 10-15 h working on a single high-speed PC (Ju & Wang, 2004).

Fig. 3.4 is a plot of the numerical (full line) and asymptotic (broken line) solutions for the surface mass fraction of hydrogen. We can see from this plot that the two lines are in very good agreement and can be considered identical for  $0 \leq \xi \leq 1$  and certainly for small values of  $\xi$ , which is to be expected from the construction of the asymptotic solution. The main point to notice from this plot is the rapid reduction in the mass fraction of hydrogen close to the leading edge compared to further down the plate. This is to be expect as this is the region where we expect the ion flux density,  $q_e(\xi)$ , to be at its greatest.

A more detailed examination of the reaction rate of hydrogen along the surface of the plate can be found in Fig. 3.5. Here we have plotted the gradient of the mass fraction of hydrogen  $Y_H$  along the surface of the plate for a cell potential of  $U_{cell} = 0.5$ . We can see from the plot the severity of the reaction close to the leading edge of the plate. Moreover, this reaction rate very rapidly converges towards zero. The main reason for this is that the initial flow is a hydrogen rich stream but as we move along the plate this composition approaches a 50:50 hydrogen to water split. This reduces the presence of hydrogen along the surface of the cell which in turn will reduce the reaction rate of hydrogen.

In Fig. 3.7 we represent a more detailed view of the mass fraction of hydrogen as we

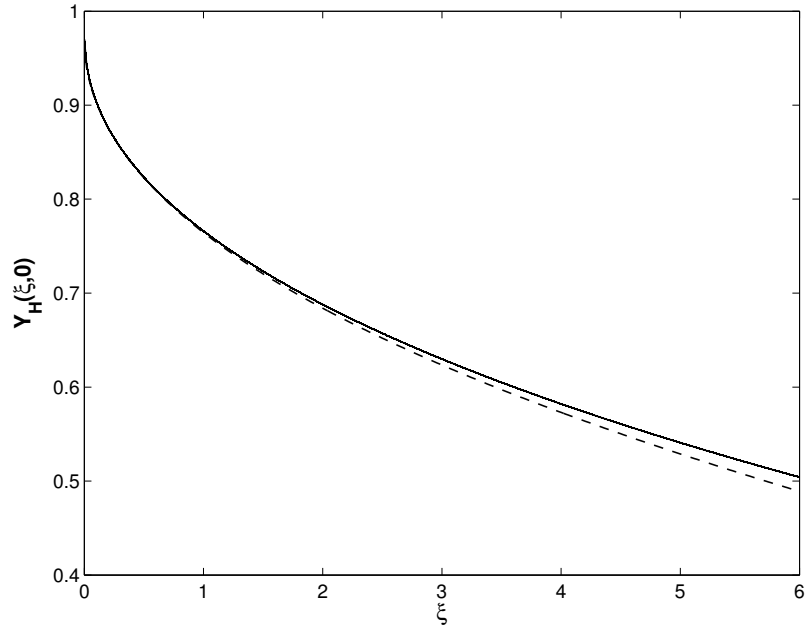


Figure 3.4: Comparison of numerical (full line) and asymptotic (broken line) solutions for  $Y_H(\xi, 0)$  when  $U_{cell} = 0.5$ . The result are closely matched for  $\xi \ll 1$  and diverge slightly as  $\xi$  increase.

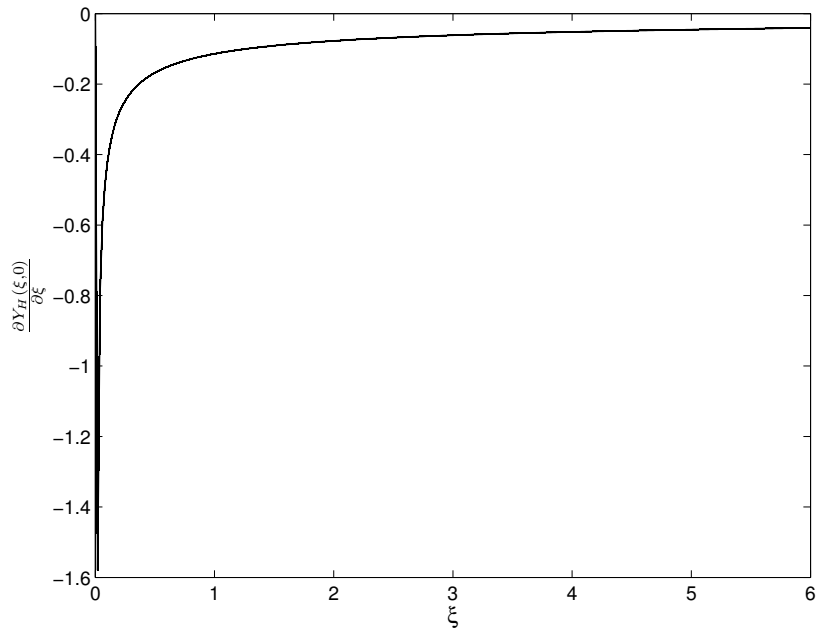


Figure 3.5: Numerical solution of  $\frac{\partial Y_H}{\partial \xi}$  along the surface of the plate for  $U_{cell} = 0.5$ . This demonstrates how the reaction rate of hydrogen along the surface of the plate varies.

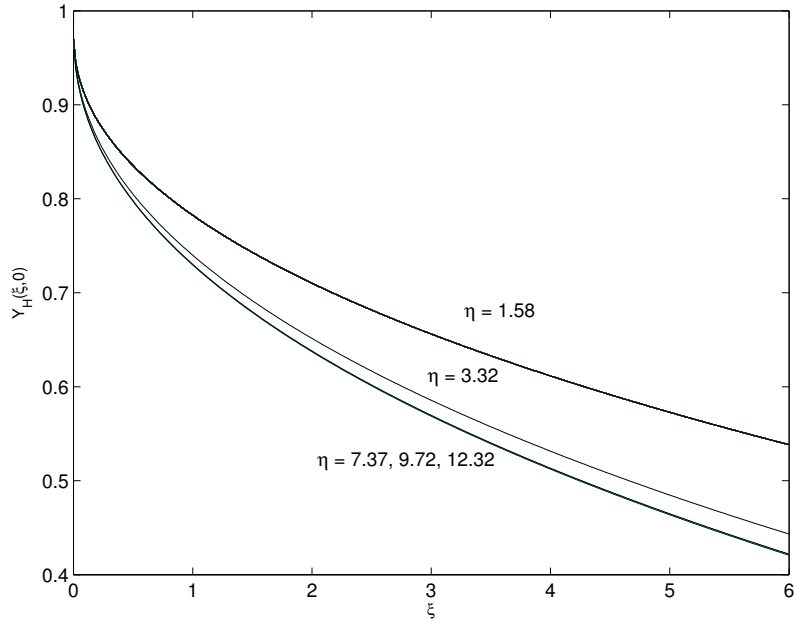


Figure 3.6:  $Y_H$  plotted along the surface of the plate for vary values of  $\eta$ . This plot demonstrates the reliance of convergence on the value of  $\eta$ .

now represent it in the entire domain of consideration. Here we have plotted the mass fraction of hydrogen for an overall cell potential of  $U_{cell}=0.5$ . This surface plot highlights how the surface reaction only has an effect on the flow within a small region close to the plate and that in the far field the flow is not altered. One point that is not entirely visible from this figure is that the reaction influences more into the free stream as we move along the plate. Alternatively, for larger values of  $\xi$  we see an influence from the reaction in larger values of  $\eta$ . Although the far field value of  $\eta_{max} \approx 12$  may seem excessive here, due to the reaction influence only being confined to a short distance close to the plate, it is necessary in order to obtain a convergent solution as mentioned earlier.

Fig. 3.6 demonstrates the reliance of convergence on the selected value of  $\eta$ . We can see that for  $\eta < 7.37$  the solution is not fully converge but for  $\eta > 7.37$  we can assume convergence for this particular model set-up. Therefore, to ensure convergence for any considered modelling conditions we set  $\eta_{max} \approx 12$ .

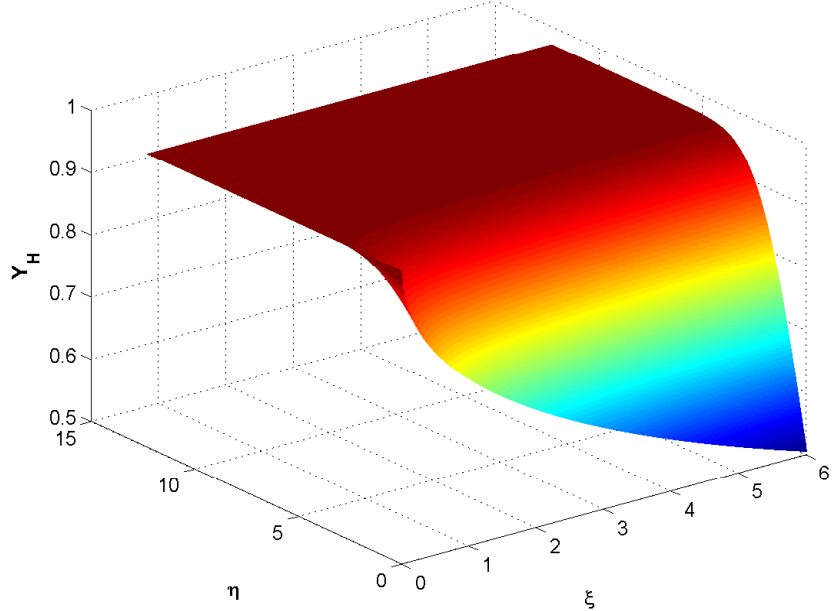


Figure 3.7:  $Y_H$  plotted against the coordinate system  $(\xi, \eta)$  for  $U_{cell} = 0.5$ . This demonstrates how the mass fraction of hydrogen varies throughout the flow domain.

For completeness we have plotted the mass fraction of water,  $Y_W$ , against the  $(\xi, \eta)$  coordinate system for  $U_{cell}=0.5$  in Fig. 3.8. Due to the condition given by (3.52) we know that the amount of water produced is exactly equal to that of hydrogen consumed.

Fig. 3.9 shows a plot of the surface mass fraction of hydrogen against the  $\xi$  coordinate for varying values of the potential  $U_{cell}$ . Here we have taken the values of  $U_{cell}$  to be  $U_{cell}=1, 0.8, 0.6, 0.4, 0.2, 0$ , where the top line corresponds to  $U_{cell} = 1$  and the subsequent lower lines correspond to decreasing values of  $U_{cell}$ . We can see here that for lower values of  $U_{cell}$  we have a greater reaction rate of hydrogen along the surface of the plate. The reason for this can be seen from the ion flux density equation (3.28) and (3.29) where decreases in  $U_{cell}$  promotes an increase in the ion flux density which explains the increase in the reaction rate.

A more detailed plot of the effects of varying values of  $U_{cell}$  against the surface mass fraction of hydrogen is given in Fig. 3.10. This plot highlights further the point that

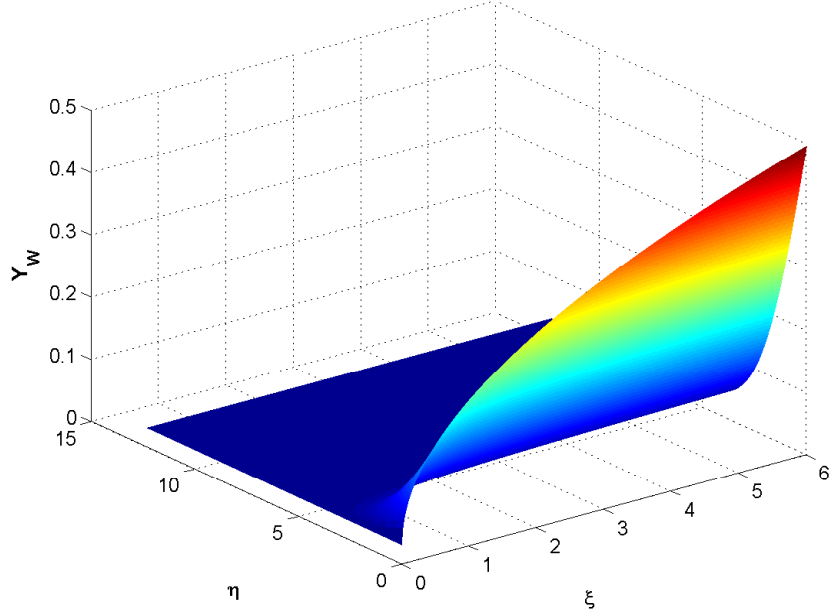


Figure 3.8:  $Y_W$  plotted against the coordinate system  $(\xi, \eta)$  for  $U_{cell} = 0.5$ . This demonstrates how the mass fraction of water varies throughout the flow domain (This is linked to the mass fraction of hydrogen since  $Y_H + Y_W = 1$ ).

decreasing the value of  $U_{cell}$  increases the reaction rate of hydrogen. Also for completeness we have plotted the surface mass fraction of water for varying values of  $U_{cell}$  in Fig. 3.11

During the establishment of this model we assumed that the oxygen concentration on the cathode side of the cell was constant and that it took the value of  $Y_O = 0.23$ , the mass fraction of concentration in air. In Fig 3.12 we investigated how the surface mass fraction of hydrogen varies for varying values of the mass fraction of oxygen on the cathode side for  $U_{cell} = 0.5$ . We examined values of  $Y_O$  in the range of 0.1 to 1 and discovered that the reaction rate of hydrogen increased with increasing values of  $Y_O$ . The reason for this comes from examination of the ion flux density (3.28) and (3.29) where it can be seen that increases in the value of  $Y_O$  from  $Y_O = a$  to  $Y_O = b$ , for  $b > a$ , gives an increase to  $q_e(\xi)$  of  $\frac{1}{2}\log(\frac{b}{a}) > 0$ . Any increase in the ion flux density will give an increase in the reaction rate of hydrogen and hence the production of water.

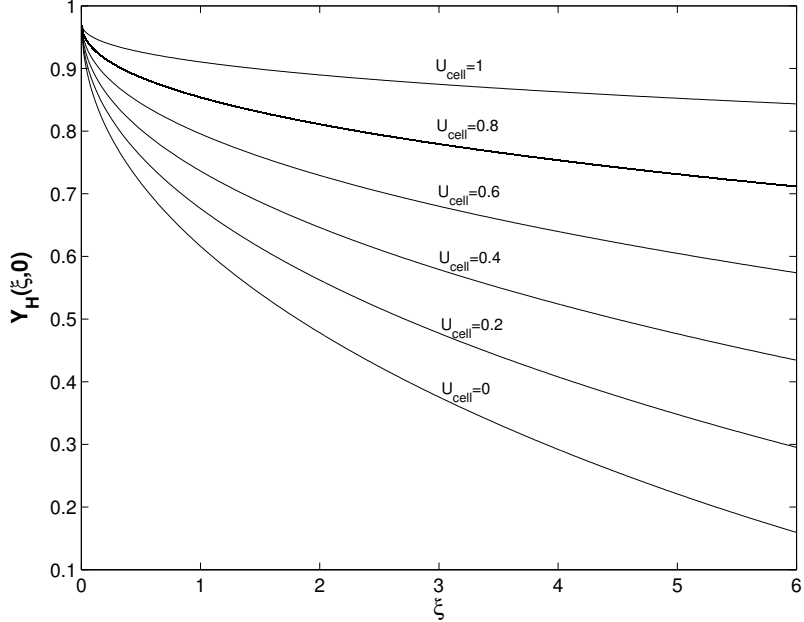


Figure 3.9: Plot of the surface mass fraction of hydrogen,  $Y_H(\xi, 0)$  for  $U_{cell}=1, 0.8, 0.6, 0.4, 0.2, 0$ . This demonstrates how the mass fraction of hydrogen along the surface of the plate varies when the cell potential is altered.

Further to assuming the mass fraction of oxygen remained constant at  $Y_O = 0.23$  we also assumed that the inlet mass fraction of hydrogen was set at  $\tilde{Y}_H = 0.97$ . Therefore, we examined the surface mass fraction of hydrogen when the inlet mass fraction of hydrogen was varied. We took values of  $\tilde{Y}_H$  between 0.03 to 0.97 since a full water inlet would provide no reaction and would give complications when calculating  $q_e(\xi)$ , this is due to the  $\log(Y_H)$  term becoming  $\log(0)$ . The results of this investigation are plotted in Fig. 3.13 for  $U_{cell} = 0.5$ . We can see that for very small amounts of hydrogen it is hard to distinguish whether there is a reaction occurring. From this, and from examination of  $q_e(\xi)$ , we would expect very low performance from an SOFC operated on with low input mass fractions of hydrogen. It should be noted here that this is only a theoretical representation which does not take into account flammability limits of a hydrogen inlet especially if oxygen has made it into the anode gas channel. For a large array of flammability limits see Coward

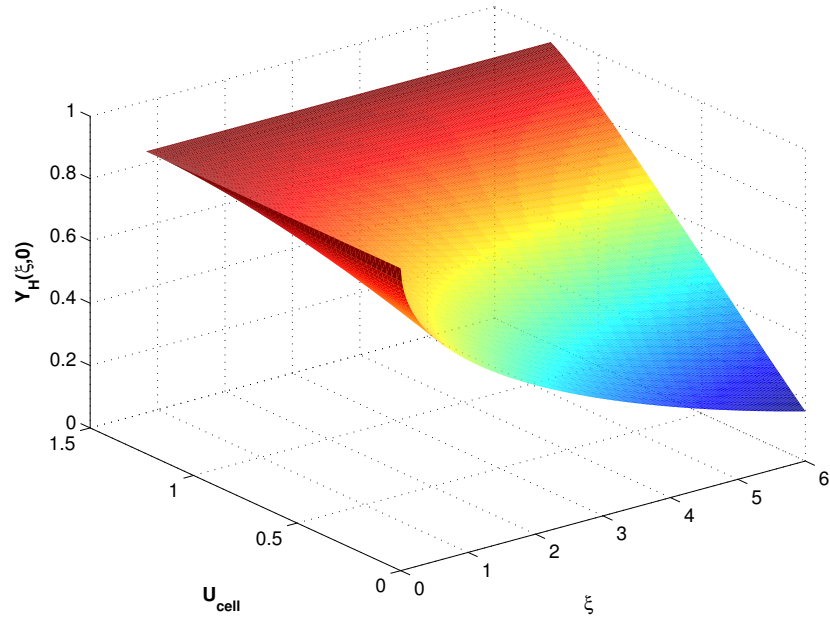


Figure 3.10: Plot of the surface mass fraction of hydrogen,  $Y_H(\xi, 0)$ , against  $\xi$  and varying values of  $U_{cell}$ . This demonstrates how the surface mass fraction of hydrogen varies for all considered cell potentials.

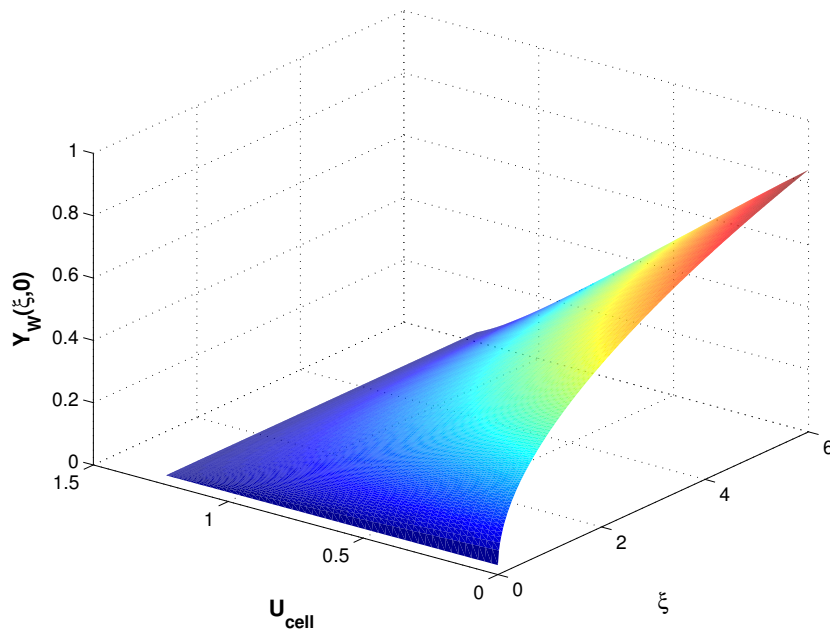


Figure 3.11: Plot of the surface mass fraction of water,  $Y_W(\xi, 0)$ , against  $\xi$  and varying values of  $U_{cell}$  (This follows from Fig 3.10 and from  $Y_H + Y_W = 1$ ).

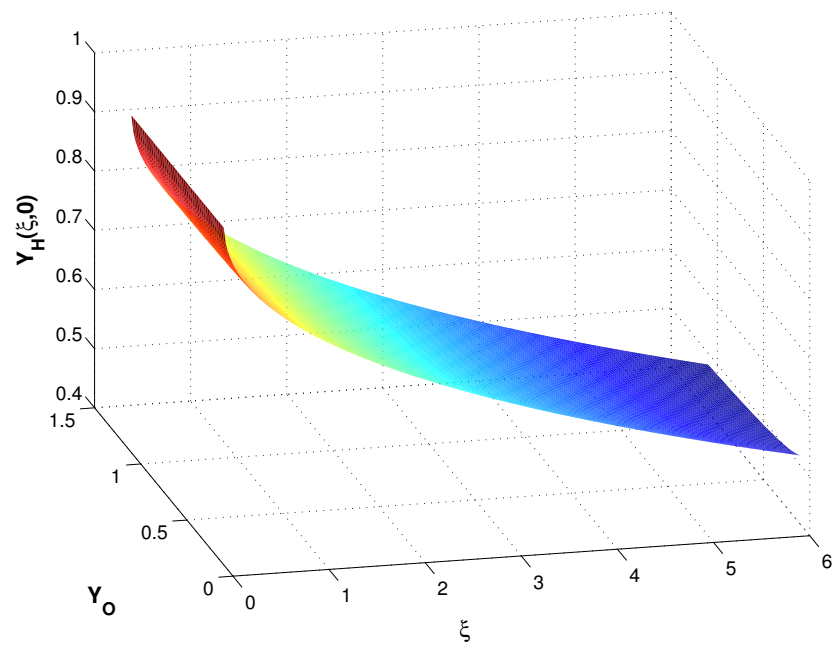


Figure 3.12: Plot of the surface mass fraction of hydrogen,  $Y_H(\xi, 0)$ , against  $\xi$  and varying values of the concentration of oxygen,  $Y_O$ , on the air side of the fuel cell. This demonstrates how the surface mass fraction of hydrogen varies when the concentration of oxygen present within the cathode is altered.

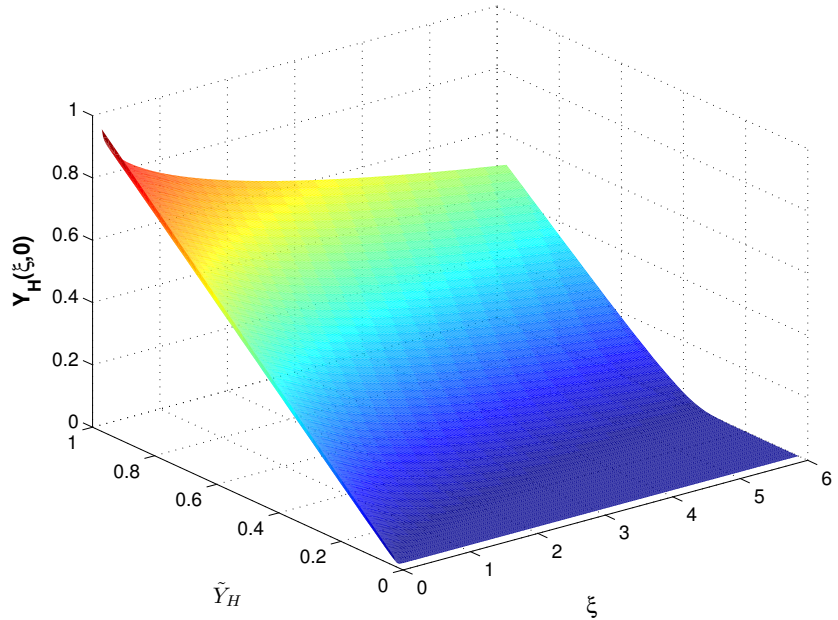


Figure 3.13: Plot of the surface mass fraction of hydrogen,  $Y_H(\xi, 0)$ , against  $\xi$  and varying values of the inlet mass fraction of hydrogen  $\tilde{Y}_H$ . This demonstrates how the surface mass fraction of hydrogen varies when the inlet composition of the anode is altered.

& Jones (1952).

In Fig. 3.14 we have plotted the surface mass fraction of hydrogen against the operating temperature along the plate. We have examined temperature variations between  $T = 1000\text{ }K$  and  $T = 1273\text{ }K$  which restricts our attention to high temperature fuel cells. From this plot we can see that the hydrogen surface mass fraction increases with increasing values of  $T$ , although the variation is small for  $\xi \leq 1$ .

All of the results demonstrated within this chapter are fundamental in identifying how certain operational conditions can affect the flow and reaction within a fuel cell. In the proceeding chapter we will also see how they are critical in determining and optimising the electrical performance of an SOFC.

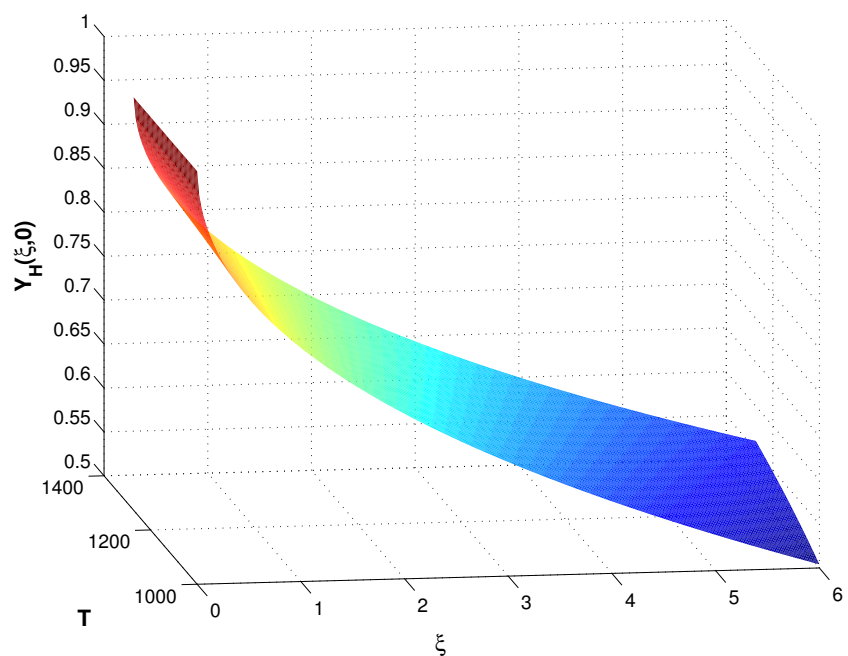


Figure 3.14: Plot of the surface mass fraction of hydrogen,  $Y_H(\xi, 0)$ , against  $\xi$  and varying values of Temperature  $T$ . This demonstrates how the surface mass fraction of hydrogen varies when the operating temperature of the cell is altered

## 3.10 Validation

In order to assess the validity of the model results we need to ensure that the analytical and numerical methods are sound. In order to do this we require an existing model which we can use to draw comparisons with our own. The difficulty in doing this is that rigorous mathematical models for fuel cells are limited and do not adopt this novel modelling technique. Therefore, we seek a more theoretical model that aligns closely to one set out within this chapter.

(Merkin, 1996) developed an analytical and numerical model for the homogeneous and heterogeneous reactions of two generic species over a flat, semi infinite, impermeable plate. This model is comparable to the one laid out in this chapter, differing on its applicability towards fuel cells. Therefore, in order to assess the validity of our analytical and numerical framework the model was adjusted to align with that presented by (Merkin, 1996) and the results plotted within Fig. 3.15

The validation results plotted in Fig. 3.15 exactly match those published within (Merkin, 1996) . This therefore validates our analytical and numerical framework as fit for purpose for the model within this chapters and subsequent similar model.

## 3.11 Chapter Summary

Within this chapter we have constructed a model for the incompressible flow and heterogeneous reaction of humidified hydrogen across a flat semi-infinite impermeable plate. The purpose of this is to reduce the model for a planar SOFC to a first principles model in order to increase rigorous analytical techniques and numerical efficiency.

We have demonstrated the construction of a framework of governing equations and boundary conditions to model the flow and surface reaction. Moreover, we have shown how boundary-layer theory and self-similarity can be utilised to reduce the complexities

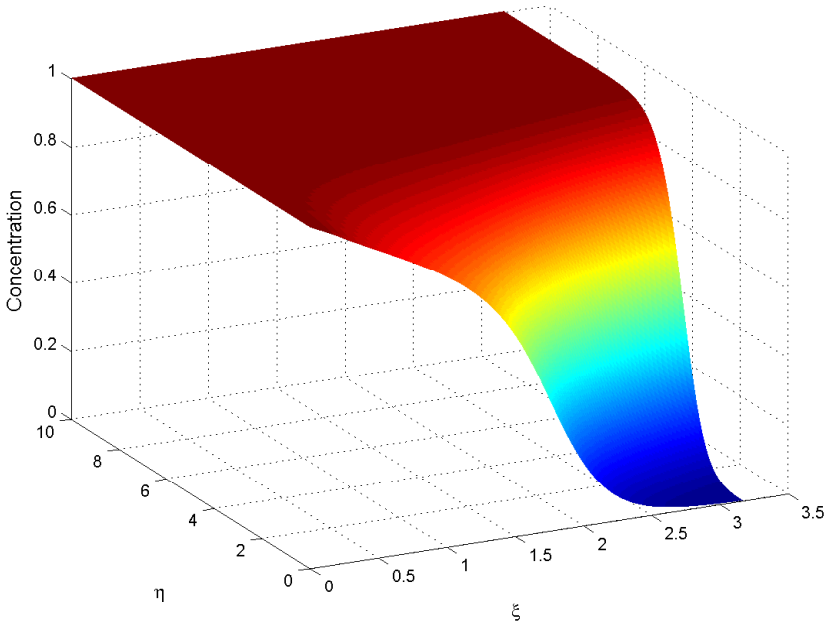


Figure 3.15: Analytical and numerical model methodology applied to the model developed by Merkin (1996)

involved in a numerical solution. A rigorous asymptotic analysis approach has been undertaken to understand the flow and reaction close to a naturally occurring singularity within the flow. Matching this analysis with a highly efficient numerical solution (to the order of seconds) means that we have generated a model which produces fast solutions that we can have confidence in.

It should be noted here that this model is a simplified first principles view of an operating SOFC. Due to these simplifications the results may not be indicative of what one would expect to see in experimental outputs. However, the benefits and value of this model are in the construction of a rigorous analytical and efficient numerical framework which will be applied to all the models throughout this work. Therefore, even though the results within this chapter may not have same level of accuracy compared to empirical data, they are fundamental in the construction and solutions of the proceeding models.

# CHAPTER 4

## ELECTRICAL MODEL

In chapter 3 we constructed a simplified model for the reactions within a planar SOFC operating on humidified hydrogen. We also demonstrated how the mass fractions of species vary along the surface of the plate and with varying cell potential. However, the most useful outputs from fuel cell analysis is a current-voltage plot, or I-V curve as it is more commonly known, as well as current-power plots. The main concept of the I-V curve is to demonstrate the electrical performance of the cell when it is operated at varying voltages and currents. The current-power plots identify the maximum operating power output and the values of cell current which achieve this. From these one is able to find the optimal electrical performance attainable from the cell, or cell stack, which gives optimal operating conditions for that cell, or cell stack.

### 4.1 Current-voltage plot

To produce the current-voltage plot for our model represented in chapter 3 we need to have an expression that couples the current and voltage. In the previous chapter we gave an equation which demonstrates this

$$i(x) = 2Fq_e(x), \quad (4.1)$$

where  $i(x)$  is the local current density,  $F$  is Faraday's constant and  $q_e(x)$  is the local ion flux density. We have seen that the ion flux density can be expressed as

$$q_e(x) = \frac{RT}{4F^2R_s} \left[ \ln \left( \frac{Y_H Y_O^{\frac{1}{2}}}{Y_W} \right) + \ln \left( \frac{m_W(\rho RT)^{\frac{1}{2}}}{m_H m_O^{\frac{1}{2}}} \right) + \frac{2F}{RT}(U^r - U_{cell}) \right] \quad (4.2)$$

and we showed that after non-dimensionalisation we obtain

$$q_e(x) = \ln \left( \frac{Y_H Y_O^{\frac{1}{2}}}{Y_W} \right) + \sigma \quad (4.3)$$

where the dimensionless parameter  $\sigma$  is given by

$$\sigma = \ln \left( \frac{m_W(\rho_{in} RT)^{\frac{1}{2}}}{m_H^{\frac{1}{2}} m_O^{\frac{1}{2}}} \right) + \frac{2F}{RT}(U^r - U_{cell}) \quad (4.4)$$

Therefore, (4.1), (4.3) and (4.4) represent a coupled system that we can use to produce a current-voltage plot from our model. Before we proceed in producing a plot to represent the electrical performance we are required to give a couple of details regarding the coupled system.

As we stated in chapter 3, section 3.3, we take the voltage, or cell potential, as a variable. This results in  $\sigma$  varying, as was shown in Table 3.2 and since we know all the other parameter values within  $\sigma$  we can say that  $\sigma$  is a known variable. Furthermore, we know the values of  $Y_H$  and  $Y_W$  for varying values of the voltage from chapter 3 and we have made the assumption that  $Y_O$  is constant and takes the value  $Y_0 = 0.23$ . Thus from our model result we can calculate the value of the ion flux density  $q_e(x)$  for varying values of the cell voltage and hence we can calculate the current density for varying values of the cell voltage.

In Fig. 4.1 we have plotted the cell voltage  $U_{cell}$  against the current density  $i$ , for

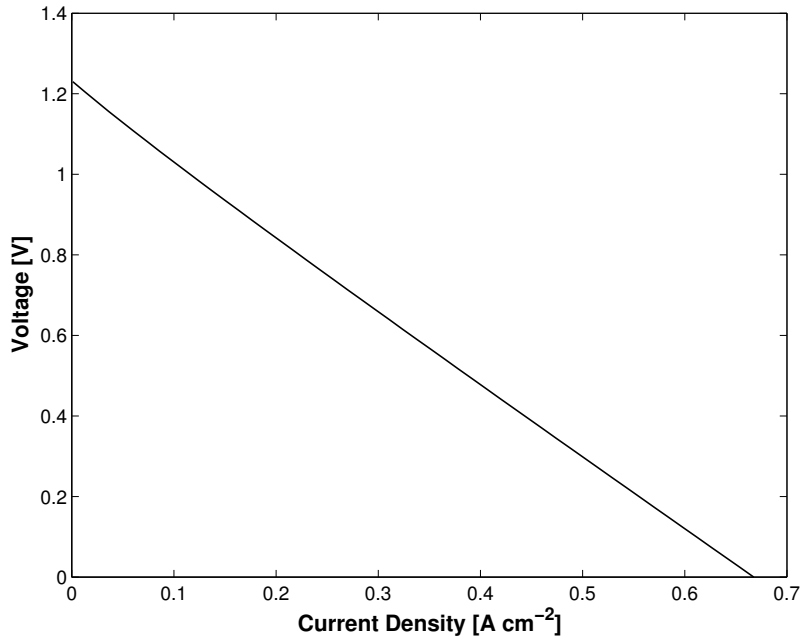


Figure 4.1: Average current-voltage plot across the length  $0 \leq \xi \leq 1$ . This demonstrates the relationship between the cell voltage and current density for this model.

the range  $0 \leq \xi \leq 1$ , which is known as an I-V or current-voltage curve. These curves represent the changes in the cell potential when there is a change in current drawn from the cell. The I-V curve is a fundamental aspect of fuel cell research as it gives details on the operating characteristics of a particular cell. We can see from our plot that we have a linear relationship between the cell voltage and the current density. The reason for this is that when we establish the electrochemistry for our model, in section 3.3, we assume that the only overpotential was that of the ohmic overpotential (3.18). Hence we would expect to see a linear relationship between these two variables. In establishing this plot we utilise the information generated by Figs. 3.10 and 3.11 to calculate  $q_e(\xi)$  for varying values of  $U_{cell}$ . Once we calculated  $q_e(\xi)$  we were required to find its average value in the range  $0 \leq \xi \leq 1$  and then use the relationship (4.1) to obtain the current density for varying  $U_{cell}$ .

In Fig. 4.1 we plotted the average current-voltage curve in the region  $0 \leq \xi \leq 1$  but

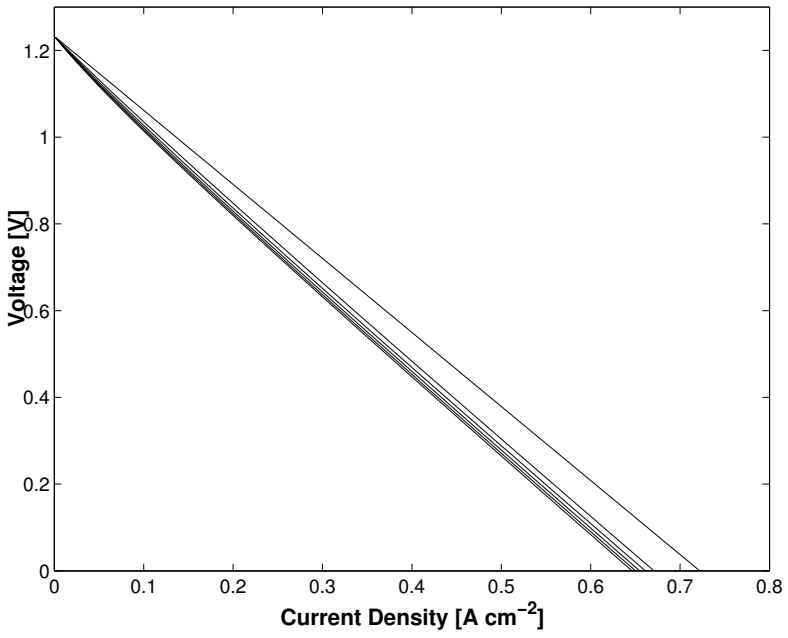


Figure 4.2: Current-voltage plot for varying values of  $\xi$ ,  $\xi=0, 0.2, 0.4, 0.6, 0.8, 1$ , where increasing  $\xi$  corresponds to a right to left shift in curves. This demonstrates how the relationship between cell potential and current density varies at different positions along the plate.

this does not describe how the cell performance varies positionally. Fig. 4.2 represents varying current-voltage curves for various positions along the plate, for  $\xi=0, 0.2, 0.4, 0.6, 0.8, 1$ . The curve on the far right corresponds to that of  $\xi = 0$  and the shift left in curves corresponds to increasing values of  $\xi$ . We had shown previously in Fig. 3.5 that the reaction rate of hydrogen is at its highest close to the leading edge. Therefore, it is expected that the highest current density values are achieved within this region. We can also see that as we move along the plate these curves seem to be converging which is a sign that the reaction rate of hydrogen is slowing down. This slowing down of the reaction rate is also represented in Fig. 3.5 since over short distances away from the leading edge, say  $\xi = 0.2$ , we can see that the variation in  $Y_H$  is much less than that of the variation around  $\xi = 0$ .

## 4.2 Current-power plot

In the previous section we demonstrated how we produce current-voltage plots from our model in chapter 3. However, current-voltage plots do not give any details about how much power is outputted from our cell model. Power production is a key factor in fuel cell manufacturing and implementation since you want to produce the maximum amount of power you can from a single cell. Furthermore, for operational reasons we would like to know what voltage the cell should be run at in order to produce the maximum power. Therefore, we require an equation which relates the power output of the cell to the cell voltage. Such an equation is given by

$$P(x) = i(x)U_{cell}, \quad (4.5)$$

where  $P(x)$  represents the local power density of the cell. We can see that due to the linear relationship between the current density and the voltage we would expect a quadratic relationship between the current density and the power density.

Fig. 4.3 shows the cell power output within the range  $0 \leq \xi \leq 1$ , where we have used the results in Fig. 4.1 to find the relationship between potential and current density and then used (4.5) to calculate the power density. From this plot we can deduce that the highest power density achievable is  $0.1994 \text{ W cm}^{-2}$  which occurs at a current density of  $0.3377 \text{ A cm}^{-2}$ . If we examine Fig. 4.1 we can see that this current density is equivalent to a cell voltage of  $0.6 \text{ V}$ . Hence, from our model we can deduce that in order to produce the maximum amount of power from the cell it should be operated at  $0.6 \text{ V}$ .

As with the current-voltage plots, Fig. 4.3 does not give details about how the cell is performing spatially, only details regarding the average cell performance. In Fig. 4.4 we have plotted power density against current for varying cell positions along the plate, for  $\xi=0, 0.2, 0.4, 0.6, 0.8, 1$ . The curve on the far right corresponds to that of  $\xi = 0$  with

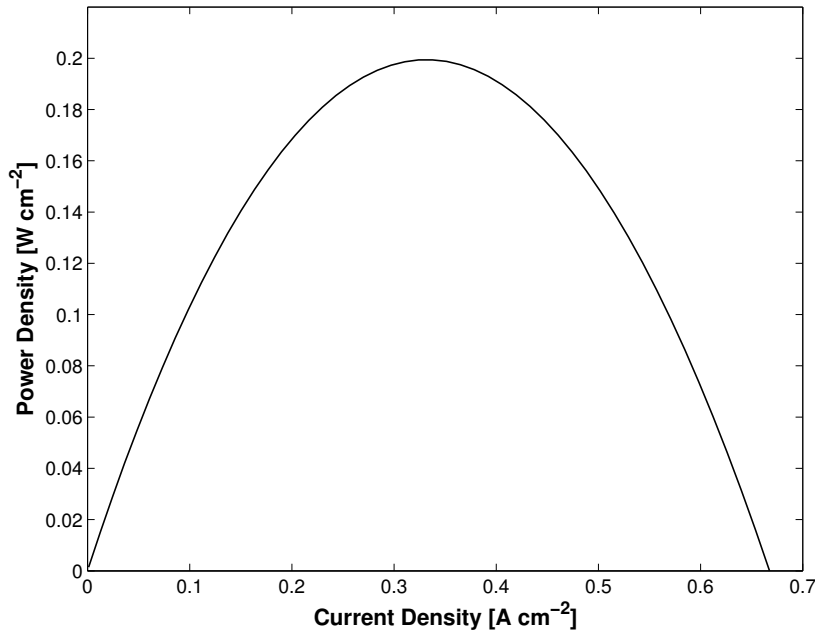


Figure 4.3: Average current-power plot across the length  $0 \leq \xi \leq 1$ . This demonstrates the relationship between the cell power density and current density for this model.

decreasing curves corresponding to increasing  $\xi$ . Since the point  $\xi = 0$  is the position where the highest reaction rate of hydrogen is achieved and hence the largest ion flux density, we should expect to see this region giving the largest value of the cells power density.

We have seen from Figs. 4.1-4.4 how varying the electrochemical parameters can have an effect on the overall performance of the cell. We now wish to focus our concentration on how varying the inlet parameters can affect the cell performance. In Fig. 4.5 we have plotted the power density of the cell against the mass fraction of oxygen on the air side of the cell. We can see from this plot that increasing the level of oxygen within the air side of the cell increases the power density of the cell. More specifically, increasing the mass fraction of oxygen from  $Y_O = 0.1$  to  $Y_O = 1$  gives an increase in the power density of  $0.0136 \text{ W cm}^{-2}$ . This is to be expected as increasing  $Y_O$  increases the ion flux density through equation (4.2) which inherently increases the power density through the relationship between the ion flux density and the current density of the cell.

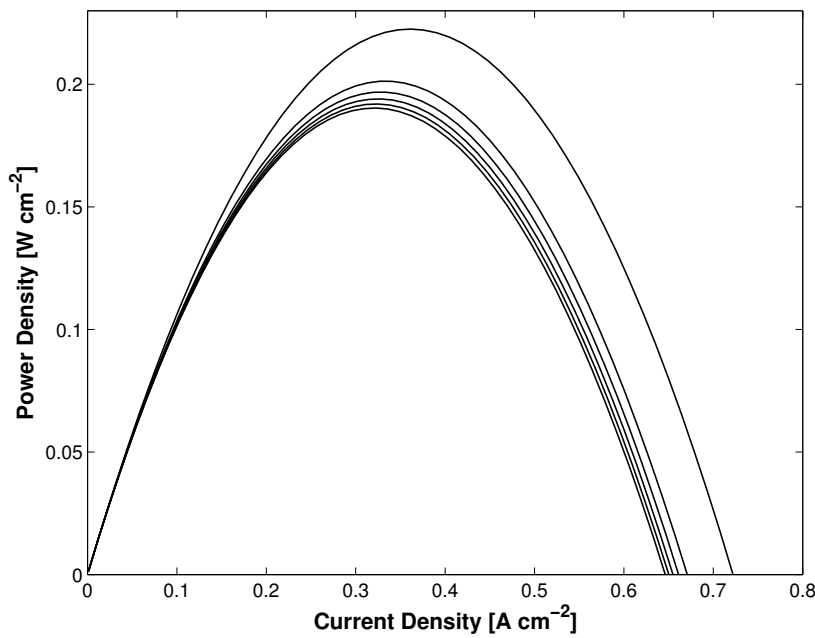


Figure 4.4: Current-power plot for varying values of  $\xi$ ,  $\xi=0, 0.2, 0.4, 0.6, 0.8, 1$ , where increasing  $\xi$  corresponds to a right to left shift in curves. This demonstrates how the relationship between the cell power density and current density varies at different positions along the plate.

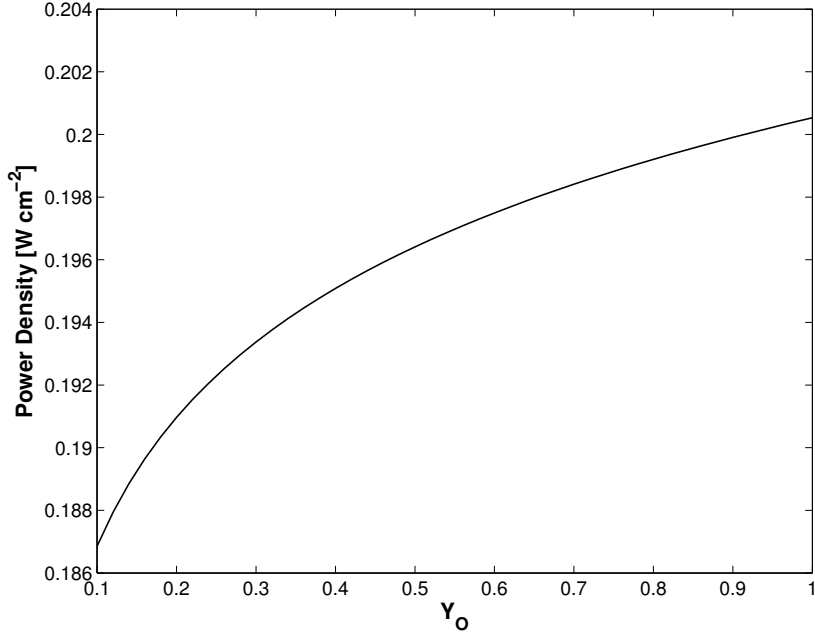


Figure 4.5: Power density plotted against varying values of the concentration of oxygen on the air side,  $Y_O$ , for  $U_{cell}=0.5$ . This demonstrates how the achievable cell power density varies when the oxygen mass fraction within the cathode side of the cell is altered.

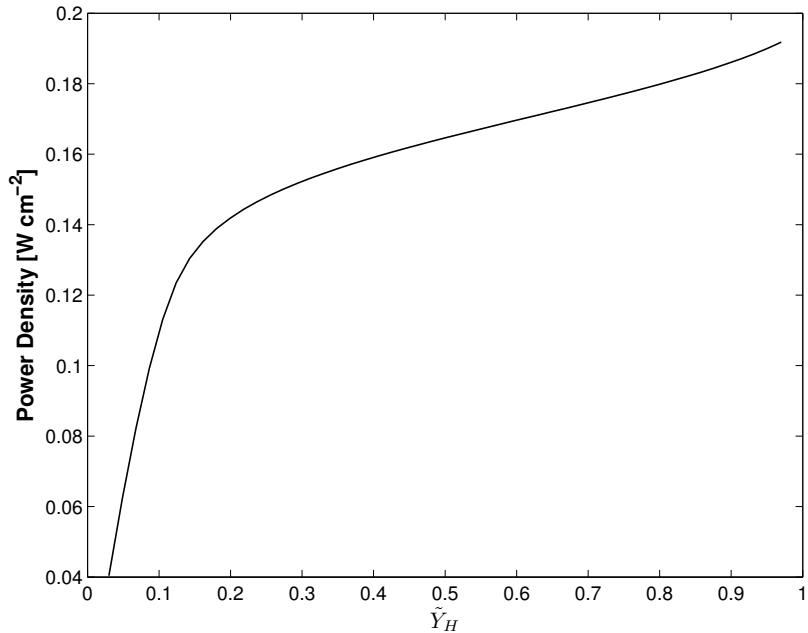


Figure 4.6: Power density plotted against varying values of the inlet mass fraction of hydrogen,  $\tilde{Y}_H$ , for  $U_{cell}=0.5$ . This demonstrates how the achievable cell power density varies when the anode inlet composition is altered.

In Fig. 4.6 we have plotted the power density of the cell against the inlet mass fraction of hydrogen  $\tilde{Y}_H$ . We can see that the power density increases with increasing values of the inlet mass fraction with an increase of  $0.1514 \text{ W cm}^{-2}$  when  $\tilde{Y}_H$  is increased from  $\tilde{Y}_H = 0.03$  to  $\tilde{Y}_H = 0.97$ . Moreover, we can see the drastic increase in power density from  $\tilde{Y}_H=0.03$  to  $\tilde{Y}_H \approx 0.2$ , where the increase after this point has a more linear behaviour. This increase is due to the  $\log(Y_H)$  term which is present in the ion flux density equation (4.2). On examination of the  $\log$  function we can see that the largest increases in its value occur when the number you are taking the logarithm of is small. However, one must note that not all of the values of  $\tilde{Y}_H$  given within this plot are valid. In operational fuel cells oxygen leakages can occur within the anode side of the cell which can combust with hydrogen if fuel inlet is not hydrogen rich or sparse. Therefore, some consideration will need to be given regarding these combustion limits before establishing the inlet mass fractions (Coward & Jones, 1952).

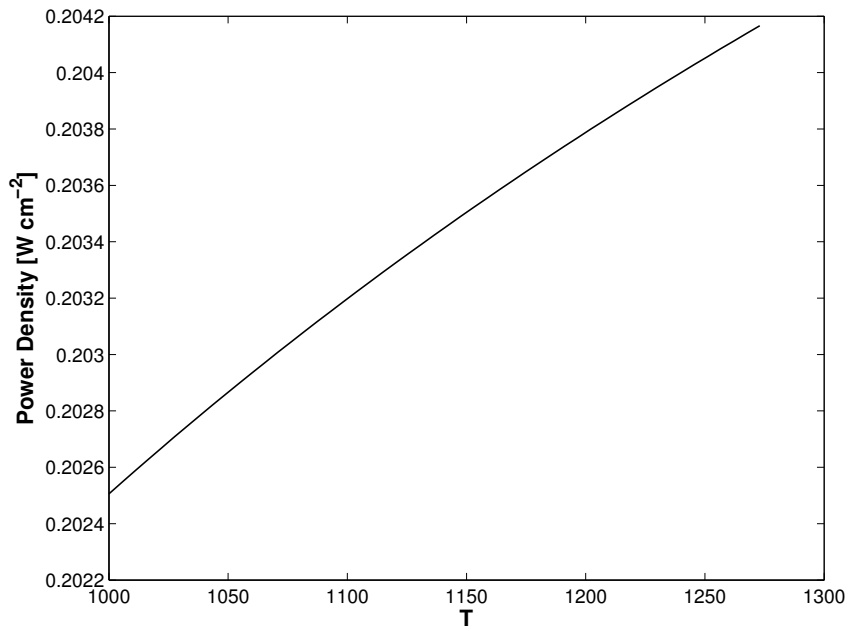


Figure 4.7: Power density plotted against varying values of the cell temperature,  $T$ , for  $U_{cell}=0.5$ . This demonstrates how the achievable cell power density varies well the operating temperature of the cell is altered.

Although the model in chapter 3 is considered to be isothermal we still have to set the inlet and cell operating temperature. In Fig. 4.7 we investigated how the power density of the cell varies when we alter the operating temperature of the cell. We have concentrated mainly on the high temperature region and as such have examined temperatures between  $T = 1000\text{ }K$  and  $T = 1273\text{ }K$  to see what effects vary this temperature has. We can see from this plot that power density and temperature have an almost linear relationship and so increasing the temperature increases the power density of the cell. More specifically, the power density increases by  $0.0017\text{ }W\text{ }cm^{-2}$  when we increase the temperature from  $T = 1000$  to  $T = 1273$ .

# CHAPTER 5

## HETEROGENEOUS REACTION IN BOUNDARY-LAYER FLOW WITH ELECTROCHEMISTRY WITH METHANE INLET

In chapter 3 we considered the heterogeneous reaction of humidified hydrogen across a flat semi-infinite plate and examined a model for this to depict an operational planar SOFC. We now wish to adapt this model to consider an inlet mixture involving methane rather than hydrogen as the fuel. One of the main reasons for considering methane as a fuel is that 96% of hydrogen is currently produced from reforming hydrocarbons (Armor, 1999) which makes it not only expensive and difficult to store but also means that it is prone to explosions (Kendall, 2000). Therefore, more work has been conducted to examine direct reforming of methane within an SOFC, with steam reforming being the most economical way of producing hydrogen (Armor, 1999). Methane is a fuel that is readily available and is already used in many domestic applications such as gas cookers and boiler systems. Therefore, this makes methane a safer, cheaper and more economically viable fuel on

which an SOFC can be operated on.

The use of methane as a fuel to operate SOFCs on is commonly used by experimentalists since direct reforming of methane to hydrogen can occur within the cell. This is due to the high operating temperatures of SOFCs which results in these cells being able to deal with impurities that would destroy other cells, as shown in Table 2.2.

## 5.1 Model description

The model we now present is identical to that depicted in Fig. 3.2 apart from the fact we are no longer using humidified hydrogen as our inlet mixture. The inlet mixture in this model will consist mainly of helium and methane with a small amount of water. We will consider the same mole fractions as Cooper *et al.* (2000) which is taken to be 90% helium and 10% methane and water. This gives us the mole fractions 54/60 for helium, 5/60 for methane and 1/60 for water. The inlet composition will once again be pre-heated to 1000K as it approaches the anode of the cell. The reaction scheme within this model is a lot more complex than that shown in chapter 3. The consideration of all possible reactions that could be present within an SOFC operating on this inlet is not viable or practical from an efficiency point of view. Therefore, we will only consider the reactions given below



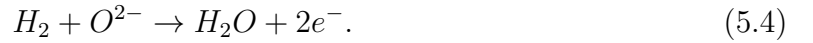
where  $k_i$  are the reaction rate coefficients and  $C_i$  are the concentrations of species  $i$ . The above system of reactions are considered irreversible for the purpose of this model

for simplification. Physically these reactions are reversible for temperatures of 1000K. We denote the subscripts  $i$  by the following: f(Methane), W(Water), D(Carbon dioxide), M(Carbon monoxide), H(Hydrogen) and h(Helium). Since Helium is inert we do not need to consider the species within this model, just to note that it remains at a constant level and that it will appear in experimental work.

Reaction (5.1) is known as the steam reforming reaction which produces hydrogen from the initial inlet mixture. The steam reforming reaction is highly endothermic ( $\Delta H = 206.2 \text{ kJ/mol}$ ) and is considered to need a large amount of energy to implement as well as a nickel or supported nickel catalyst for a rapid reaction. Therefore, we will consider the steam reforming reaction to be a heterogeneous reaction due to the need of a catalyst. Reaction (5.2) is known as methane dry reforming which utilises the carbon dioxide which is produced during operation and converts it into useful hydrogen. Once again the dry reforming reaction is highly endothermic ( $\Delta H = 247 \text{ kJ/mol}$ ) and requires high energy levels in order to take place. A normal negative with this reaction is that it requires operating temperatures of  $> 700^\circ\text{C}$  which will occur in most SOFCs (Tu *et al.*, 2011). Furthermore, the dry reforming reaction also requires the presence of a catalyst, generally nickel based, in order to operate. Therefore, we will once again consider this reaction to also be heterogeneous. Finally, reaction (5.3) is known as the water gas shift reaction which converts carbon monoxide and water into hydrogen and carbon dioxide (the carbon dioxide is subsequently used in (5.2)). The water gas shift reaction is slightly exothermic ( $\Delta H = -41.2 \text{ kJ/mol}$ ) and therefore releases energy back into the system rather than consuming it as in (5.1) and (5.2). As is common with the other two reactions a catalyst is required in order for the reaction to form. One difference with the water gas shift reaction is that it can operate at low and high temperatures but the similarity is that a nickel based or nickel-loaded catalyst is required (Li *et al.*, 2000).

The reactions above, (5.1)-(5.3), generate hydrogen from the initial inlet of methane,

water and helium. Once hydrogen has been generated within the cell it can be utilised by the hydrogen oxidation reaction, given by



with the details of this reaction given in section 3.1.

In the construction of this model we will make the following assumptions:

- The reactions will be assumed to be isothermal;
- The substrate will be assumed to be flat, semi-infinite and impermeable;
- The initial velocity is uniform as it approaches the plate with velocity  $u = U_0$ , where  $u$  is the streamwise velocity component;
- The length of the plate will be assumed to be  $L$ ;
- The flow is incompressible;
- Constant pressure;
- Non-zero viscosity resulting in a boundary-layer forming across the plate, proceeding from the leading edge;
- The flow is operating under steady state conditions and is therefore well mixed in the uniform stream before it reaches the plate.

## 5.2 Mathematical model

Many of the details of the mathematics and electrochemistry involved within this model have been explained and presented within sections 3.2 and 3.3. Therefore, we will not go into details about the equations which will be used but just state them for the readers convenience.

The conservation of momentum within the model is governed by the boundary layer equation

$$u \frac{\partial u}{\partial x} + v \frac{\partial u}{\partial y} = \nu \frac{\partial^2 u}{\partial y^2}, \quad (5.5)$$

where  $u$  and  $v$  are again the streamwise and transverse velocity components,  $x$  and  $y$  are the streamwise and transverse coordinates and  $\nu$  is the kinematic viscosity of the mixture. Taking into account the incompressibility assumption yields the following

$$\frac{\partial u}{\partial x} + \frac{\partial v}{\partial y} = 0 \quad (5.6)$$

In this model equations (5.5) and (5.6) control the momentum of the fluid mixture. We now define the equation for the conservation of mass of each of the species involved, which is given by

$$u \frac{\partial Y_i}{\partial x} + v \frac{\partial Y_i}{\partial y} = D_i \frac{\partial^2 Y_i}{\partial y^2} \quad (5.7)$$

where the term  $Y_i$  is the mass fraction of species  $i$  and is calculated by

$$Y_i = \frac{m_i C_i}{\rho} \quad (5.8)$$

It should be noted that the amount of each of the species given in section 5.1 is given in mole fractions rather than mass fractions. Hence, we require an equation to convert these mole fraction values into mass fractions so we can utilise them in our model. Such an equation is given by

$$Y_i = \frac{X_i m_i}{\sum_i X_i m_i} \quad (5.9)$$

where  $X_i$  is the mole fraction of species  $i$ .

The model electrochemistry that we are going to incorporate into this model is identical to that developed in section 3.3. Therefore, we will not go into great detail regarding the equations but simply state them for completeness. The current density of the cell is related to the ion flux density via

$$i(x) = 2Fq_e(x), \quad (5.10)$$

where  $F$  is the Faraday constant,  $i(x)$  is the local current density and  $q_e(x)$  is the local ion flux rate. The Nernst equation, written in terms of the mass fractions of species is given by

$$U^N = U^r + \frac{RT}{2F} \ln \left( \frac{Y_H Y_O^{\frac{1}{2}} m_W (\rho RT)^{\frac{1}{2}}}{Y_W m_H m_O^{\frac{1}{2}}} \right) \quad (5.11)$$

where  $U^r$  is the ideal potential,  $R$  is the gas constant,  $T$  is the absolute temperature and  $\rho$  is the mixture density. Moreover, in this model we again assume that  $Y_O$  is constant and takes the value  $Y_O = 0.23$ . We can relate the Nernst potential to the overall cell potential due to the relationship

$$U_{cell} = U^N - i(x)R_s, \quad (5.12)$$

where the term  $i(x)R_s$  corresponds to an ohmic overpotential and  $R_s$  is the specific resistance of the substrate to the ion conduction. Combining (5.10),(5.11) and (5.12) yields the following equation for the ion flux density

$$q_e(x) = \frac{RT}{4F^2 R_s} \left[ \ln \left( \frac{Y_H Y_O^{\frac{1}{2}}}{Y_W} \right) + \ln \left( \frac{m_W (\rho RT)^{\frac{1}{2}}}{m_H m_O^{\frac{1}{2}}} \right) + \frac{2F}{RT} (U^r - U_{cell}) \right] \quad (5.13)$$

### 5.3 Boundary conditions

Now we have established the mathematical and electrochemical equations that govern our model. We are required to give an accurate set of boundary conditions that depict the flow and reaction within the domain. The input gas consists of very slightly humidified methane and the flow is assumed to be uniform, with respect to the streamwise coordinate. We can calculate the mass fractions of the inlet species using (5.9) and the mole fractions given in section 5.1. Hence, the inlet boundary conditions are (for  $y > 0$ )

$$Y_f = \tilde{Y}_f, Y_h = \tilde{Y}_h, Y_W = \tilde{Y}_W, Y_D = 0, Y_M = 0, Y_H = 0, u = U_0, v = 0 \text{ on } x = 0 \quad (5.14)$$

where the values of  $\tilde{Y}_f$ ,  $\tilde{Y}_h$  and  $\tilde{Y}_W$  are given by

$$\tilde{Y}_f = 0.2548, \quad \tilde{Y}_h = 0.6879, \quad \tilde{Y}_W = 0.0573 \quad (5.15)$$

The boundary conditions far from the plate are given by (for  $x > 0$ )

$$Y_f \rightarrow \tilde{Y}_f, Y_h \rightarrow \tilde{Y}_h, Y_W \rightarrow \tilde{Y}_W, Y_D \rightarrow 0, Y_M \rightarrow 0, Y_H \rightarrow 0, u \rightarrow U_0, v \rightarrow 0 \text{ as } y \rightarrow \infty \quad (5.16)$$

On the surface of the plate we have the no-slip condition for the velocity components

$$u = 0, \quad v = 0 \quad \text{on} \quad y = 0, \quad x > 0 \quad (5.17)$$

Since all of the reactions (5.1)-(5.4) occur on the surface of the plate it is necessary to balance the amount of each of the species transported through normal diffusion with the amount that is produced or consumed within the reactions. Therefore, we introduce the

mass-flux boundary conditions on the plate

$$D_f \frac{\partial Y_f}{\partial y} = \frac{k_1 Y_f Y_W \rho}{m_W} + \frac{k_2 Y_f Y_D \rho}{m_D}, \quad (5.18)$$

$$D_h \frac{\partial Y_h}{\partial y} = 0, \quad (5.19)$$

$$D_D \frac{\partial Y_D}{\partial y} = \frac{k_2 Y_f Y_D \rho}{m_f} - \frac{k_3 Y_M Y_W \rho m_D}{m_M m_W}, \quad (5.20)$$

$$D_W \frac{\partial Y_W}{\partial y} = \frac{k_1 Y_f Y_W \rho}{m_f} + \frac{k_3 Y_M Y_W \rho}{m_M} - \frac{q_e(x) m_W}{\rho}, \quad (5.21)$$

$$D_M \frac{\partial Y_M}{\partial y} = \frac{k_3 Y_M Y_W \rho}{m_W} - \frac{k_1 Y_f Y_W \rho m_M}{m_f m_W} - \frac{2k_2 Y_f Y_D \rho m_M}{m_f m_D}, \quad (5.22)$$

$$D_H \frac{\partial Y_H}{\partial y} = \frac{q_e(x) m_H}{\rho} - \frac{3k_1 Y_f Y_W \rho m_H}{m_f m_W} - \frac{2k_2 Y_f Y_D \rho m_H}{m_f m_D} - \frac{k_3 Y_M Y_W \rho m_H}{m_M m_W}, \quad (5.23)$$

## 5.4 Non-dimensionalisation

We have established a model for the governing equations (5.5),(5.6) and (5.7) with the corresponding boundary conditions (5.14)-(5.23) in dimensional form. We now introduce the following non-dimensional variables

$$\begin{aligned} \bar{m}_i &= \frac{m_i}{m_H}, & \bar{\rho} &= \frac{\rho}{\rho_{in}}, & u &= U_0 \bar{u}, & v &= U_0 Re^{-\frac{1}{2}} \bar{v}, & \bar{x} &= \frac{x}{L}, & \bar{y} &= \frac{y Re^{\frac{1}{2}}}{L}, \\ \bar{k}_i &= \frac{k_i}{k_1}, & \bar{q}_e(x) &= \frac{4F^2 R_s}{RT} q_e(x), & Re &= \frac{U_0 L}{\nu} \end{aligned} \quad (5.24)$$

Applying these new variables to the ion flux density gives (on dropping the bars for convenience)

$$q_e(x) = \ln \left( \frac{Y_H Y_O^{\frac{1}{2}}}{Y_W} \right) + \sigma \quad (5.25)$$

where  $\sigma$  is a non-dimensional parameter defined to be

$$\sigma = \ln \left( \frac{m_W(\rho_{in}RT)^{\frac{1}{2}}}{m_H^{\frac{1}{2}} m_O^{\frac{1}{2}}} \right) + \frac{2F}{RT}(U^r - U_{cell}) \quad (5.26)$$

Under the assumption that the flow is incompressible we have that  $\bar{\rho} = 1$ . Now applying these variables to the momentum and mass conservation equations yields

$$\frac{\partial u}{\partial x} + \frac{\partial v}{\partial y} = 0, \quad (5.27)$$

$$u \frac{\partial u}{\partial x} + v \frac{\partial u}{\partial y} = \frac{\partial^2 u}{\partial y^2}, \quad (5.28)$$

$$u \frac{\partial Y_i}{\partial x} + v \frac{\partial Y_i}{\partial y} = \frac{1}{S_{ci}} \frac{\partial^2 Y_i}{\partial y^2}, \quad (5.29)$$

where  $S_{ci}$  is the Schmidt number related to species  $i$  and is defined to be  $S_{ci} = \nu/D_i$ . The Schmidt numbers are at *least*  $\mathcal{O}(1)$  within the boundary layer region where the viscous effects dominate that of diffusion. Outside of the boundary-layer we would expect the Schmidt numbers to be at *most*  $\mathcal{O}(1)$  as the diffusion terms become more dominant. The dimensionless mass-flux boundary conditions on the plate are

$$\frac{\partial Y_f}{\partial y} = \theta_f \left[ \frac{Y_f Y_W}{m_W} + \frac{k_2 Y_f Y_D}{m_D} \right], \quad (5.30)$$

$$\frac{\partial Y_h}{\partial y} = 0, \quad (5.31)$$

$$\frac{\partial Y_D}{\partial y} = \theta_D \left[ \frac{k_2 Y_f Y_D}{m_f} - \frac{k_3 Y_M Y_W m_D}{m_M m_W} \right], \quad (5.32)$$

$$\frac{\partial Y_W}{\partial y} = \theta_W \left[ \frac{Y_f Y_W}{m_f} + \frac{k_3 Y_M Y_W}{m_M} \right] - \kappa_W \frac{q_e(x) m_W}{Re^{\frac{1}{2}}}, \quad (5.33)$$

$$\frac{\partial Y_M}{\partial y} = \theta_M \left[ \frac{k_3 Y_M Y_W}{m_W} - \frac{Y_f Y_W m_M}{m_f m_W} - \frac{2k_2 Y_f Y_D m_M}{m_f m_D} \right], \quad (5.34)$$

$$\frac{\partial Y_H}{\partial y} = \kappa_H \frac{q_e(x)}{Re^{\frac{1}{2}}} - \theta_H \left[ \frac{3Y_f Y_W}{m_f m_W} - \frac{2k_2 Y_f Y_D}{m_f m_D} - \frac{k_3 Y_M Y_W}{m_M m_W} \right], \quad (5.35)$$

where the non-dimensional parameters  $\theta_i$  and  $\kappa_i$  are defined to be

$$\theta_i = \frac{k_1 L \rho_{in}}{D_i m_H Re^{\frac{1}{2}}}, \quad \kappa_i = \frac{RT m_H L}{4 D_i F^2 R_s \rho_{in}} \quad (5.36)$$

The boundary conditions at the inlet now become

$$Y_f = \tilde{Y}_f, \quad Y_h = \tilde{Y}_h, \quad Y_W = \tilde{Y}_W, \quad Y_D = 0, \quad Y_M = 0, \quad Y_H = 0, \quad u = 1, \quad v = 0 \quad \text{on } x = 0 \quad (5.37)$$

and in the far field

$$Y_f \rightarrow \tilde{Y}_f, \quad Y_h \rightarrow \tilde{Y}_h, \quad Y_W \rightarrow \tilde{Y}_W, \quad Y_D \rightarrow 0, \quad Y_M \rightarrow 0, \quad Y_H \rightarrow 0, \quad u \rightarrow 1, \quad v \rightarrow 0 \quad \text{as } y \rightarrow \infty \quad (5.38)$$

Finally, the velocity conditions on the plate are

$$u = 0, \quad v = 0 \quad \text{on} \quad y = 0, \quad x > 0 \quad (5.39)$$

## 5.5 Outer region as $Re \rightarrow \infty$

We now seek a solution for the outer inviscid region within the flow. Since there is no homogeneous reaction within this region of our model we can say that the species are only subject to convection and diffusion. We may also assume that within this region there is no feedback from the heterogeneous reactions (5.1)-(5.4). Therefore, we may drop the mass-flux conditions (5.30)-(5.35) within the outer region. As a result we can obtain the exact solution within this region, given by

$$Y_f = \tilde{Y}_f, \quad Y_h = \tilde{Y}_h, \quad Y_W = \tilde{Y}_W, \quad Y_D = 0, \quad Y_M = 0, \quad Y_H = 0, \quad u = 1, \quad v = 0 \quad (5.40)$$

The outer solution represents a uniform flow of reactants without the presence of a reaction. This exactly conforms with the fact that the outer solution is outside of the boundary-layer region and is not affected by the heterogeneous reaction.

## 5.6 Inner region as $Re \rightarrow \infty$

Within the inner region of the boundary-layer we are unable to drop the mass-flux conditions as we did in the outer region. This is due to the heterogeneous reactions and the effects of viscosity within this region of the flow. Therefore, we are required to find a solution to (5.27)-(5.29) subject to the boundary conditions (5.30)-(5.39). Since there is no suction or blowing on the plate we can introduce a transformation which we used in section 3.7. For the readers convenience we will state this again

$$\psi = \xi^{\frac{1}{2}} f(\eta), \quad \text{with} \quad \eta = \frac{y}{x^{\frac{1}{2}}} \quad \text{and} \quad \xi = x, \quad (5.41)$$

where

$$u = \frac{\partial \psi}{\partial y}, \quad v = -\frac{\partial \psi}{\partial x} \quad (5.42)$$

By definition of the stream function variable  $\psi$  we have that the volumetric continuity condition (5.27) is automatically satisfied. As in chapter 3, applying this transformation to the momentum equation (5.28) yields the Blasius equation

$$f''' + \frac{1}{2} f f'' = 0 \quad (5.43)$$

where the primes denote differentiation with respect to the similarity variable  $\eta$ . The momentum boundary conditions under the transformation (5.41) become

$$f'(\infty) = 1, \quad f(0) = f'(0) = 0 \quad (5.44)$$

As we would expect the momentum equation and boundary conditions are completely decoupled from the mass fractions of any of the species. Hence, we can obtain a solution for  $f$  independently but we cannot obtain a solution for the mass fractions without knowing the solution for  $f$ . Therefore, if we substitute the transformation into the convection-diffusion equation (5.29) for all species then we obtain

$$\frac{1}{S_{ci}} \frac{\partial^2 Y_i}{\partial \eta^2} + \frac{1}{2} f \frac{\partial Y_i}{\partial \eta} - x \frac{df}{d\eta} \frac{\partial Y_i}{\partial \xi} = 0 \quad (5.45)$$

subject to the mass flux boundary conditions at the plate

$$\frac{\partial Y_f}{\partial \eta} = \xi^{\frac{1}{2}} \theta_f \left[ \frac{Y_f Y_W}{m_W} + \frac{k_2 Y_f Y_D}{m_D} \right], \quad (5.46)$$

$$\frac{\partial Y_h}{\partial \eta} = 0, \quad (5.47)$$

$$\frac{\partial Y_D}{\partial \eta} = \xi^{\frac{1}{2}} \theta_D \left[ \frac{k_2 Y_f Y_D}{m_f} - \frac{k_3 Y_M Y_W m_D}{m_M m_W} \right], \quad (5.48)$$

$$\frac{\partial Y_W}{\partial \eta} = \xi^{\frac{1}{2}} \left\{ \theta_W \left[ \frac{Y_f Y_W}{m_f} + \frac{k_3 Y_M Y_W}{m_M} \right] - \kappa_W \frac{q_e(\xi) m_W}{Re^{\frac{1}{2}}} \right\}, \quad (5.49)$$

$$\frac{\partial Y_M}{\partial \eta} = \xi^{\frac{1}{2}} \theta_M \left[ \frac{k_3 Y_M Y_W}{m_W} - \frac{Y_f Y_W m_M}{m_f m_W} - \frac{2k_2 Y_f Y_D m_M}{m_f m_D} \right], \quad (5.50)$$

$$\frac{\partial Y_H}{\partial \eta} = \xi^{\frac{1}{2}} \left\{ \kappa_H \frac{q_e(\xi)}{Re^{\frac{1}{2}}} - \theta_H \left[ \frac{3Y_f Y_W}{m_f m_W} - \frac{2k_2 Y_f Y_D}{m_f m_D} - \frac{k_3 Y_M Y_W}{m_M m_W} \right] \right\}, \quad (5.51)$$

and the remaining boundary conditions

$$Y_f = \tilde{Y}_f, \quad Y_h = \tilde{Y}_h, \quad Y_W = \tilde{Y}_W, \quad Y_D = 0, \quad Y_M = 0, \quad Y_H = 0 \quad \text{on} \quad \xi = 0, \quad \eta > 0 \quad (5.52)$$

$$Y_f \rightarrow \tilde{Y}_f, \quad Y_h \rightarrow \tilde{Y}_h, \quad Y_W \rightarrow \tilde{Y}_W, \quad Y_D \rightarrow 0, \quad Y_M \rightarrow 0, \quad Y_H \rightarrow 0 \quad \text{as} \quad \eta \rightarrow \infty, \quad \xi > 0 \quad (5.53)$$

### 5.6.1 Asymptotic solution for $\xi \ll 1$

As we saw in chapter 3 the point  $\xi = 0$ , on the plate, is a singularity within the flow as this is the point where the velocity instantaneously goes from its free stream speed to zero. Therefore, we seek a solution of equations (5.43) and (5.45), subject to the boundary conditions (5.44) and (5.46)-(5.53), for small values of  $\xi$  close to the leading edge of the plate where the singularity occurs. We note from (5.25) that  $q_e(\xi) \sim \mathcal{O}(1)$  and so the mass flux boundary conditions (5.46)-(5.50) suggest that we should look for solutions in the form of the following asymptotic expansions

$$Y_f(\xi, \eta) = a_0 + \xi^{\frac{1}{2}}a_1(\eta) + \xi a_2(\eta) + \xi^{\frac{3}{2}}a_3(\eta), \dots \quad (5.54)$$

$$Y_h(\xi, \eta) = b_0 + \xi^{\frac{1}{2}}b_1(\eta) + \xi b_2(\eta) + \xi^{\frac{3}{2}}b_3(\eta), \dots \quad (5.55)$$

$$Y_D(\xi, \eta) = \xi^{\frac{1}{2}}c_1(\eta) + \xi c_2(\eta) + \xi^{\frac{3}{2}}c_3(\eta), \dots \quad (5.56)$$

$$Y_W(\xi, \eta) = d_0 + \xi^{\frac{1}{2}}d_1(\eta) + \xi d_2(\eta) + \xi^{\frac{3}{2}}d_3(\eta), \dots \quad (5.57)$$

$$Y_M(\xi, \eta) = \xi^{\frac{1}{2}}e_1(\eta) + \xi e_2(\eta) + \xi^{\frac{3}{2}}e_3(\eta), \dots \quad (5.58)$$

where the functions  $a_i$ ,  $b_i$ ,  $c_i$ ,  $d_i$  and  $e_i$  are  $\mathcal{O}(1)$  as  $\xi \rightarrow 0$  and  $a_0 = \tilde{Y}_f$ ,  $b_0 = \tilde{Y}_h$  and  $d_0 = \tilde{Y}_W$  which can be seen from the inlet conditions (5.52). It can be seen above that we have not included an expansion for the mass fraction of hydrogen. The reason behind this is that due to mass continuity we must have  $\sum_i Y_i = 1$  and so as long as we can find a solution to all the other mass fractions we can utilise this fact to find a solution for  $Y_H$ .

Moreover, since helium is inert we do not need to consider a solution for it but just note that we have  $\sum_{i,i \neq h} Y_i = 0.3121$ . However, for completeness we will proceed to include details of the expansions for helium.

Substituting (5.54)-(5.58) into the convection-diffusion equation (5.45) yields the following system of equations in ascending orders of  $\xi$ , for  $\mathcal{O}(\xi^{\frac{1}{2}})$ ,  $\mathcal{O}(\xi)$  and  $\mathcal{O}(\xi^{\frac{3}{2}})$

$$\frac{1}{S_{ci}}\tau_1'' + \frac{f}{2}\tau_1' - \frac{f'}{2}\tau_1 = 0, \quad (5.59)$$

$$\frac{1}{S_{ci}}\tau_2'' + \frac{f}{2}\tau_2' - f'\tau_2 = 0, \quad (5.60)$$

$$\frac{1}{S_{ci}}\tau_3'' + \frac{f}{2}\tau_3' - \frac{3f'}{2}\tau_3 = 0, \quad (5.61)$$

where  $\tau = a, b, c, d, e$ . The following mass-flux boundary conditions for all of the species will be given in terms of ascending powers of  $\xi$ . The conditions for methane are

$$a'_1 = \frac{\theta_f}{m_W} a_0 d_0, \quad (5.62)$$

$$a'_2 = \theta_f \left[ \frac{(a_0 d_1 + a_1 d_0)}{m_W} + \frac{k_2}{m_D} a_0 c_1 \right], \quad (5.63)$$

$$a'_3 = \theta_f \left[ \frac{(a_2 d_0 + a_1 d_1 + a_0 d_2)}{m_W} + \frac{k_2}{m_D} (a_1 c_1 + a_0 c_2) \right] \quad (5.64)$$

The mass-flux conditions for helium are given by

$$b'_1 = 0 \quad (5.65)$$

$$b'_2 = 0 \quad (5.66)$$

$$b'_3 = 0 \quad (5.67)$$

with the conditions for carbon dioxide represented by

$$c'_1 = 0, \quad (5.68)$$

$$c'_2 = \theta_D \left[ \frac{k_2}{m_f} a_0 c_1 - \frac{k_3 m_D}{m_M m_W} d_0 e_1 \right]. \quad (5.69)$$

$$c'_3 = \theta_D \left[ \frac{k_2}{m_f} (a_1 c_1 + a_0 c_2) - \frac{k_3 m_D}{m_M m_W} (d_1 e_1 + d_0 e_2) \right] \quad (5.70)$$

Establishing the equations for the mass-flux conditions of water is slightly more complicated due to the definition of the ion flux density (5.25). Therefore, we are required to substitute the expansions for the species into the equation for  $q_e(\xi)$  and then substitute this into the equation for the mass-flux of water. On doing this we obtain the following

$$d'_1 = \frac{\theta_W}{m_f} a_0 d_0 + \frac{\kappa_W m_W}{Re^{\frac{1}{2}}} \left[ (a_0 + b_0 + d_0) + \frac{1}{2}(a_0 + b_0 + d_0)^2 + \frac{1}{3}(a_0 + b_0 + d_0)^3 - \right. \\ \left. ln(d_0) - \frac{1}{2}ln(Y_O) - \sigma \right], \quad (5.71)$$

$$d'_2 = \theta_W \left[ \frac{(a_1 d_0 + a_0 d_1)}{m_f} + \frac{k_3}{m_M} d_0 e_1 \right] + \\ \frac{\kappa_W m_W}{Re^{\frac{1}{2}}} \left[ (a_1 + b_1 + c_1 + d_1 + e_1) + 2(a_0 + b_0 + d_0)(a_1 + b_1 + c_1 + d_1 + e_1) - \right. \\ \left. (a_0 + b_0 + d_0)^2 (a_1 + b_a + c_1 + d_1 + e_1) + \frac{d_1}{d_0} \right], \quad (5.72)$$

$$d'_3 = \theta_W \left[ \frac{(a_0 d_2 + a_1 d_1 + a_2 d_0)}{m_f} + \frac{k_3}{m_M} (d_1 e_1 + d_0 e_2) \right] + \\ \frac{\kappa_W m_W}{Re^{\frac{1}{2}}} \left[ (a_2 + b_2 + c_2 + d_2 + e_2) + (a_0 + b_0 + d_0)(a_2 + b_2 + c_2 + d_2 + e_2) + \right. \\ \left. \frac{1}{2}(a_1 + b_1 + c_1 + d_1 + e_1)^2 + (a_0 + b_0 + d_0)^2 (a_2 + b_2 + c_2 + d_2 + e_2) + \right. \\ \left. (a_0 + b_0 + d_0)(a_1 + b_1 + c_1 + d_1 + e_1)^2 + \frac{d_2}{d_0} - \frac{1}{2} \left( \frac{d_1}{d_0} \right)^2 \right] \quad (5.73)$$

Finally, the mass-flux boundary conditions for carbon monoxide are

$$e'_1 = -\frac{\theta_M m_M}{m_f m_W} a_0 d_0, \quad (5.74)$$

$$e'_2 = \theta_M \left[ \frac{k_3}{m_W} d_0 e_1 - \frac{m_M}{m_f m_W} (a_1 d_0 + a_0 d_1) - \frac{2k_2 m_M}{m_f m_D} a_0 c_1 \right], \quad (5.75)$$

$$e'_3 = \theta_M \left[ \frac{k_3}{m_W} (d_1 e_1 + d_0 e_2) - \frac{m_M}{m_f m_W} (a_0 d_2 + a_1 d_1 + a_2 d_0) - \frac{2k_2 m_M}{m_f m_D} (a_1 c_1 + a_0 c_2) \right] \quad (5.76)$$

The far field conditions for all of the species are given by

Parameter	Symbol	Value	Units
Molar mass of chemical species	$m_i$	$m_H=0.002$	$kg\ mol^{-1}$
		$m_W=0.018$	$kg\ mol^{-1}$
		$m_f=0.016$	$kg\ mol^{-1}$
		$m_O=0.032$	$kg\ mol^{-1}$
		$m_D=0.044$	$kg\ mol^{-1}$
		$m_h=0.004$	$kg\ mol^{-1}$
Inlet mass fractions of species	$\tilde{Y}_i$	$\tilde{Y}_f = 0.2548$	
		$\tilde{Y}_W = 0.0573$	
		$\tilde{Y}_h = 0.6879$	
Species diffusivity	$D_i$	$10^{-4}$	$m^2\ s^{-1}$
Faraday's constant	$F$	96485	$C\ mol^{-1}$
Gas constant	$R$	8.3144	$J\ K^{-1}\ mol^{-1}$
Temperature	$T$	1000	$K$
Input gas density	$\rho_{in}$	0.0561	$kg\ m^{-3}$
Anode length	$L$	$O(10^{-1})$	$m$
Specific resistance of zirconia	$R_s$	$1.707 \times 10^{-4}$	$\Omega\ m^2$
Viscosity	$\mu$	$4.606 \times 10^{-5}$	$kg\ m^{-1}\ s^{-1}$
Inlet velocity	$U_0$	$O(10^{-1}) - O(1)$	$m\ s^{-1}$
Ideal potential	$U^r$	0.99	$V$
Cell potential	$U_{cell}$	0-1.2	$V$
Steam reforming reaction rate	$k_1$	$1.61 \times 10^{13}$	$mol\ m^{-4}\ s^{-1}$

Table 5.1: Parameters, their symbols, values and units

$$\tau_1(\eta) \rightarrow 0, \quad \tau_2(\eta) \rightarrow 0, \quad \tau_3(\eta) \rightarrow 0 \quad \text{as} \quad \eta \rightarrow \infty \quad (5.77)$$

The result of these expansions gives a set of boundary value problems which we are required to solve together in order to generate a solution for the momentum and mass fractions of each of the species. Once again we solve the above problem using the shooting method alongside the parameter and dimensionless parameters given in Tables 5.1 and 5.2

Symbol	Typical value	Description
$Re$	$O(10^2)$	Reynolds Number = $\frac{\text{inertial forces}}{\text{viscous forces}}$
$S_{ci}$	$O(1)$	Schmidt number = $\frac{\text{viscous forces}}{\text{diffusive forces}}$
$\sigma$	$24.65 - (-3)$	
$\kappa_i$	$4.6632 \times 10^{-4}$	$\frac{\text{electrochemical flux of hydrogen}}{\text{diffusive flux of hydrogen}}$
$\theta_i$	$4.5161 \times 10^{14}$	
$\bar{k}_1, \bar{k}_2$	$6.2112 \times 10^{-8}$	Dimensionless reaction rates

Table 5.2: Definitions of dimensionless parameters and their typical values

## 5.7 Results and Discussion

We now seek a numerical solution to the model equations (5.45) subject to the boundary conditions (5.46)-(5.53). The numerical solution for the momentum within the model is taken from the results of the shooting method within the asymptotic analysis. The numerical method which is utilised to solve the above system is given in section 3.8.1. It should be noted here that the mass fraction of helium is omitted from the numerical solutions, since helium is inert, and the remaining mass fractions of species have been scaled up such that

$$Y_f + Y_W + Y_M + Y_D + Y_H = 1. \quad (5.78)$$

Fig. 5.1 shows a plot of the mass fraction of methane within the transformed coordinate system  $(\xi, \eta)$  for a constant cell potential  $U_{cell} = 0.5$ . We can see that close to the leading edge of the plate there is a severe reduction in the mass fraction of methane and that after this point the reaction rate slows. Since  $Y_f$  is not directly dependent on the ion flux density we need to examine our initial reaction structure to justify this reduction. From (5.1)-(5.3) we can see that the mass fraction of methane depends on that of water and carbon dioxide and so it is the depletion of these species that slows the reaction rate of methane.

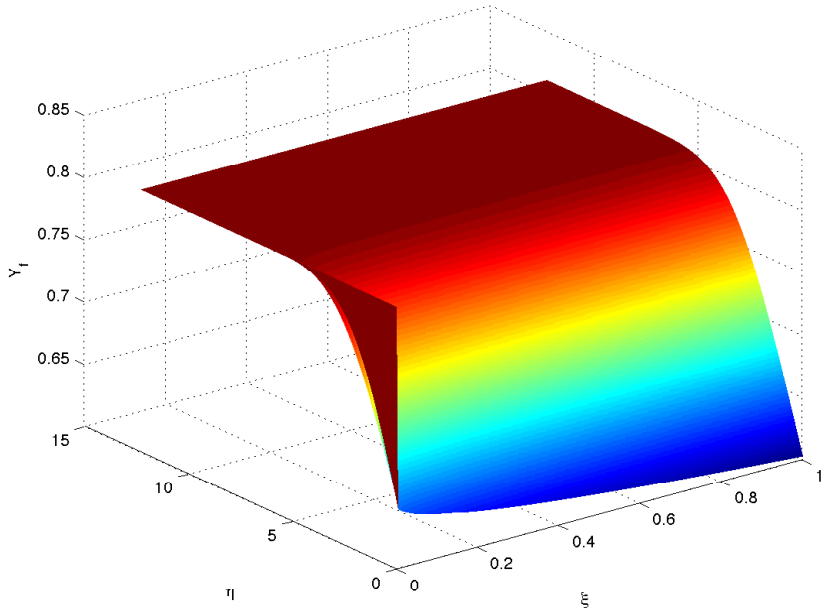


Figure 5.1:  $Y_f$  plotted against the coordinate system  $(\xi, \eta)$  for  $U_{cell} = 0.5$ . This demonstrates how the mass fraction of methane varies throughout the flow domain.

One of the causes of slow methane reaction away from the leading edge is demonstrated in Fig. 5.2 where the mass fraction of water has been plotted in the coordinate system  $(\xi, \eta)$  for a constant cell potential of  $U_{cell} = 0.5$ . It can be seen from this plot that the mass fraction of water becomes negligible after the leading edge of the plate. This is due to the species being consumed within reaction (5.1) and this reduction is species aligns with that of methane in Fig. 5.1. Therefore, since there is little water present after this points reaction (5.1) is effectively switched off. Some water will still be produced from (5.4) which means that reaction (5.1) will still occur but the effects will be small.

Fig. 5.3 plots the mass fraction of carbon monoxide with the domain  $(\xi, \eta)$  for a constant cell potential  $U_{cell} = 0.5$ . This plots demonstrates a significant increase in the mass fraction of carbon monoxide close to the leading edge, aligning with the reduction in methane from reaction (5.1), and that after this point the reaction rate slows. Due to the negligible presence of water after the leading edge reaction (5.3) is also effectively

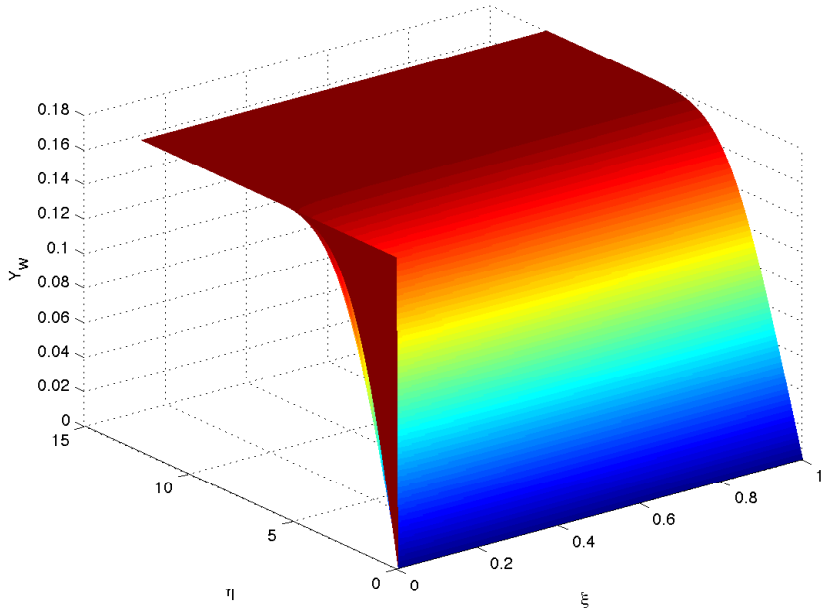


Figure 5.2:  $Y_W$  plotted against the coordinate system  $(\xi, \eta)$  for  $U_{cell} = 0.5$ . This demonstrates how the mass fraction of water varies throughout the flow domain.

switched off and as a result the carbon monoxide becomes a significant proportion of the overall species within the cell.

The mass fraction of hydrogen within the domain  $(\xi, \eta)$  for constant cell potential  $U_{cell} = 0.5$  is plotted in Fig. 5.4. Here the mass fraction of hydrogen greatly increases at the leading edge due to the severity of reactions (5.1)-(5.3) around this point. Due to the depletion of water and carbon dioxide, to be explained later, these reactions become negligible after this point and as such very little hydrogen is produced. Therefore, the reduction in hydrogen after the leading edge is due to the hydrogen oxidation reaction (5.4). The reaction rate of this reaction appears to be significantly less than that of the other reactions within the model. Hence, very little water is produced from this reaction and any water that is produced is rapidly consumed by reactions (5.1) and (5.3).

The mass fraction of carbon dioxide has not been plotted within this work. The reason for this is due to the negligible amount of the species present throughout the flow

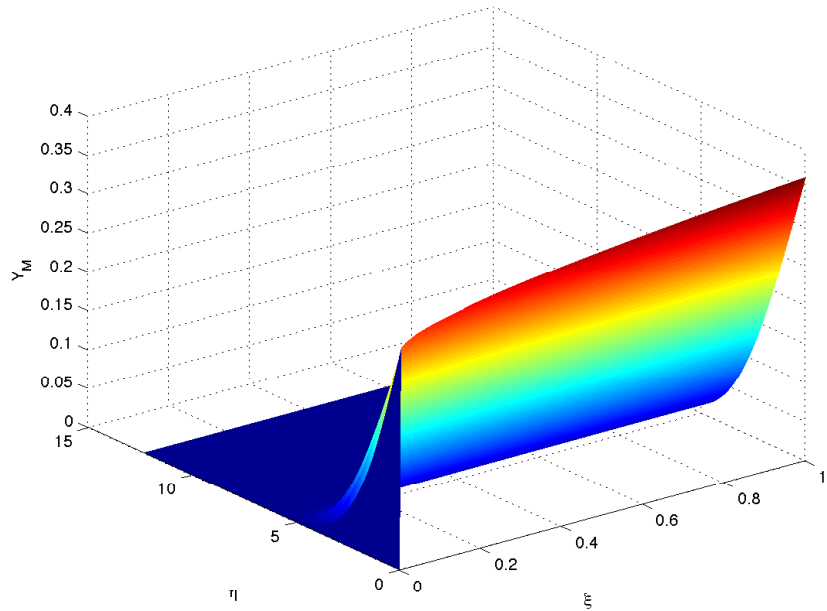


Figure 5.3:  $Y_M$  plotted against the coordinate system  $(\xi, \eta)$  for  $U_{cell} = 0.5$ . This demonstrates how the mass fraction of carbon monoxide varies throughout the flow domain.

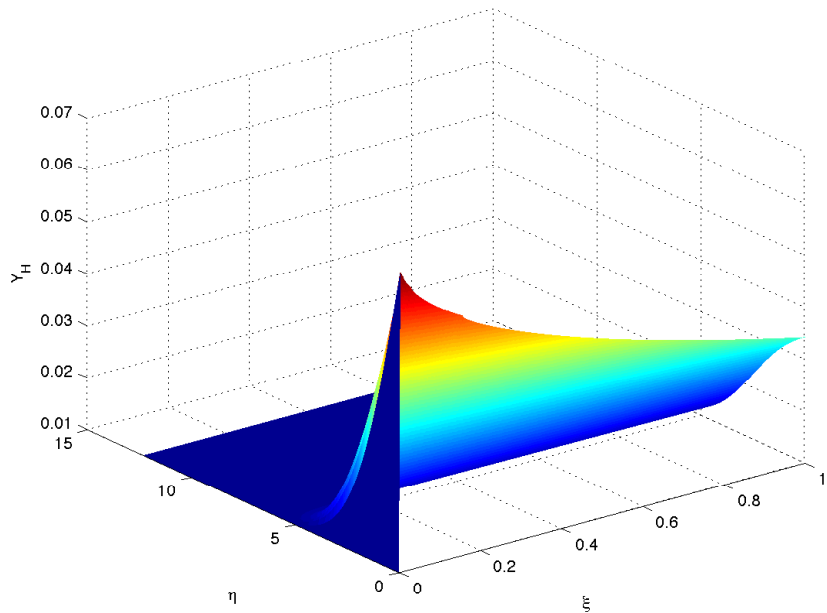


Figure 5.4:  $Y_H$  plotted against the coordinate system  $(\xi, \eta)$  for  $U_{cell} = 0.5$ . This demonstrates how the mass fraction of hydrogen varies throughout the flow domain.

domain. It should be noted that although this amount is negligible it still contributes to the reduction of methane within reaction (5.2). It should be noted here that the mass fractions of species may vary from those demonstrated within experimental work due to the assumptions that the reaction structure is irreversible.

To produce I-V and current-power plots from this model we are required to understand how the mass fractions of all the species vary when the cell potential is not treated as a constant. Therefore, we examine the production and consumption of species along the plate when  $U_{cell}$  is taken to be a variable.

Fig. 5.5 plots the mass fraction of methane along the surface of the plate for varying values of  $U_{cell}$ . Although the severity of the reaction at the leading edge is still high for all values of  $U_{cell}$  the mass fraction of methane does increase for increasing values of  $U_{cell}$ . The reason for this is that for larger values of  $U_{cell}$  the hydrogen oxidation reaction rate becomes slower. As a result the amount of water that is produced from this reaction is less than that for lower values of  $U_{cell}$ . Therefore, the reaction rate for the steam reforming of methane reduces because of this reduction in water production.

The surface mass fraction of water for varying  $U_{cell}$ , plotted in Fig. 5.6, demonstrates the same profile for all values of cell potential. The reduction in water is severe at the leading edge and become negligible away from this point. Although less water will be produced from the hydrogen oxidation reaction (5.4) any water that is produced is immediately consumed by the reactions (5.1) and (5.3).

Fig. 5.7 plots the surface mass fraction of carbon monoxide for varying values of  $U_{cell}$ . Again the severity of the reaction rate close to the leading edge is high for all values of  $U_{cell}$ . However, away from this point the mass fraction of carbon monoxide increases for increasing cell potential. This is due to the reduction in water consumption from the hydrogen oxidation reaction resulting in a reduction in carbon monoxide production through reaction (5.1).

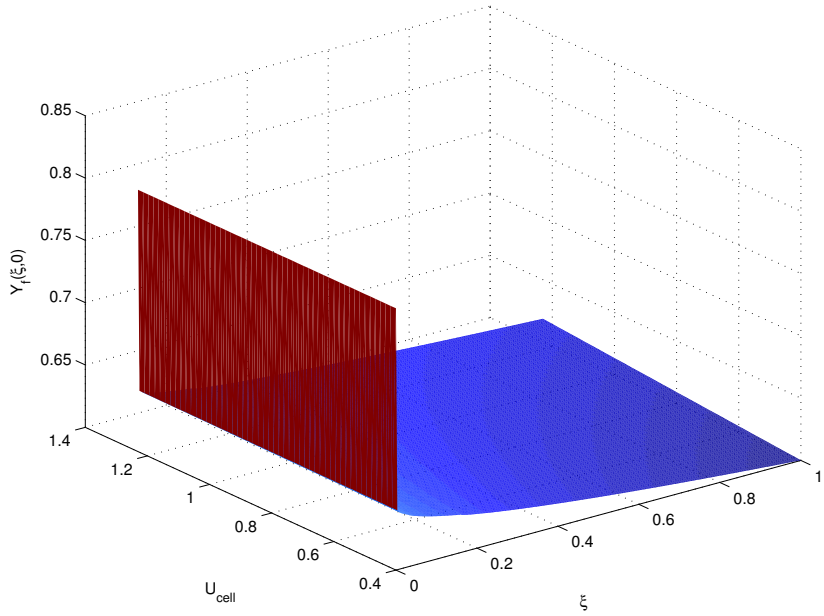


Figure 5.5: Plot of the surface mass fraction of methane,  $Y_f(\xi, 0)$ , against  $\xi$  and varying values of  $U_{cell}$ . This demonstrates how the surface mass fraction of methane varies for all considered cell potentials.

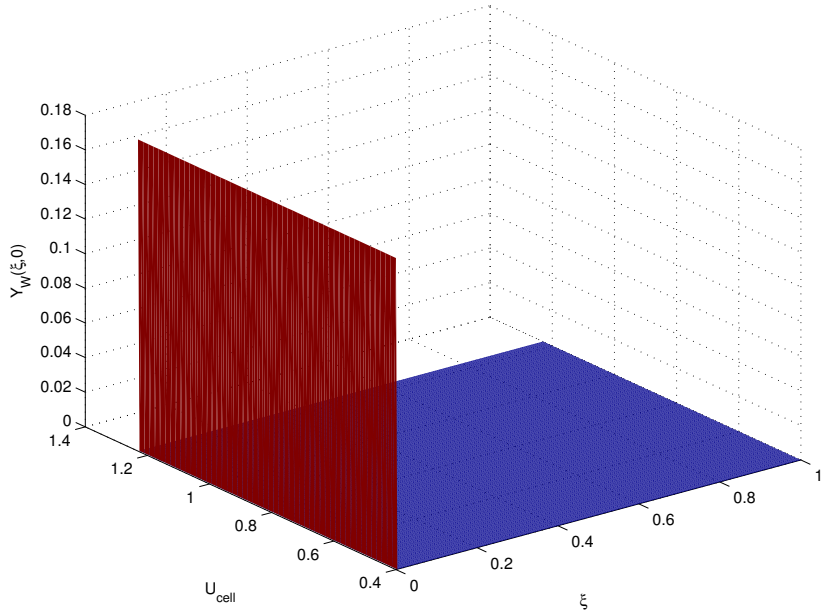


Figure 5.6: Plot of the surface mass fraction of water,  $Y_W(\xi, 0)$ , against  $\xi$  and varying values of  $U_{cell}$ . This demonstrates how the surface mass fraction of water varies for all considered cell potentials.

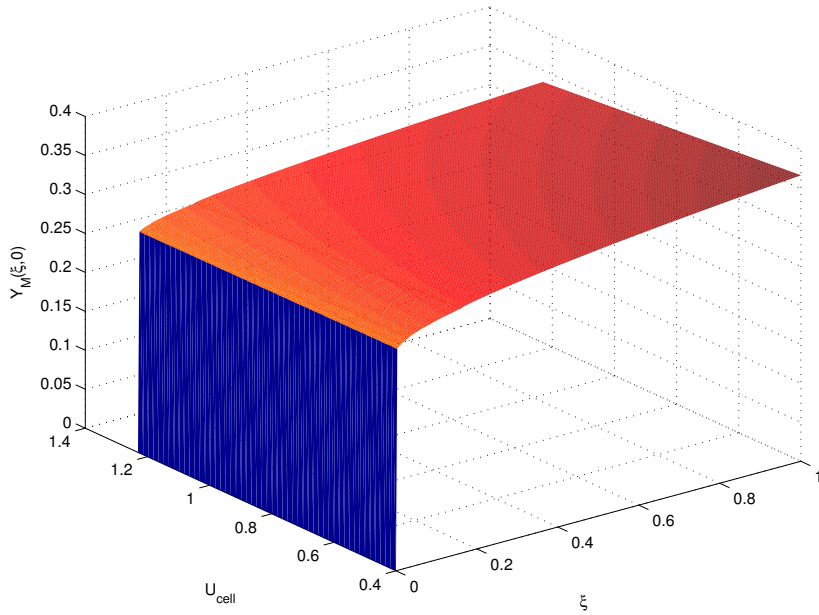


Figure 5.7: Plot of the surface mass fraction of carbon monoxide,  $Y_M(\xi, 0)$ , against  $\xi$  and varying values of  $U_{cell}$ . This demonstrates how the surface mass fraction of carbon monoxide varies for all considered cell potentials.

The surface mass fraction of hydrogen for varying values of  $U_{cell}$  is plotted in Fig. 5.8. here we can see that the hydrogen is produced rapidly at the leading edge of the plate due to the severity of the reactions rates in (5.1)-(5.3). As we have stated, after this point the the reactions (5.1)-(5.3) are effectively switched off and as a result hydrogen is only consumed within the hydrogen oxidation reaction (5.4). This therefore accounts for the reduction in the surface mass fraction of hydrogen along the plate. Moreover, the mass fraction of hydrogen increases for increasing values of  $U_{cell}$ . this is due to (5.4) having a lower reaction rate for higher values of  $U_{cell}$  and because the remaining reactions have limited effect due to the depletion of water and carbon dioxide.

## 5.8 Electrical Model

The set up for the electrical model is identical to that shown within chapter 4. Therefore, the details for the electrical model are omitted in this case but can be referred to in the

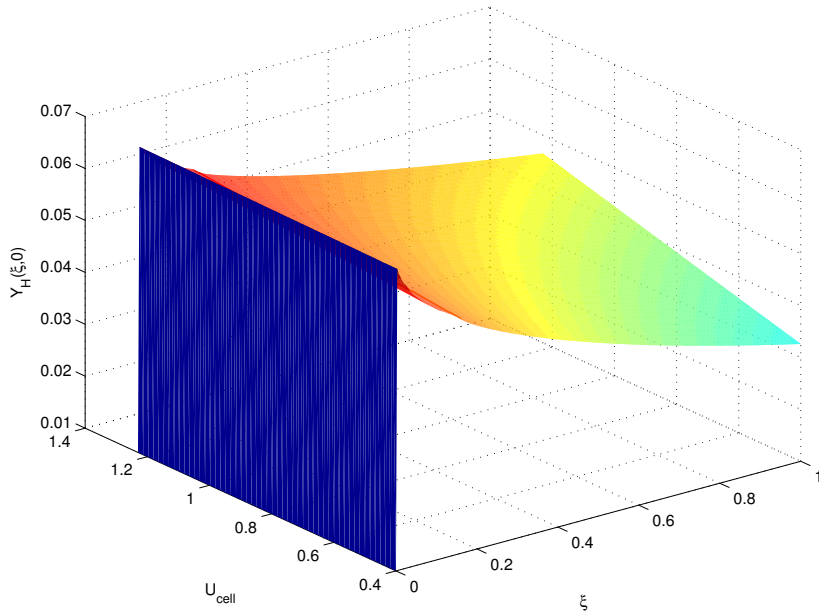


Figure 5.8: Plot of the surface mass fraction of hydrogen,  $Y_H(\xi, 0)$ , against  $\xi$  and varying values of  $U_{cell}$ . This demonstrates how the surface mass fraction of hydrogen varies for all considered cell potentials.

referenced chapter. The behaviour of the IV and current-power curves for cell position are also identical to those in sections 4.1 and 4.2 with the greatest power production being produced at the leading edge of the plate, due to the ion flux density taking its greatest value at this point.

Fig. 5.9 plots the average IV and current-power curves across the surface of the plate  $0 \leq \xi \leq 1$ . From this plot we can see that the cell potential decreases with increasing current density. Furthermore, due to the linear relationship between the current density and cell potential we have a quadratic relationship between the current density and power density of the cell. The maximum achievable power density from the model inputs is  $0.3415 \text{ W cm}^{-2}$  which occurs at the current density of  $0.5862 \text{ A cm}^{-2}$ . If we map this current density to the cell potential we obtain an optimal operating cell potential of  $0.5826 \text{ V}$ .

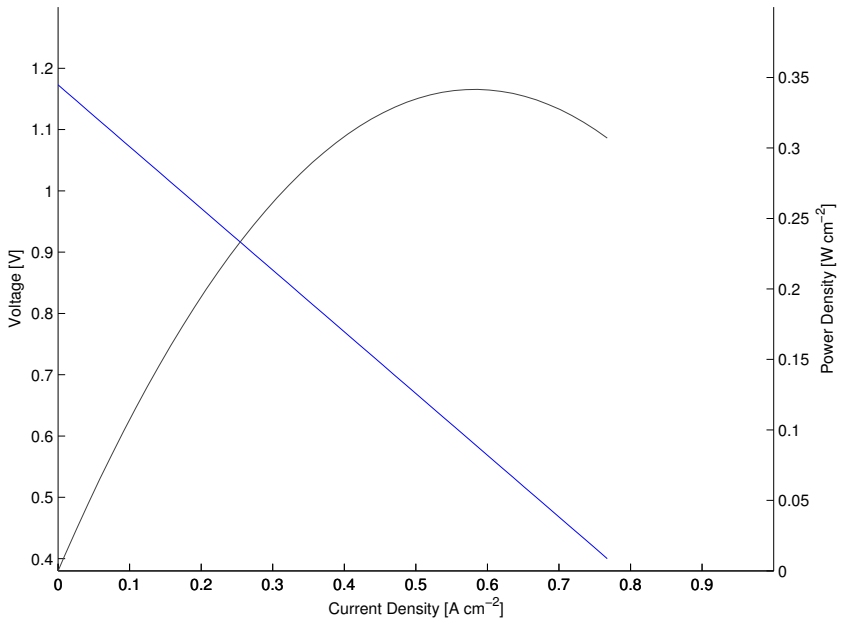


Figure 5.9: Average current-voltage (blue line) and current-power (black line) curves across the length of the cell  $0 \leq \xi \leq 1$ . These plots demonstrate the relationship between the cell voltage and current density as well as the cell power density and current density within this model.

## 5.9 Chapter Summary

Within this chapter we have examined the flow and heterogeneous reaction of humidified methane, adapting the model in chapter 3. This chapter gives a demonstration of how the analytical and numerical framework developed in chapter 3 can be applied to planar SOFCs operating under alternative conditions. Therefore, this highlights the versatility of this modelling approach.

This model has demonstrated how the hydrogen oxidation reaction depends on the full reaction structure of humidified methane. Therefore, this demonstrates how the electrical performance of the cell depends on the initial inlet mixture. The electrical performance of this model has been solved and can be seen to produce a higher achievable power density compared to the humidified hydrogen case.

In the proceeding chapter we will challenge the assumptions in chapters 3 and 5 to

align the more more closely with an operating planar SOFC.

# CHAPTER 6

## COMPRESSIBLE HETEROGENEOUS REACTION IN BOUNDARY-LAYER FLOW WITH ELECTROCHEMISTRY

### 6.1 Model description

We have demonstrated in chapters 3-5 the flow and reaction of an incompressible mixture of species over a flat, semi-infinite, impermeable plate. Furthermore, we have given details on the electrical performance of both these models by drawing comparisons with SOFCs. However, the limitations of these models occur in the assumption that the flow remains incompressible throughout the entire reaction process. Although this is an appropriate initial assumption to make, mainly due to the added simplicity and density variations at high temperatures, we can improve on the initial models by now taking the flow to be compressible. We would expect to see variable density within the model due to the composition of the mixture changing as we move along the surface of the plate. However, as we will demonstrate, there are added considerations to take when examining a compressible system compared to an incompressible case.

The model set up will take the same form as that outlined in chapter 3. Therefore, we will consider an inlet mixture of humidified hydrogen (97% Hydrogen and 3% Water) which is forcefully convected across a flat, semi-infinite, impermeable plate which is coated in a nickel based catalyst. The reaction which occurs on the surface of the plate will take the form of the hydrogen oxidation reaction



Once again we will consider the mixture to be well mix as it approaches the plate with a uniform velocity of  $U_0$ . Moreover, we will assume that the plate has a typical length scale  $L$ , which we can assume to be the length of the plate. The difference with this model is that we will now consider compressibility and so we no longer assume constant density throughout the flow. Moreover, we will also be assuming non-constant mixture viscosity, due to the mixture composition varying, and a non-isothermal system. Although Fig. 3.3 demonstrates that SOFCs are an almost isothermal system we can see that there are slight temperature variations and there is a link between density and temperature which we will show later.

## 6.2 Mathematical model

The mathematical models used in chapters 3 and 5 are no longer relevant here due to the assumption that the flow is now compressible. Therefore, we are required to generate an alternative mathematical model in order to incorporate this new assumption.

The conservation of momentum within this model is governed by the boundary-layer equations, which take the alternative form within this set-up

$$u \frac{\partial u}{\partial x} + v \frac{\partial u}{\partial y} = -\frac{1}{\rho} \frac{dP}{dx} + \nu \frac{\partial^2 u}{\partial y^2}, \quad (6.2)$$

$$0 = \frac{\partial P}{\partial y} \quad (6.3)$$

where  $u$  and  $v$  are the streamwise and transverse velocity components and  $x$  and  $y$  are the streamwise and transverse coordinates. In this model the density,  $\rho$ , pressure,  $P$ , and kinematic viscosity,  $\nu$ , are all variables. Now taking into account the compressibility of the model yields the following volumetric continuity equation

$$\frac{\partial(\rho u)}{\partial x} + \frac{\partial(\rho v)}{\partial y} = 0, \quad (6.4)$$

To define the equation for the conservation of species within our domain we need to revert our attention back to equation (3.12). Here we used the facts that the homogeneous reaction rate was zero and that the velocity of particular species could be related to the diffusion velocity of those species and the combined mixture velocity. This equation is still valid for this particular model with the only variation occurring from the fact that we no longer have a constant density and as such we are unable to cancel the density term from each side of this equation. Therefore, if we incorporate Fick's law into (3.12) then we obtain the conservation of mass equation

$$\nabla \cdot (\rho D_i \nabla Y_i) = \rho(\mathbf{v} \cdot \nabla) Y_i \quad (6.5)$$

As was explained within the model description we are now going to examine the case where the system is non-isothermal and as a result temperature variations will occur. We have seen previously in Fig. 3.3 that the experimentally observed variations in temperature are small and thus we would expect to see this occurrence within our model.

Hence, we require an equation the governs the temperature distribution within our model domain. Such an equation will take the form of the energy equation, given by

$$u \frac{\partial T}{\partial x} + v \frac{\partial T}{\partial y} = \frac{u}{\rho C_p} \frac{dP}{dx} + \frac{1}{\rho C_p} \frac{\partial}{\partial y} \left( k \frac{\partial T}{\partial y} \right) + \frac{\mu}{\rho C_p} \left( \frac{\partial u}{\partial y} \right)^2 \quad (6.6)$$

where  $T$  is the absolute temperature,  $C_p$  is the heat capacity at constant pressure,  $k$  is the thermal conductivity of our mixture of gases and  $\mu$  is the dynamic viscosity of the mixture. Equations (6.2)-(6.6) represent the governing equations for the velocity, mass fraction and temperature within our model. The focus now is to establish similar equations for the density, pressure and dynamic viscosity.

In order to calculate the pressure with the flow we utilise the equation of state which is written here as

$$P = \rho R T \sum_i \frac{Y_i}{m_i} \quad (6.7)$$

We can see from this equation that we do not need to explicitly solve  $P$ , rather we only need to solve for  $\rho$ ,  $T$  and  $Y_i$ . This will save computational time and storage later on which will increase the overall efficiency of the model. For the dynamic viscosity we use the method of Bromley & Wilke (1951) for the mixing rule of a gaseous mixture at low pressures

$$\mu = \sum_{i=1}^n \frac{\mu_i}{1 + \frac{1}{X_i} \sum_{l=1, l \neq i}^n X_l \phi_{il}} \quad (6.8)$$

where  $\mu_i$  is the species kinematic viscosity,  $X_i$  is the mole fraction of species and  $\phi_{i,l}$  is called an interaction parameter. In this case the interaction parameter is given by

$$\phi_{il} = \frac{\left[1 + \left(\frac{\mu_i}{\mu_l}\right)^{\frac{1}{2}} \left(\frac{m_l}{m_i}\right)^{\frac{1}{4}}\right]^2}{\sqrt{8} \left[1 + \frac{m_i}{m_l}\right]^{\frac{1}{2}}} \quad (6.9)$$

One can calculate the values of the coefficients of viscosity for each chemical species at normal pressure and up to 5000 K by examining Krieger (1951). Finally for the mixture density we use the relationship

$$\rho = \frac{\rho_H \rho_W}{Y_H \rho_W + Y_W \rho_H} \quad (6.10)$$

Therefore, we have expressed the mixture viscosity and density in terms of the mass fractions of species and several parameter values. Hence, as with the equation of state for pressure (6.7) we need not solve the mixture viscosity and density explicitly thus saving computational time and increasing efficiency. For simplicity we will assume that within this model the mixture thermal conductivity and specific heat capacity at constant pressure remain constant throughout. It is possible to define equations for both of these physical properties and details of these can be found in appendix C.

The electrochemistry that we will use to define the rate of reaction is identical to that used in chapters 3 and 5. Therefore, we will just give the very basic details in this section and leave the reader to examine the details in the aforementioned chapters. The current density of the cell is proportional to the ion flux density, via the equation

$$i(x) = 2F q_e(x), \quad (6.11)$$

where  $i(x)$  is the local current density,  $F$  is Faraday's constant and  $q_e(x)$  is the local ion flux density. The equation for the overall cell potential remains the same as that of previous chapters and is given by

$$U_{cell} = U^N - \sum_i \eta_i, \quad (6.12)$$

where we take

$$\sum_i \eta_i = i(x)R_s \quad (6.13)$$

On utilising the Nernst equation (2.9), (3.15) and (5.11) we obtain the equation for the ion flux density

$$q_e(x) = \frac{RT}{4F^2R_s} \left[ \ln \left( \frac{Y_H Y_O^{\frac{1}{2}}}{Y_W} \right) + \ln \left( \frac{m_W(\rho_a R T_a)^{\frac{1}{2}}}{m_H m_O^{\frac{1}{2}}} \right) + \frac{2F}{RT} (U^r - U_{cell}) \right] \quad (6.14)$$

where  $\rho_a$  and  $T_a$  are the constant values of density and temperature on the air side of the fuel cell.

### 6.3 Boundary conditions

We have now established the governing equations for the conservation of mass (6.5), momentum (6.2)-(6.4) and energy (6.6) as well as equations governing the pressure (6.7), mixture viscosity (6.8) and mixture density (6.10) within the given domain. Moreover, we have set-up the underlying electrochemistry which gives details on the local ion flux density (6.14). We are now required to give details regarding the boundary conditions at the inlet, in the far field and on the surface of the plate. In section 6.1 we described the initial flow as uniform and that the initial mixture consisted of humidified hydrogen. Therefore, we begin by stating the initial boundary conditions for the model which are given by

$$Y_H = \tilde{Y}_H, Y_W = \tilde{Y}_W, u = U_0, v = 0, T = T_0, P = P_0, \rho = \rho_0 \quad \text{on } x = 0, y > 0 \quad (6.15)$$

In the far field we assume there is no feedback from the chemical reaction and as a result the momentum, species mass and temperature should not be affected. Hence, the boundary conditions in the far field are given by

$$Y_H \rightarrow \tilde{Y}_H, Y_W \rightarrow \tilde{Y}_W, u \rightarrow U_0, v \rightarrow 0, T \rightarrow T_0, P \rightarrow P_0, \rho \rightarrow \rho_0 \quad \text{as } y \rightarrow \infty, x > 0 \quad (6.16)$$

Since the surface of the plate is impermeable to gas species and the plate is stationary we have a no-slip condition for the velocity components on its surface. This implies that the boundary conditions for velocity of the surface of the plate are represented by

$$u = 0, v = 0 \quad \text{on } y = 0, x > 0 \quad (6.17)$$

It now remains to give details regarding the boundary conditions for species, temperature, pressure and density along the surface of the plate.

The boundary conditions for the variation of species along the plate were shown in section 3.4. However, for completeness we will give details of them here

$$D_H \frac{\partial Y_H}{\partial y} = \frac{q_e(x)m_H}{\rho}, \quad (6.18)$$

$$D_W \frac{\partial Y_W}{\partial y} = -\frac{q_e(x)m_W}{\rho}, \quad (6.19)$$

where  $D_i$  is the species diffusion coefficient and  $m_i$  is the species molar mass. For the

surface temperature variations we take our inspiration from Merkin & Chaudhary (1994) and Chaudhary & Merkin (1995) where we link the change in surface temperature to the reaction rate of reaction (6.1). It should be stated here that reaction (6.1) is exothermic and as a result heat will be produced from this reaction taking place. Therefore, we obtain the boundary condition for temperature on the surface of the plate

$$k \frac{\partial T}{\partial y} = -Q q_e(x) \quad (6.20)$$

where the parameter  $Q$  is the heat released in the reaction. This parameter can be calculated by multiplying the enthalpy change of combustion by the number of moles of the reactant.

We have seen how the pressure, density and viscosity can all be determined from the mass fraction of species and the temperature. Therefore, we do not need to explicitly define the boundary conditions for these variables. For the readers interest, the obvious boundary condition for pressure arises from substitution of the no slip condition (6.17) into the momentum equation (6.2) which yields

$$\frac{dP}{dx} = \mu \frac{\partial^2 u}{\partial y^2} \quad (6.21)$$

## 6.4 Non-dimensionalisation

The governing equations (6.2)-(6.10) and their corresponding boundary conditions (6.15)-(6.21) are all currently in dimensional form. Therefore, we now introduce the following set of non-dimensional variables

$$\begin{aligned}\bar{m}_i &= \frac{m_i}{m_H}, \quad \bar{\rho} = \frac{\rho}{\rho_0}, \quad u = U_0 \bar{u}, \quad v = U_0 R e^{-\frac{1}{2} \bar{v}}, \quad \bar{x} = \frac{x}{L}, \quad \bar{y} = \frac{y R e^{\frac{1}{2}}}{L}, \quad \bar{\mu} = \frac{\mu}{\mu_0} \\ \bar{q}_e(x) &= \frac{4F^2 R_s}{RT_0} q_e(x), \quad \bar{T} = \frac{T}{T_0}, \quad \bar{P} = \frac{P}{U_0^2 \rho_0}, \quad \bar{\nu} = \frac{\bar{\mu}}{\bar{\rho}}\end{aligned}\quad (6.22)$$

If we apply these new variables to the ion flux density equation (6.14) then we obtain (on dropping the bars for convenience)

$$q_e(x) = T \left[ \ln \left( \frac{Y_H Y_O^{\frac{1}{2}}}{Y_W} \right) + \frac{\Gamma}{T} + \sigma \right] \quad (6.23)$$

where the parameter  $\sigma$  is given by

$$\sigma = \ln \left( \frac{m_W (\rho_a R T_a)^{\frac{1}{2}}}{m_O^{\frac{1}{2}} m_H^{\frac{1}{2}}} \right) \quad (6.24)$$

and the parameter  $\Gamma$  is given by

$$\Gamma = \frac{2F(U^r - U_{cell})}{RT_0} \quad (6.25)$$

If we now apply the non-dimensional variables to the governing equations then we obtain

$$\frac{\partial(\rho u)}{\partial x} + \frac{\partial(\rho v)}{\partial y} = 0, \quad (6.26)$$

$$u \frac{\partial u}{\partial x} + v \frac{\partial u}{\partial y} = - \frac{1}{\rho} \frac{dP}{dx} + \nu \frac{\partial^2 u}{\partial y^2}, \quad (6.27)$$

$$\frac{1}{S_c} \frac{\partial}{\partial y} \left( \rho_f \frac{\partial Y_H}{\partial y} \right) = \rho_f \left( u_f \frac{\partial Y_H}{\partial x} + v_f \frac{\partial Y_H}{\partial y} \right), \quad (6.28)$$

$$\frac{\delta}{S_c} \frac{\partial}{\partial y} \left( \rho \frac{\partial Y_W}{\partial y} \right) = \rho \left( u \frac{\partial Y_W}{\partial x} + v \frac{\partial Y_W}{\partial y} \right), \quad (6.29)$$

$$u \frac{\partial T}{\partial x} + v \frac{\partial T}{\partial y} = E \frac{u}{\rho} \frac{dP}{dx} + \frac{1}{Pr \rho} \frac{\partial^2 T}{\partial y^2} + E \nu \left( \frac{\partial u}{\partial y} \right)^2 \quad (6.30)$$

where the Reynolds number, Schmidt number, Eckert number and Prandtl number are given by

$$Re = \frac{U_0 L}{\nu_0}, \quad S_c = \frac{\nu}{D_H}, \quad E = \frac{U_0^2}{C_p T_0}, \quad Pr = \frac{\nu_0}{\alpha}, \quad \alpha = \frac{k}{\rho_0 C_p} \quad (6.31)$$

As with the models developed in previous chapters we require the Schmidt number to be at *least*  $\mathcal{O}(1)$  within the velocity boundary-layer and at *most*  $\mathcal{O}(1)$  in the far field. The Prandtl number  $Pr$  defines the ratio between viscous diffusion and thermal diffusion. This number is the most important characteristic for thermal boundary layers and forced convection due to thermal changes (Schlichting & Gersten, 2004). The Prandtl number dictates the thickness of the thermal boundary-layer since for  $Pr > 1$  we have that the thermal boundary-layer lies within the velocity boundary-layer and for  $Pr < 1$  we have the opposite occurrence (Bird *et al.*, 2006). This is particularly important when dealing with gases as the Prandtl number for gases is typically  $\mathcal{O}(1)$  (Bird *et al.*, 2006; Johnson, 1998). Within this model we have used the Prandtl number for a mixture of gases rather than for particular species. The Eckert number defines the ratio between kinetic energy and the enthalpy within the flow.

The parameter  $\delta$  in equation (6.29) is given by

$$\delta = \frac{D_W}{D_H} \quad (6.32)$$

The equation of state (6.7) now becomes

$$P = \beta \rho T \left( Y_H + \frac{Y_W}{m_W} \right) \quad (6.33)$$

where the dimensionless parameter  $\beta$  is given by

$$\beta = \frac{RT_0}{U_0^2 m_H} \quad (6.34)$$

The non-dimensional equation for the mixture viscosity now takes the form

$$\mu = \frac{Y_H m_w \mu_H}{\mu_0(Y_H m_W + Y_W \phi_{HW})} + \frac{Y_W \mu_W}{\mu_0(Y_W + Y_H m_W \phi_{WH})} \quad (6.35)$$

where the interaction parameters  $\phi_{HW}$  and  $\phi_{WH}$  become

$$\phi_{HW} = \frac{\left[1 + \left(\frac{\mu_H}{\mu_W}\right)^{\frac{1}{2}} m_W^{\frac{1}{4}}\right]^2}{\left[8\left(1 + \frac{1}{m_W}\right)\right]^{\frac{1}{2}}} \quad \phi_{WH} = \frac{\left[1 + \left(\frac{\mu_W}{\mu_H}\right)^{\frac{1}{2}} \left(\frac{1}{m_W}\right)^{\frac{1}{4}}\right]^2}{[8(1 + m_W)]^{\frac{1}{2}}} \quad (6.36)$$

If we substitute the non-dimensional variables (6.22) into the density mixture equation (6.10) we obtain

$$\rho = \frac{\rho_H \rho_W}{\rho_0(Y_H \rho_W + Y_W \rho_H)} \quad (6.37)$$

The boundary conditions at the inlet of the cell become

$$Y_H = \tilde{Y}_H, \quad Y_W = \tilde{Y}_W, \quad u = 1, \quad v = 0, \quad T = 1, \quad P = \tilde{P}, \quad \rho = 1 \quad \text{on} \quad x = 0, \quad y > 0 \quad (6.38)$$

where

$$\tilde{P} = \frac{P_0}{U_0^2 \rho} \quad (6.39)$$

Now in the far field the boundary conditions are represented by

$$Y_H \rightarrow \tilde{Y}_H, \quad Y_W \rightarrow \tilde{Y}_W, \quad u \rightarrow 1, \quad v \rightarrow 0, \quad T \rightarrow 1, \quad P \rightarrow \tilde{P}, \quad \rho \rightarrow 1 \quad \text{as} \quad y \rightarrow \infty, \quad x > 0 \quad (6.40)$$

and the velocity boundary conditions on the surface of the plate are

$$u = 0, \quad v = 0 \quad \text{on} \quad y = 0, \quad x > 0 \quad (6.41)$$

The dimensionless mass-flux boundary conditions on the surface of the plate become

$$\frac{\partial Y_H}{\partial y} = \frac{\lambda}{Re^{\frac{1}{2}}} \frac{q_e(x)}{\rho_f}, \quad (6.42)$$

$$\frac{\partial Y_W}{\partial y} = - \frac{\lambda m_W}{Re^{\frac{1}{2}} \delta} \frac{q_e(x)}{\rho_f} \quad (6.43)$$

where the dimensionless parameter  $\lambda$  is given by

$$\lambda = \frac{LRT_0 m_H}{4F^2 R_s \rho_0 D_H} \quad (6.44)$$

We require right hand sides equations (6.42) and (6.43) to cancel when they are summed for conservation of mass to hold. Otherwise we will not have a balance between the amount of hydrogen reacting and the amount of water vapor being produced. Therefore we have that

$$\frac{m_W}{\delta} = 1 \quad \Rightarrow \quad \delta = 9 \quad (6.45)$$

since the molar mass of water is 9 times that of hydrogen. Once again this is a requirement of the model equations and may not be indicative of empirical information due to the assumption that the mass of oxygen within the cathode is zero. The temperature flux on the surface of the plate becomes

$$\frac{\partial T}{\partial y} = \gamma \frac{q_e(x)}{Re^{\frac{1}{2}}} \quad (6.46)$$

where the parameter  $\gamma$  is given by

$$\gamma = \frac{QRL}{4kF^2R_s} \quad (6.47)$$

Finally, the boundary condition for pressure on the surface of the plate does not alter from that given in (6.21)

## 6.5 Outer region as $Re \rightarrow \infty$

Once again we seek a solution within the inviscid region of the flow where there is no homogeneous reaction or feedback from the heterogeneous reaction present. Therefore, within this region we are able to drop the mass flux boundary conditions (6.42) and (6.43), the temperature flux condition (6.46) and the no-slip condition (6.41). As a result we are able to obtain an exact solution within this region, given by

$$u = 1, \quad v = 0, \quad Y_H = \tilde{Y}_H, \quad Y_W = \tilde{Y}_W, \quad T = 1, \quad P = \tilde{P}, \quad \rho = 1, \quad \mu = 1 \quad (6.48)$$

The outer solution represents a uniform flow of reactants without the presence of a reaction. This exactly conforms with the fact that the outer solution is outside of the boundary-layer region and is not affected by the heterogeneous reaction.

## 6.6 Inner region as $Re \rightarrow \infty$

Within the inner region we are unable to drop the mass flux, temperature flux and no slip conditions as we did in the outer region. This is due to the exothermic heterogeneous reaction and the dominance of viscosity within this region of the flow. Therefore, we are required to find a solution to (6.26)-(6.37) subject to the boundary conditions (6.38)-(6.46).

To find a solution to the above problem we introduce the transformation

$$\psi = \xi^{\frac{1}{2}} f(\eta), \quad \text{with} \quad \eta = \frac{y}{x^{\frac{1}{2}}} \quad \text{and} \quad \xi = x \quad (6.49)$$

We now consider an alternative coordinate system  $(\xi, \eta)$  where  $\eta$  is defined as a similarity variable. The definition of the stream function for the case of compressible flow over a flat, semi-infinite, impermeable plate is not the same as for the incompressible case demonstrated in sections 3.7 and 5.6. In defining this new stream function we take our inspiration from Moore (1951) and Cohen & Reshotko (1955) and thus we define this function as

$$u = \frac{1}{\rho} \frac{\partial \psi}{\partial y} \quad \text{and} \quad v = -\frac{1}{\rho} \frac{\partial \psi}{\partial x} \quad (6.50)$$

The stream function is designed to satisfy the volumetric continuity equation (6.26) exactly which means we no longer need to consider this equation as part of our system. Using the stream function (6.49) and the definition (6.50) we can define the velocity components  $u$  and  $v$  in terms of the function  $f$  via

$$u = \frac{f'(\eta)}{\rho} \quad \text{and} \quad v = \frac{1}{\rho \xi^{\frac{1}{2}}} \left( \frac{\eta}{2} f'(\eta) - \frac{1}{2} f(\eta) \right) \quad (6.51)$$

where the primes denote differentiation with respect to  $\eta$ . Furthermore, we obtain the definitions of the derivatives of the velocity functions, given by

$$\frac{\partial u}{\partial y} = \frac{\partial \eta}{\partial y} \frac{\partial u}{\partial \eta} = \xi^{-\frac{1}{2}} \left[ \frac{f''(\eta)}{\rho} + f'(\eta) \frac{\partial}{\partial \eta} \left( \frac{1}{\rho} \right) \right], \quad (6.52)$$

$$\frac{\partial^2 u}{\partial y^2} = \frac{1}{\xi} \left[ \frac{f'''(\eta)}{\rho} + 2f''(\eta) \frac{\partial}{\partial \eta} \left( \frac{1}{\rho} \right) + f'(\eta) \frac{\partial^2}{\partial \eta^2} \left( \frac{1}{\rho} \right) \right] \quad (6.53)$$

and

$$\frac{\partial u}{\partial x} = \frac{\partial \xi}{\partial x} \frac{\partial u}{\partial \xi} + \frac{\partial \eta}{\partial x} \frac{\partial u}{\partial \eta} = \frac{\partial u}{\partial \xi} - \frac{\eta}{2x} \frac{\partial u}{\partial \eta} \quad (6.54)$$

Upon substitution of (6.51) and(6.52) into (6.54) we obtain

$$\frac{\partial u}{\partial x} = f'(\eta) \frac{\partial}{\partial \xi} \left( \frac{1}{\rho} \right) - \frac{\eta}{2\xi} \left[ \frac{f''(\eta)}{\rho} + f'(\eta) \frac{\partial}{\partial \eta} \left( \frac{1}{\rho} \right) \right] \quad (6.55)$$

If we now substitute these transformations into the momentum equation (6.27) we obtain a new momentum equation in terms of the function  $f$

$$\frac{\mu}{\rho} f''' + f'' \left[ 2\mu \frac{\partial}{\partial \eta} \left( \frac{1}{\rho} \right) + \frac{1}{2\rho} f \right] + f' \left[ \mu \frac{\partial^2}{\partial \eta^2} \left( \frac{1}{\rho} \right) + \frac{1}{2} f \frac{\partial}{\partial \eta} \left( \frac{1}{\rho} \right) + \xi f' \frac{\partial}{\partial \xi} \left( \frac{1}{\rho} \right) \right] - \xi \frac{dP}{d\xi} = 0 \quad (6.56)$$

Here we must take note of (3.46) and in particular that every derivative with respect to  $x$  now takes the form of derivatives with respect to both  $\xi$  and  $\eta$ . However, in the case of the transformed momentum equation (6.56) we can automatically set the term involving  $\frac{\partial P}{\partial \eta}$  to zero since

$$0 = \frac{dP}{dy} = \frac{dP}{d\eta} \frac{\partial \eta}{\partial y} = x^{-\frac{1}{2}} \frac{dP}{d\eta} \quad (6.57)$$

The boundary conditions for the momentum equation under this transformation become

$$f'(\infty) = \rho(\infty), \quad f(0) = f'(0) = 0 \quad (6.58)$$

From boundary condition (6.40) we can see that  $\rho(\infty) = 1$  and so we have the identical boundary conditions to that of the standard Blasius solution. In the case of compressible flow we can see that the momentum equation is not decoupled from the mass fraction of species or the temperature due to the definitions of the mixture viscosity and density.

Therefore, it is no longer an option to solve the momentum equation independently of the convection-diffusion and the energy equations.

We now proceed in finding a full set of transformed equations and boundary conditions for the mass fraction and temperature within the flow. If we apply the transformation (6.49) to the convection-diffusion equation (6.28) we obtain

$$\frac{1}{S_c} \frac{\partial}{\partial \eta} \left( \rho \frac{\partial Y_H}{\partial \eta} \right) = \xi f' \frac{\partial Y_H}{\partial \xi} - \frac{f}{2} \frac{\partial Y_H}{\partial \eta} \quad (6.59)$$

It should be noted that from here on in we will only consider the solution of the mass fraction of hydrogen  $Y_H$ . This is due to the conservation of mass equation which is given by

$$\sum_{i=1}^N Y_i = 1 \quad (6.60)$$

where  $N$  here is the number of species present on the fuel side, in this case two. Thus we have the equation

$$Y_W = 1 - Y_H \quad (6.61)$$

Applying the transformation to the energy equation (6.30) gives

$$\xi f' \frac{\partial T}{\partial \xi} - \frac{f}{2} \frac{\partial T}{\partial \eta} = \frac{\xi E}{\rho} f' \frac{dP}{d\xi} + \frac{1}{Pr} \frac{\partial^2 T}{\partial \eta^2} + E \mu \left[ \frac{f''}{\rho} + f' \frac{\partial}{\partial \eta} \left( \frac{1}{\rho} \right) \right]^2 \quad (6.62)$$

The equation of state (6.33), mixture viscosity (6.35) and mixture density (6.37) will remain the same as previously defined since neither of these equation contains a derivative term.

We are now required to state the remaining transformed boundary conditions for this model. The mass-flux boundary condition for hydrogen at the plate is given

$$\frac{\partial Y_H}{\partial \eta} = \xi^{\frac{1}{2}} \frac{\lambda}{Re^{\frac{1}{4}}} \frac{q_e(\xi)}{\rho_f}, \quad (6.63)$$

and the condition for temperature at the surface of the plate is

$$\frac{\partial T}{\partial \eta} = -\xi^{\frac{1}{2}} \gamma \frac{q_e(x)}{Re^{\frac{1}{2}}} \quad (6.64)$$

The remaining boundary conditions now take the form

$$Y_H = \tilde{Y}_H, \quad Y_W = \tilde{Y}_W, \quad u = 1, \quad v = 0, \quad T = 1, \quad P = \tilde{P}, \quad \rho = 1 \quad \text{on} \quad \xi = 0, \quad \eta > 0 \quad (6.65)$$

$$Y_H \rightarrow \tilde{Y}_H, \quad Y_W \rightarrow \tilde{Y}_W, \quad u \rightarrow 1, \quad v \rightarrow 0, \quad T \rightarrow 1, \quad P \rightarrow \tilde{P}, \quad \rho \rightarrow 1 \quad \text{as} \quad \eta \rightarrow \infty, \quad \xi > 0 \quad (6.66)$$

$$u = 0, \quad v = 0 \quad \text{on} \quad \eta = 0, \quad \xi > 0 \quad (6.67)$$

### 6.6.1 Asymptotic solution for $\xi \ll 1$

We now seek an asymptotic solution to equations (6.56), (6.59) and (6.62) with respect to the boundary conditions (6.58), (6.63)-(6.67) around a point of singularity situated at  $\xi = 0$ . We begin by introducing the expansions for the mass fraction of hydrogen and temperature, which we obtain from examination of the boundary conditions (6.63) and (6.64). On noting from (6.23) that  $q_e(\xi) \sim \mathcal{O}(1)$  as  $\xi \rightarrow 0$  We obtain the expansions

$$Y_H(\xi, \eta) = a_0 + \xi^{\frac{1}{2}} a_1(\eta) + \xi a_2(\eta) + \xi^{\frac{3}{2}} a_3(\eta) + \dots, \quad (6.68)$$

$$T(\xi, \eta) = b_0 + \xi^{\frac{1}{2}} b_1(\eta) + \xi b_2(\eta) + \xi^{\frac{3}{2}} b_3(\eta) + \dots, \quad (6.69)$$

where the functions  $a_i$  and  $b_i$  are  $\mathcal{O}(1)$  as  $\xi \rightarrow 0$  and  $a_0 = \tilde{Y}_H$  and  $b_0 = 1$ . Upon implementing expansions (6.68) and (6.69) we found that the appropriate expansions for the remaining variables are

$$P(\xi, \eta) = p_0 + \xi^{\frac{1}{2}} p_1(\eta) + \xi p_2(\eta) + \dots, \quad (6.70)$$

$$\rho(\xi, \eta) = r_0 + \xi^{\frac{1}{2}} r_1(\eta) + \xi r_2(\eta) + \dots, \quad (6.71)$$

$$\mu(\xi, \eta) = s_0 + \xi^{\frac{1}{2}} s_1(\eta) + \xi s_2(\eta) + \dots, \quad (6.72)$$

Once again the functions  $p_i$ ,  $r_i$  and  $s_i$  are  $\mathcal{O}(1)$  as  $\xi \rightarrow 0$  and  $p_0 = \tilde{P}$ ,  $r_0 = 1$  and  $s_0 = 1$ .

Substituting the expansions (6.68)-(6.72) into the momentum equation (6.56) yields the following set of equations in ascending orders of  $\xi$ , for  $\mathcal{O}(\xi^{\frac{1}{2}})$ ,  $\mathcal{O}(\xi)$  and  $\mathcal{O}(\xi^{\frac{3}{2}})$

$$0 = f''' s_0 + \frac{f'' f}{2}, \quad (6.73)$$

$$\begin{aligned} 0 &= f''' \frac{\rho_0}{\rho_H \rho_W} [s_1(a_0 \rho_W + (1 - a_0) \rho_H) + s_0(a_1 \rho_W - a_1 \rho_H)] + \\ &\quad f'' \frac{\rho_0}{\rho_H \rho_W} \left[ 2s_0(a'_1 \rho_W - a'_1 \rho_H) + \frac{f}{2}(a_1 \rho_W - a_1 \rho_H) \right] + \\ &\quad f' \frac{\rho_0}{\rho_H \rho_W} \left[ s_0(a''_1 \rho_W - a''_1 \rho_H) + \frac{f}{2}(a'_1 \rho_W - a'_1 \rho_H) + \frac{f'}{2}(a_1 \rho_W - a_1 \rho_H) \right] - \frac{p_1}{2}, \end{aligned} \quad (6.74)$$

$$\begin{aligned} 0 &= f''' \frac{\rho_0}{\rho_H \rho_W} [s_2(a_0 \rho_W + (1 - a_0) \rho_H) + s_1(a_1 \rho_W - a_1 \rho_H) + s_0(a_2 \rho_W - a_2 \rho_H)] + \\ &\quad f'' \frac{\rho_0}{\rho_H \rho_W} \left[ 2(s_0(a'_2 \rho_W - a'_2 \rho_H) + s_1(a'_1 \rho_W - a'_1 \rho_H)) + \frac{f}{2}(a_2 \rho_W - a_2 \rho_H) \right] + \\ &\quad f' \frac{\rho_0}{\rho_H \rho_W} \left[ s_1(a''_1 \rho_W - a''_1 \rho_H) + s_0(a''_2 \rho_W - a''_2 \rho_H) + \frac{f}{2}(a'_2 \rho_W - a'_2 \rho_H) + f'(a_2 \rho_W - a_2 \rho_H) \right] - p_2 \end{aligned} \quad (6.75)$$

The values of the functions  $s_i$  are given by

$$\begin{aligned}
s_0 = & \frac{m_w \mu_H}{\mu_{f,0} \phi_{HW}} a_0 \left[ 1 + a_0 - \frac{a_0 m_W}{\phi_{HW}} + \left( \frac{a_0 m_W}{\phi_{HW}} - a_0 \right)^2 - \left( \frac{a_0 m_W}{\phi_{HW}} - a_0 \right)^3 \right] + \\
& \frac{\mu_W (1 - a_0)}{\mu_{f,0}} \left[ 1 - m_W \phi_{WH} a_0 + a_0 + (m_W \phi_{WH} a_0 - a_0)^2 - (m_W \phi_{WH} a_0 - a_0)^3 \right], \\
\end{aligned} \tag{6.76}$$

We already know that the value of  $s_0 = 1$  but we include details of the expansion of this constant for completeness. The expansion of  $s_1$  is represented by

$$\begin{aligned}
s_1 = & \frac{m_w \mu_H}{\mu_{f,0} \phi_{HW}} \left[ a_1 \left\{ 1 + a_0 - \frac{a_0 m_W}{\phi_{HW}} + \left( \frac{a_0 m_W}{\phi_{HW}} - a_0 \right)^2 - \left( \frac{a_0 m_W}{\phi_{HW}} - a_0 \right)^3 \right\} + \right. \\
& a_0 \left\{ a_1 - \frac{m_W a_1}{\phi_{HW}} + 2 \left( \frac{m_W a_0}{\phi_{HW}} - a_0 \right) \left( \frac{m_W a_1}{\phi_{HW}} - a_1 \right) - 3 \left( \frac{a_0 m_W}{\phi_{HW}} - a_0 \right)^2 \left( \frac{a_1 m_W}{\phi_{HW}} - a_1 \right) \right\} \Big] + \\
& \frac{\mu_W}{\mu_{f,0}} \left[ a_1 \left\{ 1 - m_W \phi_{WH} a_0 + a_0 + (m_W \phi_{WH} a_0 - a_0)^2 - (m_W \phi_{WH} a_0 - a_0)^3 \right\} + \right. \\
& (1 - a_0) \left\{ a_1 - m_W \phi_{WH} a_1 + 2(m_W \phi_{WH} a_0 - a_0)(m_W \phi_{WH} a_1 - a_1) - \right. \\
& \left. \left. 3(m_W \phi_{WH} a_0 - a_0)^2 (m_W \phi_{WH} a_1 - a_1) \right\} \right] \\
\end{aligned} \tag{6.77}$$

and  $s_2$

$$\begin{aligned}
s_2 = & \frac{m_w \mu_H}{\mu_{f,0} \phi_{HW}} \left[ a_2 \left\{ 1 + a_0 - \frac{a_0 m_W}{\phi_{HW}} + \left( \frac{a_0 m_W}{\phi_{HW}} - a_0 \right)^2 - \left( \frac{a_0 m_W}{\phi_{HW}} - a_0 \right)^3 \right\} + \right. \\
& a_1 \left\{ a_1 - \frac{m_W a_1}{\phi_{HW}} + 2 \left( \frac{m_W a_0}{\phi_{HW}} - a_0 \right) \left( \frac{m_W a_1}{\phi_{HW}} - a_1 \right) - 3 \left( \frac{a_0 m_W}{\phi_{HW}} - a_0 \right)^2 \left( \frac{a_1 m_W}{\phi_{HW}} - a_1 \right) \right\} + \\
& a_0 \left\{ a_2 - \frac{m_W a_2}{\phi_{HW}} + \left( \frac{a_1 m_W}{\phi_{HW}} - a_1 \right)^2 + 2 \left( \frac{m_W a_0}{\phi_{HW}} - a_0 \right) \left( \frac{m_W a_2}{\phi_{HW}} - a_2 \right) + \right. \\
& \left. 3 \left( \frac{m_W a_0}{\phi_{HW}} - a_0 \right) \left( \frac{m_W a_1}{\phi_{HW}} - a_1 \right)^2 + 3 \left( \frac{m_W a_0}{\phi_{HW}} - a_0 \right)^2 \left( \frac{m_W a_2}{\phi_{HW}} - a_2 \right) \right\} \Big] + \\
& \frac{\mu_W}{\mu_{f,0}} \left[ a_2 \left\{ 1 - m_W \phi_{WH} a_0 + a_0 + \left( m_W \phi_{WH} a_0 - a_0 \right)^2 - \left( m_W \phi_{WH} a_0 - a_0 \right)^3 \right\} + \right. \\
& a_1 \left\{ a_1 - m_W \phi_{WH} a_1 + 2 \left( m_W \phi_{WH} a_0 - a_0 \right) \left( m_W \phi_{WH} a_1 - a_1 \right) - \right. \\
& \left. \left. 3 \left( m_W \phi_{WH} a_0 - a_0 \right)^2 \left( m_W \phi_{WH} a_1 - a_1 \right) \right\} + \right. \\
& \left. (1 - a_0) \left\{ a_2 - m_W \phi_{WH} a_2 + \left( m_W \phi_{WH} a_1 - a_1 \right)^2 + 2 \left( m_W \phi_{WH} a_0 - a_0 \right) \left( m_W \phi_{WH} a_1 - a_1 \right) + \right. \right. \\
& \left. \left. 3 \left( m_W \phi_{WH} a_0 - a_0 \right) \left( m_W \phi_{WH} a_1 - a_1 \right)^2 + 3 \left( m_W \phi_{WH} a_0 - a_0 \right)^2 \left( m_W \phi_{WH} a_2 - a_2 \right) \right\} \right] \tag{6.78}
\end{aligned}$$

Since the values of  $s_i$  are calculated from equation (6.35) we have used the binomial expansion in order to obtain (6.76)-(6.78). In making this expansion we have taken terms up to the cubic order since after this point the complexity increases exponentially and does not offer a greater amount of accuracy to warrant doing. If we now substitute the expansions into the convection-diffusion equation (6.59) we obtain, in ascending orders of  $\xi$

$$\frac{r_0 a_1''}{S_c} = \frac{f' a_1}{2} - \frac{f a_1'}{2}, \quad (6.79)$$

$$\frac{(r_0 a_2'' + r_1' a_1' + r_1 a_1'')}{S_c} = f' a_2 - \frac{f a_2'}{2}, \quad (6.80)$$

$$\frac{(r_0 a_3'' + r_1' a_2' + r_1 a_2'' + r_2' a_1' + r_2 a_1'')}{S_c} = \frac{3 f' a_3}{2} - \frac{f a_3'}{2} \quad (6.81)$$

where the expansions of the values of  $r_i$  are given by

$$r_0 = \frac{\rho_W}{\rho_0} \left[ 1 - \left( \frac{\rho_W}{\rho_H} a_0 - a_0 \right) + \left( \frac{\rho_W}{\rho_H} a_0 - a_0 \right)^2 - \left( \frac{\rho_W}{\rho_H} a_0 - a_0 \right)^3 \right], \quad (6.82)$$

$$r_1 = \frac{\rho_W}{\rho_0} \left[ 2 \left( \frac{\rho_W}{\rho_H} a_0 - a_0 \right) \left( \frac{\rho_W}{\rho_H} a_1 - a_1 \right) - \left( \frac{\rho_W}{\rho_H} a_1 - a_1 \right) - 3 \left( \frac{\rho_W}{\rho_H} a_0 - a_0 \right)^2 \left( \frac{\rho_W}{\rho_H} a_1 - a_1 \right) \right] \quad (6.83)$$

$$r_2 = \frac{\rho_W}{\rho_0} \left[ \left( \frac{\rho_W}{\rho_H} a_1 - a_1 \right)^2 + 2 \left( \frac{\rho_W}{\rho_H} a_0 - a_0 \right) \left( \frac{\rho_W}{\rho_H} a_2 - a_2 \right) - 3 \left( \frac{\rho_W}{\rho_H} a_0 - a_0 \right)^2 \left( \frac{\rho_W}{\rho_H} a_2 - a_2 \right) - \left( \frac{\rho_W}{\rho_H} a_2 - a_2 \right) - 3 \left( \frac{\rho_W}{\rho_H} a_0 - a_0 \right) \left( \frac{\rho_W}{\rho_H} a_1 - a_1 \right)^2 \right] \quad (6.84)$$

where upon substitution of parameter values we do obtain  $r_0 = 1$ . If we apply the expansions to the mass-flux boundary condition (6.63) then we obtain, in ascending orders of  $\xi$

$$a'_1 = \frac{\lambda\rho_0}{Re^{\frac{1}{2}}\rho_H\rho_W} q_0(a_0\rho_W + (1-a_0)\rho_H), \quad (6.85)$$

$$a'_2 = \frac{\lambda\rho_0}{Re^{\frac{1}{2}}\rho_H\rho_W} [q_0(a_1\rho_W - a_1\rho_H) + q_1(a_0\rho_W + (1-a_0)\rho_H)], \quad (6.86)$$

$$a'_3 = \frac{\lambda\rho_0}{Re^{\frac{1}{2}}\rho_H\rho_W} [q_0(a_2\rho_W - a_2\rho_H) + q_1(a_1\rho_W - a_1\rho_H) + q_2(a_0\rho_W + (1-a_0)\rho_H)] \quad (6.87)$$

where the values of  $q_i$  are calculated from applying the asymptotic expansions to the ion flux density equation (6.23). Thus we obtain

$$q_0 = b_0 \left[ \ln(a_0) + a_0 + \frac{a_0^2}{2} + \frac{\Gamma}{b_0} + \ln(Y_O^{\frac{1}{2}}) + \sigma \right], \quad (6.88)$$

$$q_1 = b_0 \left[ \frac{a_1}{a_0} + a_1 + a_0a_1 - \frac{\Gamma b_1}{b_0^2} \right] + b_1 \left[ \ln(a_0) + a_0 + \frac{a_0^2}{2} + \frac{\Gamma}{b_0} + \ln(Y_O^{\frac{1}{2}}) + \sigma \right], \quad (6.89)$$

$$\begin{aligned} q_2 = & b_0 \left[ \frac{a_2}{a_0} - \frac{a_1^2}{2a_0^2} + a_2 + \frac{a_1^2}{2} + a_0a_2 + \frac{\Gamma}{b_0} \left( \frac{b_1^2}{b_0^2} - \frac{b_2}{b_0} \right) \right] + b_1 \left[ \frac{a_1}{a_0} + a_1 + a_0a_1 - \frac{\Gamma b_1}{b_0^2} \right] + \\ & b_2 \left[ \ln(a_0) + a_0 + \frac{a_0^2}{2} + \frac{\Gamma}{b_0} + \ln(Y_O^{\frac{1}{2}}) + \sigma \right] \end{aligned} \quad (6.90)$$

Applying the asymptotic expansions to the energy equation (6.62) yields the following set of equations in ascending orders of  $\xi$

$$Es_0g_0 = 0, \quad (6.91)$$

$$\frac{f'b_1}{2} - \frac{fb'_1}{2} = \frac{E\rho_0f'}{\rho_H\rho_W} \left( \frac{p_1}{2}(a_0\rho_W + (1-a_0)\rho_H) \right) + \frac{b''_1}{Pr} + E(s_0g_1 + s_1g_0), \quad (6.92)$$

$$f'b_2 - \frac{fb'_2}{2} = \frac{E\rho_0f'}{\rho_H\rho_W} \left( p_2(a_0\rho_w + (1-a_0)\rho_H) + \frac{p_1}{2}(a_1\rho_W - a_1\rho_H) \right) + \frac{b''_2}{Pr} + E_f(s_0g_2 + s_1g_1 + s_2g_0), \quad (6.93)$$

$$\frac{3f'b_3}{2} - \frac{fb'_3}{2} = \frac{E\rho_0f'}{\rho_H\rho_W} \left( p_2(a_1\rho_w - a_1\rho_H) + \frac{p_1}{2}(a_2\rho_W - a_2\rho_H) \right) + \frac{b''_3}{Pr} + E_f(s_0g_3 + s_1g_2 + s_2g_1) \quad (6.94)$$

The equation evaluated at the constant order of magnitude (6.91) is satisfied due to the value of the parameter  $E$  being effectively zero. The values of  $g_i$  are defined by

$$g_0 = \left( \frac{\rho_0 f''}{\rho_H \rho_W} \right)^2 (a_0 \rho_W + (1 - a_0) \rho_H)^2, \quad (6.95)$$

$$\begin{aligned} g_1 = & 2 \left( \frac{\rho_0 f''}{\rho_H \rho_W} \right)^2 (a_0 \rho_W + (1 - a_0) \rho_H)(a_1 \rho_W - a_1 \rho_H) + \\ & 2 \left( \frac{\rho_0 f''}{\rho_H \rho_W} \right) \left( \frac{\rho_0 f'}{\rho_H \rho_W} \right) (a_0 \rho_W + (1 - a_0) \rho_H)(a'_1 \rho_W - a'_1 \rho_H), \end{aligned} \quad (6.96)$$

$$\begin{aligned} g_2 = & \left( \frac{\rho_0 f''}{\rho_H \rho_W} \right)^2 [2(a_0 \rho_W + (1 - a_0) \rho_H)(a_2 \rho_W - a_2 \rho_H) + (a_1 \rho_W - a_1 \rho_H)^2] + \\ & \left( \frac{\rho_0 f'}{\rho_H \rho_W} \right)^2 (a'_1 \rho_W - a'_1 \rho_H)^2 + \\ & 2 \left( \frac{\rho_0 f''}{\rho_H \rho_W} \right) \left( \frac{\rho_0 f'}{\rho_H \rho_W} \right) [(a_0 \rho_W + (1 - a_0) \rho_H)(a'_2 \rho_W - a'_2 \rho_H) + (a_1 \rho_W - a_1 \rho_H)(a'_1 \rho_W - a'_1 \rho_H)], \end{aligned} \quad (6.97)$$

$$\begin{aligned} g_3 = & 2 \left( \frac{\rho_0 f''}{\rho_H \rho_W} \right)^2 (a_1 \rho_W - a_1 \rho_H)(a_2 \rho_W - a_2 \rho_H) + 2 \left( \frac{\rho_0 f'}{\rho_H \rho_W} \right)^2 (a'_1 \rho_W - a'_1 \rho_H)(a'_2 \rho_W - a'_2 \rho_H) + \\ & 2 \left( \frac{\rho_0 f''}{\rho_H \rho_W} \right) \left( \frac{\rho_0 f'}{\rho_H \rho_W} \right) [(a_1 \rho_W - a_1 \rho_H)(a'_2 \rho_W - a'_2 \rho_H) + (a_2 \rho_W - a_2 \rho_H)(a'_1 \rho_W - a'_1 \rho_H)] \end{aligned} \quad (6.98)$$

The corresponding surface boundary conditions to the expanded energy equation are given by

$$b'_1 = - \frac{\gamma}{Re^{\frac{1}{2}}} q_0, \quad (6.99)$$

$$b'_2 = - \frac{\gamma}{Re^{\frac{1}{2}}} q_1, \quad (6.100)$$

$$b'_3 = - \frac{\gamma}{Re^{\frac{1}{2}}} q_2, \quad (6.101)$$

Now in order to calculate the pressure within the flow we are required to substitute the asymptotic expansions for pressure, temperature, density and hydrogen mass fraction

into the equation of state (6.33). This yields the following set of equations

$$p_0 = \beta r_0 b_0 \left( a_0 + \frac{(1 - a_0)}{m_W} \right), \quad (6.102)$$

$$p_1 = \beta \left[ r_0 b_0 \left( a_1 - \frac{a_1}{m_W} \right) + (r_0 b_1 + r_1 b_0) \left( a_0 + \frac{(1 - a_0)}{m_W} \right) \right], \quad (6.103)$$

$$p_2 = \beta \left[ r_0 b_0 \left( a_2 - \frac{a_2}{m_W} \right) + (r_0 b_1 + r_1 b_0) \left( a_1 - \frac{a_1}{m_W} \right) + (r_0 b_2 + r_1 b_1 + r_2 b_0) \left( a_0 + \frac{(1 - a_0)}{m_W} \right) \right], \quad (6.104)$$

where  $p_0 = \tilde{P}$  upon substitution of the parameter values into (6.102).

It now only remains for us to identify the function values within the far field when we substitute the asymptotic expansions into (6.40). Therefore, we obtain

$$a_1(\infty) = 0, \quad a_2(\infty) = 0, \quad a_3(\infty) = 0, \quad (6.105)$$

$$b_1(\infty) = 0, \quad b_2(\infty) = 0, \quad b_3(\infty) = 0, \quad (6.106)$$

It should be noted here that (6.73)-(6.106) represent a set of boundary value problems for the different orders of momentum, mass fraction, temperature, density, pressure and viscosity in (6.68)-(6.72). Due to the assumption that the mixture is compressible, the above system of equations is now coupled which means that we can only obtain a solution by solving all of the equation together. To find a solution to this system of boundary value problems we use the shooting method where the parameter values are given in Tables 6.1 and 6.2.

Parameter	Symbol	Value	Units
Molar mass of chemical species	$m_i$	$m_H=0.002$ $m_W=0.018$ $m_O=0.032$	$kg\ mol^{-1}$ $kg\ mol^{-1}$ $kg\ mol^{-1}$
Inlet mass fractions of species	$\tilde{Y}_i$	$\tilde{Y}_H = 0.97$ $\tilde{Y}_W = 0.03$	
Hydrogen diffusivity	$D_H$	$10^{-4}$	$m^2\ s^{-1}$
Faraday's constant	$F$	96485	$C\ mol^{-1}$
Gas constant	$R$	8.3144	$J\ K^{-1}\ mol^{-1}$
Inlet temperature	$T_0$	1000	$K$
Cathode temperature	$T_a$	1000	$K$
Species density	$\rho_i$	$\rho_H=0.0481$ $\rho_W=0.25$	$kg\ m^{-3}$ $kg\ m^{-3}$
Cathode density	$\rho_a$	0.34	$kg\ m^{-3}$
Inlet Pressure	$P_0$	1	$atm$
Anode length	$L$	$O(10^{-1})$	$m$
Specific resistance of zirconia	$R_s$	$1.707 \times 10^{-4}$	$\Omega\ m^2$
Species viscosity	$\mu_i$	$\mu_H = 1.958 \times 10^{-5}$ $\mu_W = 3.789 \times 10^{-5}$	$kg\ m^{-1}\ s^{-1}$ $kg\ m^{-1}\ s^{-1}$
Inlet velocity	$U_0$	$O(10^{-1})$	$m\ s^{-1}$
Ideal potential	$U^r$	0.9	$V$
Cell potential	$U_{cell}$	0.4-1.23	$V$
Heat capacity	$C_p$	14599.24	$J\ kg^{-1}\ K^{-1}$
Thermal conductivity	$k$	0.16296	$W\ m^{-1}\ K^{-1}$
Heat released from reaction (6.1)	$Q$	143	$J\ mol^{-1}$

Table 6.1: Parameters, their symbols, values and units

Symbol	Typical value	Description
$Re$	25	Reynolds Number = $\frac{\text{inertial forces}}{\text{viscous forces}}$
$S_c$	4.0248	Schmidt number = $\frac{\text{viscous forces}}{\text{diffusive forces}}$
$Pr$	1.78	Prandtl number = $\frac{\text{viscous diffusion}}{\text{thermal diffusion}}$
$\alpha$	$2.2665 \times 10^{-4}$	Thermal diffusivity
$E$	$6.8497 \times 10^{-10}$	Eckert number = $\frac{\text{kinetic energy}}{\text{enthalpy}}$
$\sigma$	7.8917	
$\Gamma$	11.6045 - (-7.6590)	
$\beta$	$4.157 \times 10^8$	
$\lambda$	0.0531	$\frac{\text{electrochemical flux of hydrogen}}{\text{diffusive flux of hydrogen}}$
$\gamma$	$1.1478 \times 10^{-4}$	

Table 6.2: Definitions of dimensionless parameters and their typical values

## 6.7 Results and discussion

We now seek a numerical solution to equations (6.59) and (6.62) subject to the boundary conditions (6.63)-(6.40). The numerical solution for the velocity within the flow is taken from the shooting method solution that was obtain in the numerical solution of the asymptotic expansion of the model equations and boundary conditions. The numerical method that we used to solve the model equations is the same as in section 3.8.1.

Fig. 6.1 represent a plot of the mass fraction of hydrogen within the coordinate system  $(\xi, \eta)$  for an overall cell potential of  $U_{cell} = 0.5$ . We can see from this figure that the effects of the reaction are confined to a small distance close to the plate and do not affect the far field flow. Moreover, the reaction rate of hydrogen close to the leading edge of the plate can be seen to be much higher than that for greater values of  $\xi$ . The details of the reaction rate are plotted in Fig. 6.2 where we have plotted the gradient of mass fraction of hydrogen along the surface of the plate for  $U_{cell} = 0.5$ . Here we can see in more detail the severity of the reaction rate close to the leading edge and that for  $\xi > 0.4$  we have an almost constant reaction rate. The reason for this is due to the change in the mixture composition around this point where a hydrogen rich stream now becomes a 50:50 hydrogen to water stream.

In Fig. 6.3 we have plotted the mass fraction of water  $Y_W$  within the coordinate system  $(\xi, \eta)$  for  $U_{cell} = 0.5$ . We know that the mass fraction of water produced is equal to that of hydrogen consumed due to the continuity condition (6.61). However, for the readers convenience we have plotted this figure here.

An addition to this model is the introduction of temperature variations and the link between the exothermic reaction and the boundary condition for temperature a long the surface of the plate. In Fig. 6.4 we have plotted the temperature  $T$  within the coordinate system  $(\xi, \eta)$  for  $U_{cell} = 0.5$ . We can see that there is no significant variation

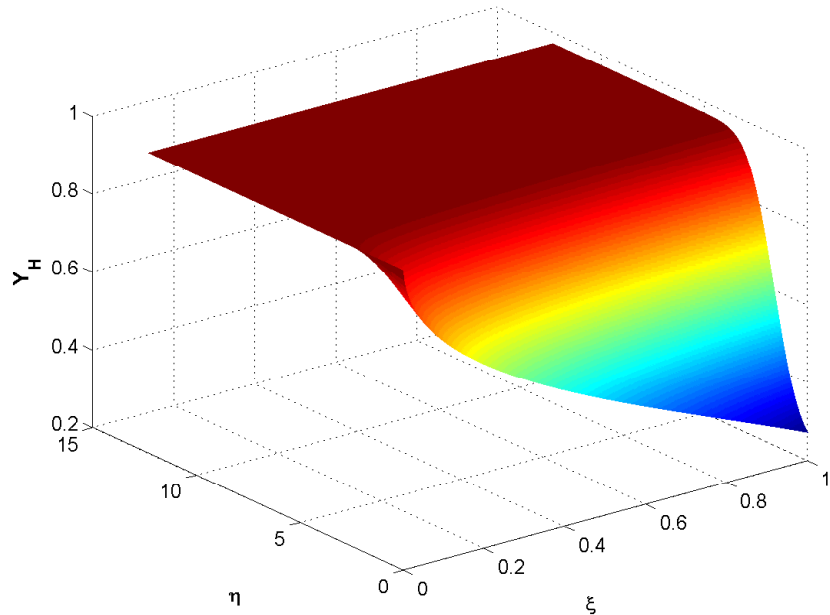


Figure 6.1:  $Y_H$  plotted against the coordinate system  $(\xi, \eta)$  for  $U_{cell} = 0.5$ . This demonstrates how the mass fraction of hydrogen varies throughout the flow domain.

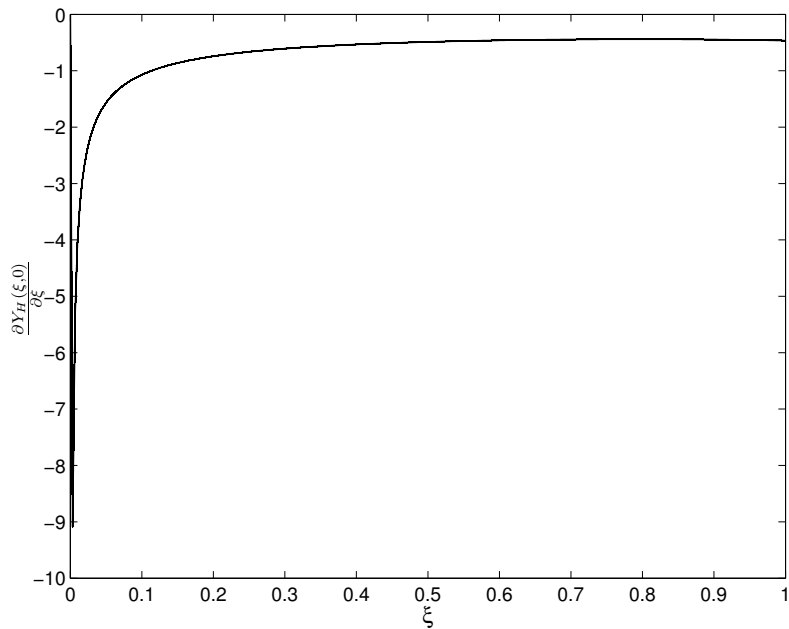


Figure 6.2: Numerical solution of  $\frac{\partial Y_H}{\partial \xi}$  along the surface of the plate for  $U_{cell} = 0.5$ . This demonstrates how the reaction rate of hydrogen along the surface of the plate varies.

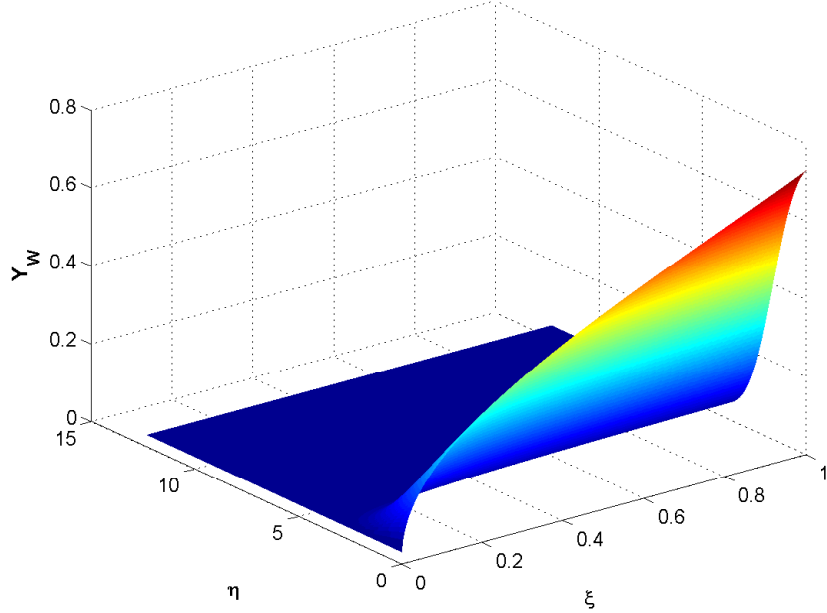


Figure 6.3:  $Y_W$  plotted against the coordinate system  $(\xi, \eta)$  for  $U_{cell} = 0.5$ . This demonstrates how the mass fraction of water varies throughout the flow domain.

in temperature along the plate with the maximum temperature only reaching 0.1% above the initial temperature. More specifically this is only a 1K (or equally  $1^{\circ}\text{C}$ ) increase for an inlet temperature of 1000 K. Therefore, the assumption in chapter 3 that the system is isothermal seems to be valid from analysis of this figure.

One of the most important additions to this model is the assumption that the flow is compressible. In Fig. 6.5 we have plotted the mixture density within the coordinate system  $(\xi, \eta)$ . We can see from this plot that the mixture density increases along the surface of the plate and reaches a maximum value of around 2.4 times the initial density. This is due to the mixture composition changing from hydrogen rich to water rich and that the density of water is over 5 times that of hydrogen.

Fig. 6.6 we have plotted the pressure  $P$  within the coordinate system  $(\xi, \eta)$  for  $U_{cell} = 0.5$ . Here we have scaled the value of  $P$  by the constant value of  $\beta$  found in (6.34). From this plot we can see that there is a pressure drop along the plate from the leading

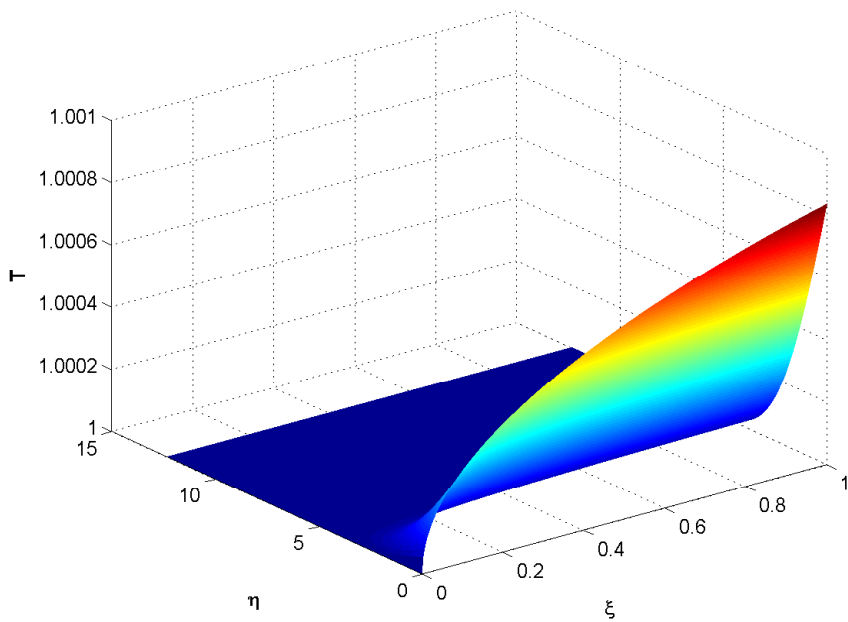


Figure 6.4:  $T$  plotted against the coordinate system  $(\xi, \eta)$  for  $U_{cell} = 0.5$ . This demonstrates how the dimensionless absolute temperature varies throughout the flow domain.

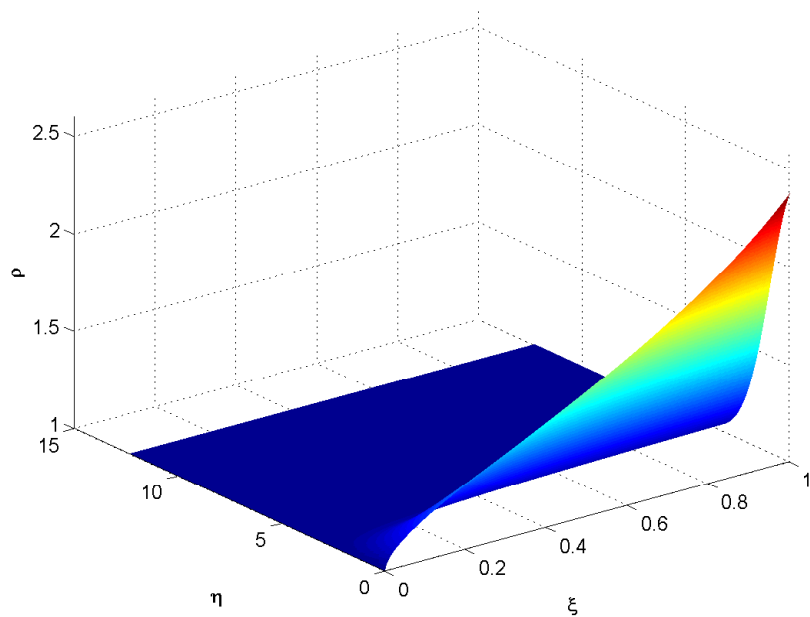


Figure 6.5:  $\rho$  plotted against the coordinate system  $(\xi, \eta)$  for  $U_{cell} = 0.5$ . This demonstrates how the dimensionless species mixture density varies throughout the flow domain.

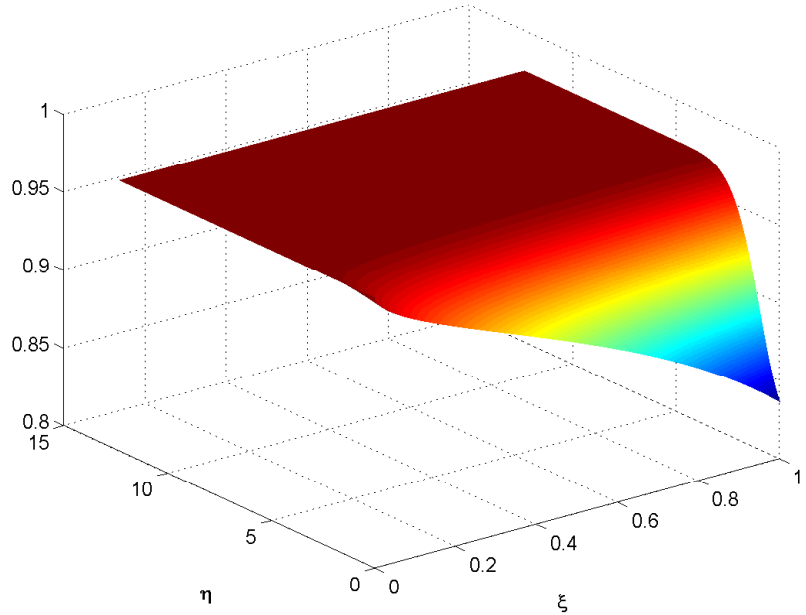


Figure 6.6:  $P$  plotted against the coordinate system  $(\xi, \eta)$  for  $U_{cell} = 0.5$ . This demonstrates how the dimensionless pressure varies throughout the flow domain.

edge. More specifically there the pressure reduces by over 14% from the inlet to the end of the plate. The reason for this occurrence lies with equation (6.33) and the fact that the dimensionless molar mass of water  $m_W = 2$ . This implies that the variation of mass fraction of water is only half as significant as that of hydrogen and as such we get a reduction in pressure due to the reduction in mass fraction of hydrogen.

The above figures all depicted the model properties for a single value of  $U_{cell} = 0.5$ . However, the value of  $U_{cell}$  can vary based on the designated operating conditions of the cell. Therefore, it is essential to understand how these model variables alter under varying values of  $U_{cell}$ .

Fig. 6.7 depicts the mass fraction of hydrogen along the surface of the plate plotted against the coordinate  $\xi$  and the cell voltage  $U_{cell}$ . For large values of  $U_{cell}$  we can see that the reaction rate of hydrogen is effectively switched off which is to be expected as  $U_{cell}$  approaches the OCV. Decreasing the value of  $U_{cell}$  promotes the reaction of hydrogen due

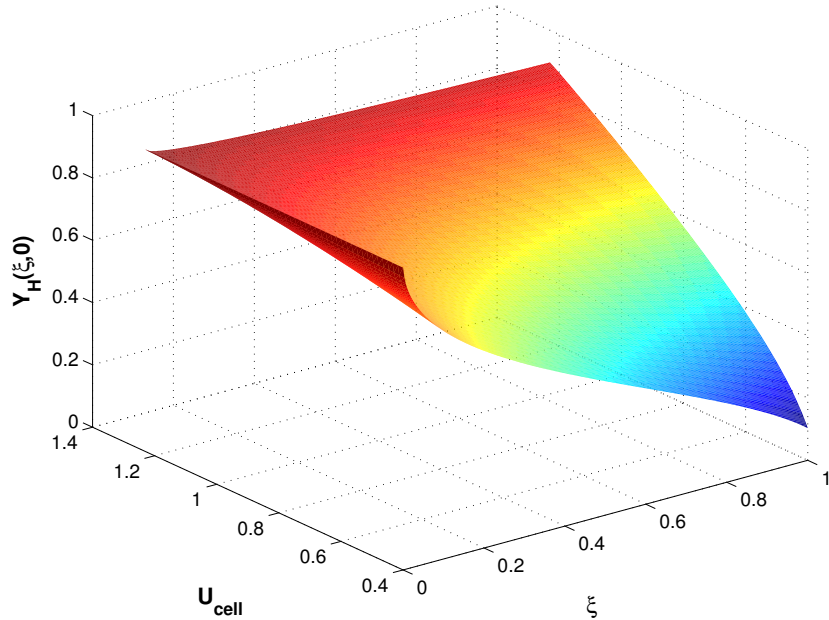


Figure 6.7: Plot of the surface mass fraction of hydrogen,  $Y_H(\xi, 0)$ , against  $\xi$  and varying values of cell voltage  $U_{cell}$ . This demonstrates how the surface mass fraction of hydrogen varies for all considered cell potentials.

to the increase in ion flux density which can be seen by the increase in the value of  $\Gamma$  (6.25). For completeness we have plotted the surface mass fraction of water for varying values of  $U_{cell}$  in Fig. 6.8.

Figs. 6.9-6.11 show the surface temperature, density and pressure plotted against the coordinate  $\xi$  for varying values of the cell voltage  $U_{cell}$ , respectively. For high values of  $U_{cell}$  we can see that for all three of these variables there is no distinguishable change from that of their respective inlet values. However, as we decrease the value of  $U_{cell}$  we can see a distinctive increase in the temperature and density whilst there is a decrease in the pressure. These are all due to the changes in the reaction rate of hydrogen where decreasing  $U_{cell}$  increases this reaction rate which in turn increases the ratio of water to hydrogen. From the temperature flux boundary condition (6.64) and definition of mixture pressure and density (6.33) and (6.37) we can see how a variation in this ratio will change

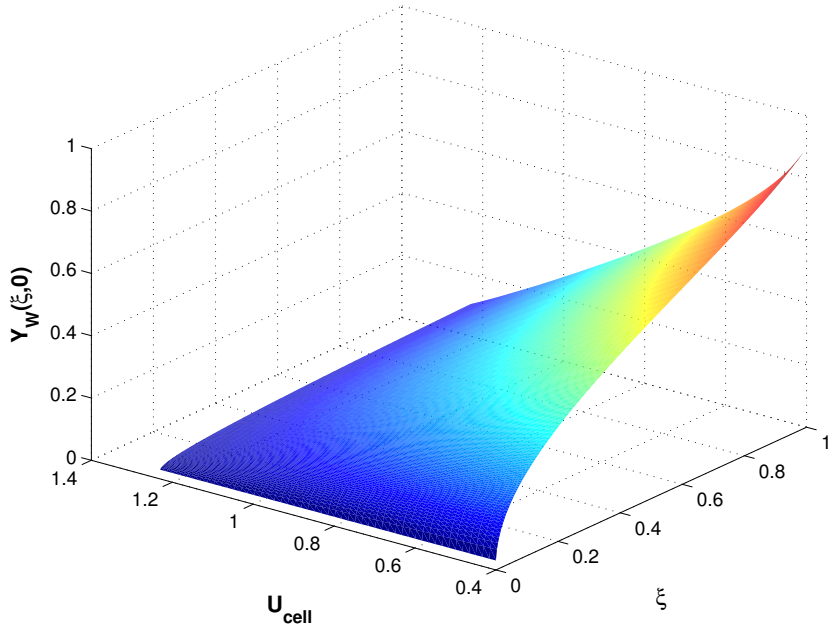


Figure 6.8: Plot of the surface mass fraction of water,  $Y_W(\xi, 0)$ , against  $\xi$  and varying values of cell voltage  $U_{cell}$ . (This follows from Fig 6.7 and from  $Y_H + Y_W = 1$ ).

the properties of each of these variables in this manner.

All of the above figures have used the assumption that the mass fraction of oxygen on the cathode side of the cell is equal to that of the mass fraction which is present in air. However, we are able to analyse the effects on the variables within the anode when this value is allowed to vary.

Fig. 6.12 shows the surface mass fraction of hydrogen plotted against the coordinate  $\xi$  and varying values of the mass fraction of oxygen  $Y_O$  for  $U_{cell} = 0.5$ . We can see from this plot that the mass fraction of hydrogen decreases for higher values of  $Y_O$  which implies that the value of  $Y_O$  has a direct effect on the reaction rate of hydrogen. This is due to increases in  $Y_O$  having the effect of increasing the value of the ion flux density which can be seen in (6.23). Fig. 6.13 represent the surface mass fraction of water plotted against the coordinate  $\xi$  and varying values of  $Y_O$ . The increase in water is once again equal to the consumption of hydrogen along the surface of the plate.

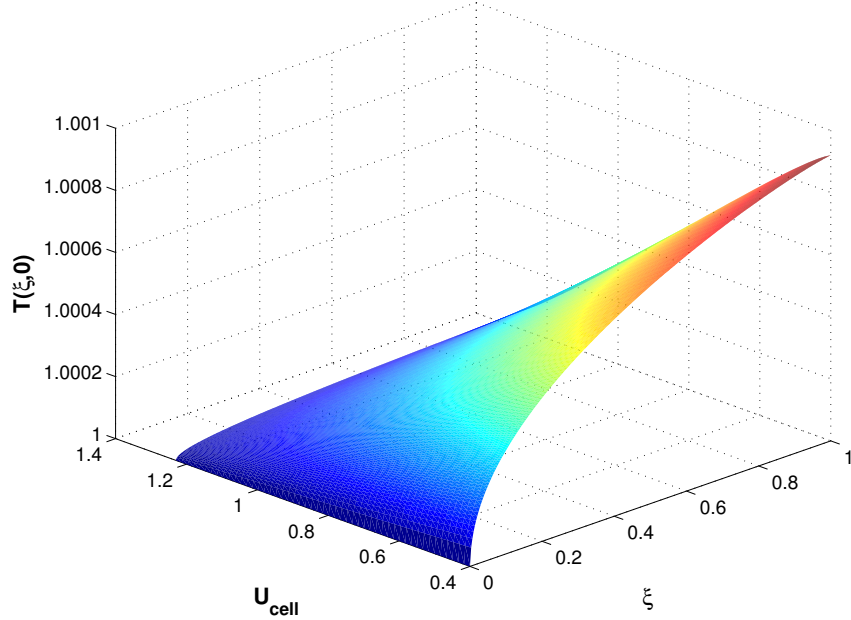


Figure 6.9: Plot of the surface temperature,  $T(\xi, 0)$ , against  $\xi$  and varying values of cell voltage  $U_{cell}$ . This demonstrates how the dimensionless absolute temperature varies along the surface for all considered cell potentials.

With regards to the remaining variables within our model, Figs. 6.14-6.16 represent the plots of surface temperature, density and pressure against the coordinate  $\xi$  and varying values of  $Y_O$  for  $U_{cell} = 0.5$ . We can see from these plots that temperature and density increase whereas pressure decreases with increasing values of  $Y_O$ . Once again this is due to the effects of  $Y_O$  on the value of the ion flux density and the relationship that these variables have with the ion flux density and the values of the mass fractions of hydrogen and water.

### 6.7.1 Comparison to Incompressible Model

Throughout this thesis we have constructed models for the incompressible and compressible flow and reaction of humidified hydrogen across a plate. From these results we can draw comparisons between the models to highlight the differences between the different techniques.

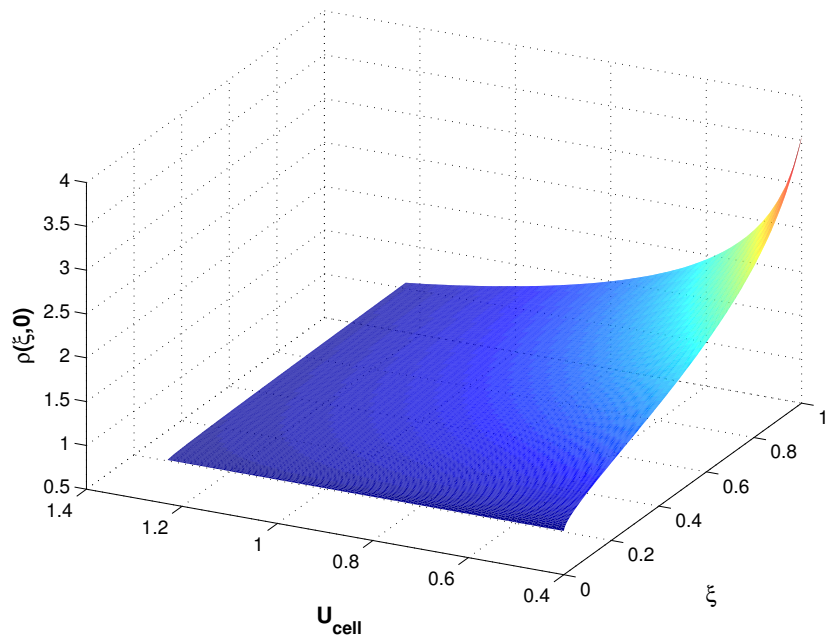


Figure 6.10: Plot of the surface density,  $\rho(\xi, 0)$ , against  $\xi$  and varying values of cell voltage  $U_{cell}$ . This demonstrates how the dimensionless density along the surface varies for all considered cell potentials.

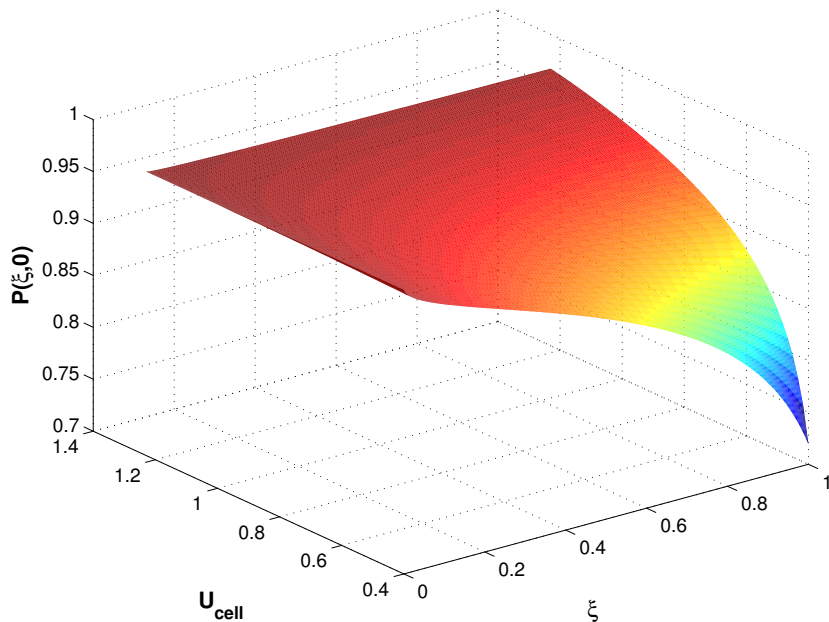


Figure 6.11: Plot of the surface pressure,  $P(\xi, 0)$ , against  $\xi$  and varying values of cell voltage  $U_{cell}$ . This demonstrates how the dimensionless pressure along the surface varies for all considered cell potentials.

Fig. 6.17 represents the comparison of the hydrogen reaction rate for the incompressible and compressible models. From this plot it can be seen that there is a significant variation in reaction rates between the models, with the compressible case demonstrating the faster rate. This difference is due to the compressible model taking into account the fact that water has a greater density compared to hydrogen within this set-up. This assumption has a direct implication on the heterogeneous reaction rates along the surface of the plate. The magnitude of this difference highlights the importance of the compressibility assumption in fuel cell modelling.

## 6.8 Chapter Summary

Within this chapter we examined the same model set up developed in chapter 3 with the addition of the assumption that the flow was now compressible, due to varying mixture

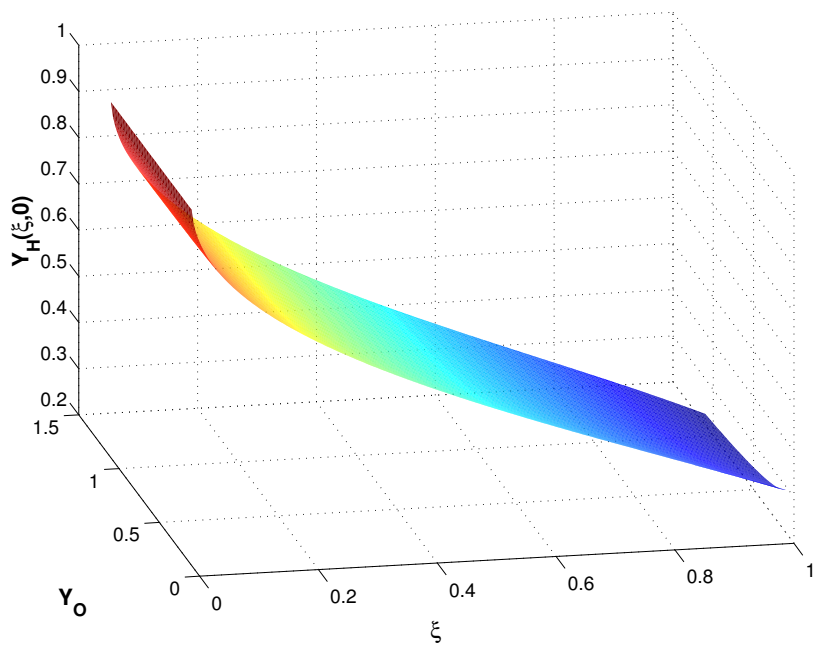


Figure 6.12: Plot of the surface mass fraction of hydrogen,  $Y_H(\xi, 0)$ , against  $\xi$  and varying values of the mass fraction of oxygen on the air side of the cell  $Y_O$ . This demonstrates how the surface mass fraction of hydrogen varies when the concentration of oxygen present within the cathode is altered.

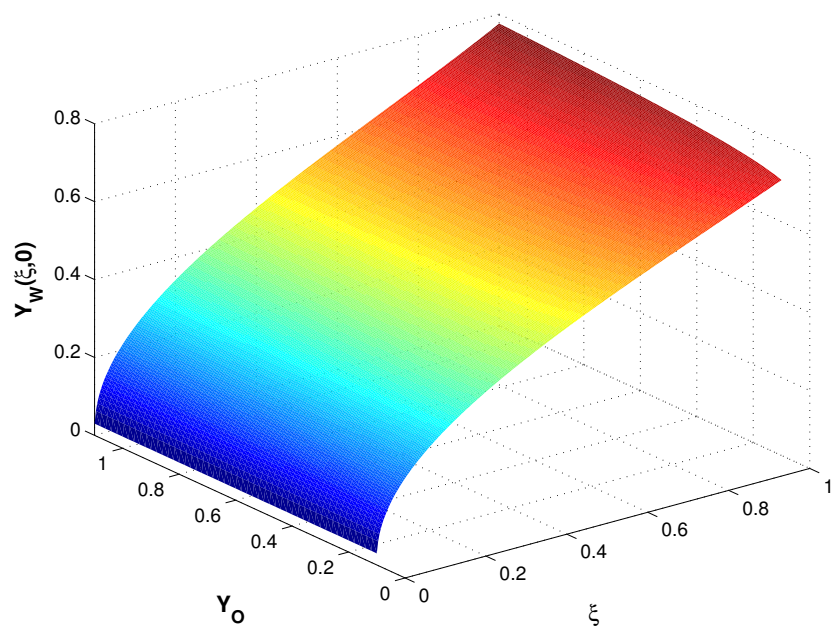


Figure 6.13: Plot of the surface mass fraction of water,  $Y_W(\xi, 0)$ , against  $\xi$  and varying values of the mass fraction of oxygen on the air side of the cell  $Y_O$ . This demonstrates how the surface mass fraction of water varies when the concentration of oxygen present within the cathode is altered.

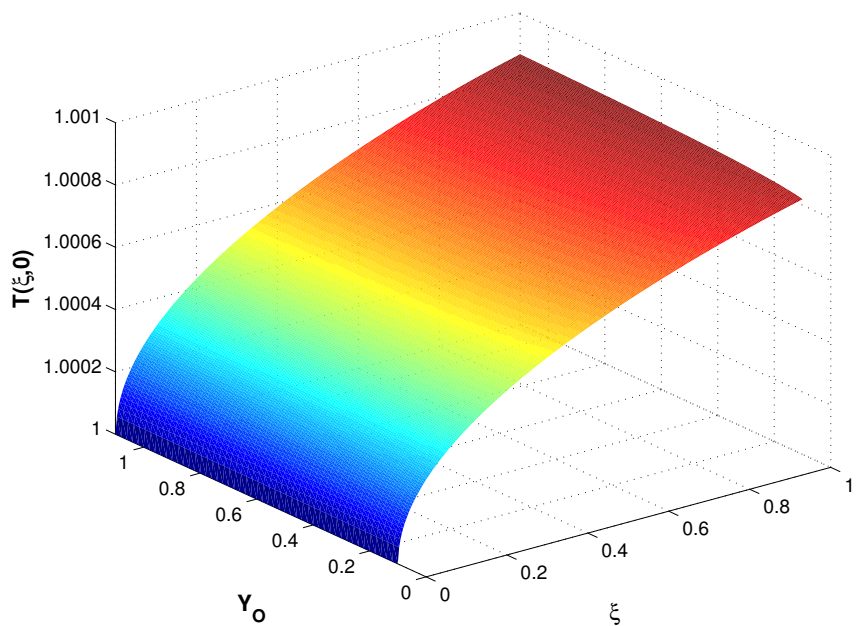


Figure 6.14: Plot of the surface temperature,  $T(\xi, 0)$ , against  $\xi$  and varying values of the mass fraction of oxygen on the air side of the cell  $Y_O$ . This demonstrates how the dimensionless absolute temperature along the surface varies when the concentration of oxygen present within the cathode is altered.

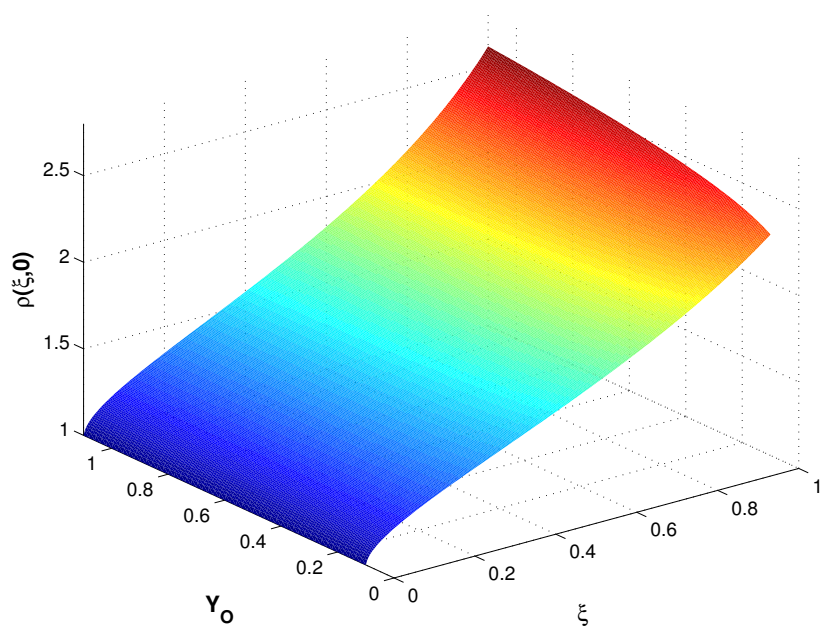


Figure 6.15: Plot of the surface density,  $\rho(\xi, 0)$ , against  $\xi$  and varying values of the mass fraction of oxygen on the air side of the cell  $Y_O$ . This demonstrates how the dimensionless density along the surface varies when the concentration of oxygen present within the cathode is altered.

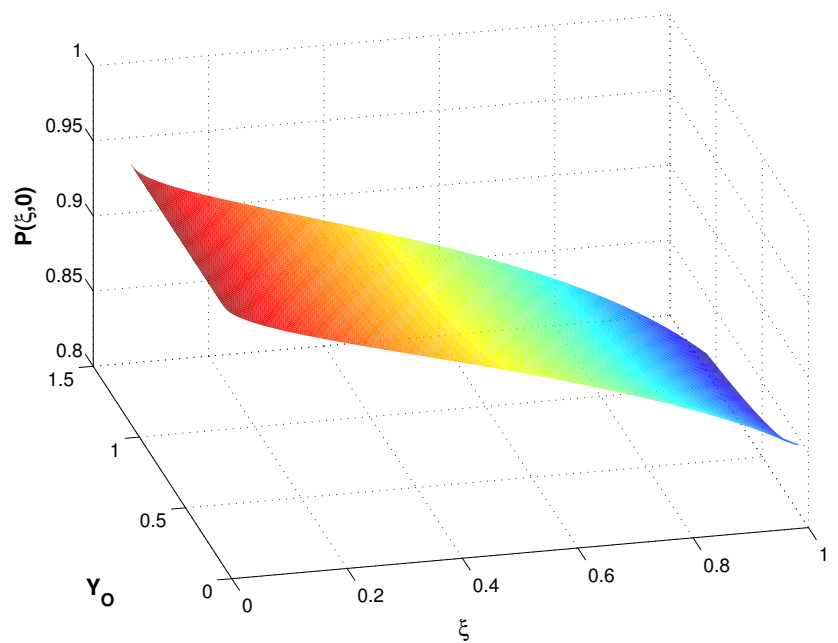


Figure 6.16: Plot of the surface pressure,  $P(\xi, 0)$ , against  $\xi$  and varying values of the mass fraction of oxygen on the air side of the cell  $Y_O$ . This demonstrates how the dimensionless pressure along the surface varies when the concentration of oxygen present within the cathode is altered.

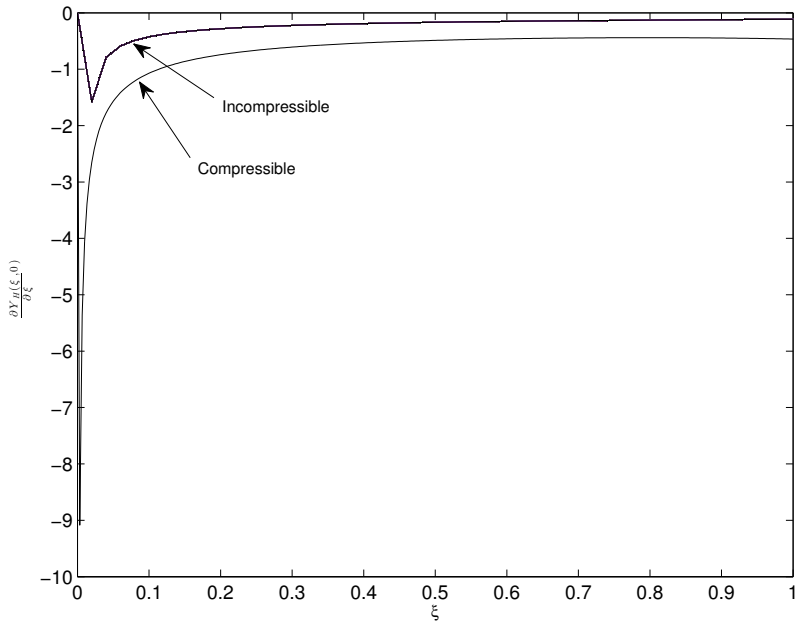


Figure 6.17: Plot of the comparison in the reaction rate of hydrogen between the incompressible and compressible models.

ratios, and that the system was not isothermal. Making these two additions to the model in chapter 3 increased the complexity of the model dramatically in terms of both analytical and numerical solutions. Once again we linked the reaction rates of species to the electrochemical parameters of the cell and due to the exothermic nature of this reaction we also linked the temperature variations at the plate with the same electrochemical parameters. From this base model we introduce non-dimensional variables before applying self-similarity to simplify the numerical problem. A consequence of this model was the problem of a singularity at the leading edge of the plate so we constructed an asymptotic solution for  $\xi \ll 1$ . Further to this we constructed a numerical solution for the full flow domain. The numerical results we obtained demonstrated that the reaction rate of hydrogen was far greater in the case of compressible flow compared to the incompressible case demonstrated in chapter 3. Moreover, although we made the assumption that the system is not isothermal we showed that in the case of this model we have an almost

isothermal system. We also went on to show how cell potential and mass fraction of oxygen within the cathode effected the variables within the model.

# CHAPTER 7

## ELECTRICAL MODEL

In chapter 6 we constructed a model for the flow and reaction of a compressible mixture of hydrogen and water across a flat, semi-infinite, impermeable plate. We presented numerical solutions which identified how the mass fractions of species, temperature, density and pressure all vary with respect to varying values of the cell potential. We now seek to develop details regarding the electrical performance of the model by examining how the current and power densities vary with changing values of cell potential. From this we can gain optimal operating conditions for planar SOFCs.

### 7.1 Current-voltage plot

To calculate the current density that corresponds to the value of cell potential we require a link between the two variables. This was introduced in section 6.2 and is given by

$$i(x) = 2Fq_e(x), \quad (7.1)$$

We have seen that the ion flux density  $q_e(x)$  can be written as

$$q_e(x) = \frac{RT}{4F^2 R_s} \left[ \ln \left( \frac{Y_H Y_O^{\frac{1}{2}}}{Y_W} \right) + \ln \left( \frac{m_W (\rho_a R T_a)^{\frac{1}{2}}}{m_H m_O^{\frac{1}{2}}} \right) + \frac{2F}{RT} (U^r - U_{cell}) \right] \quad (7.2)$$

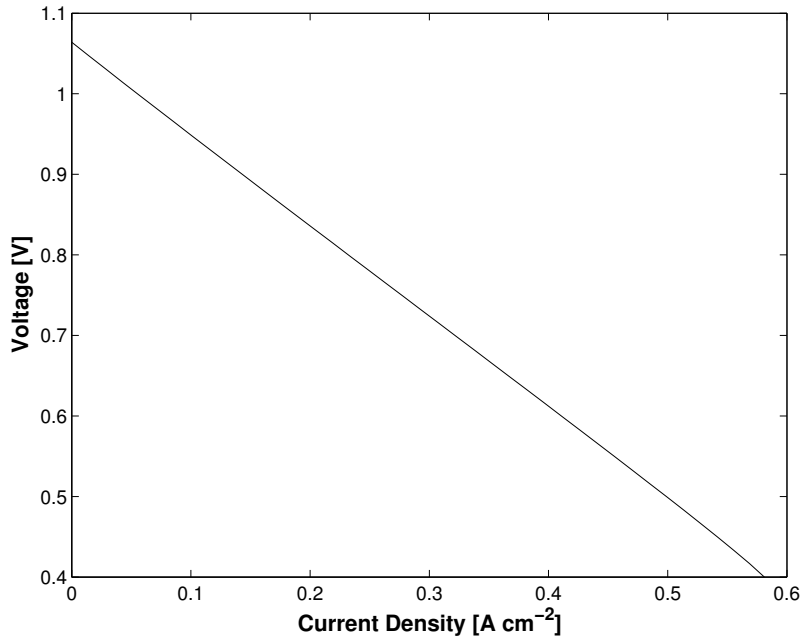


Figure 7.1: Average current-voltage plot across the length  $0 \leq \xi \leq 1$ . This demonstrates the relationship between the cell voltage and current density for this model.

Equations (7.1) and (7.2) represent a coupled system that will allow us to determine the current density of our model.

Fig. 7.1 represents the current density  $i(\xi)$  plotted against the cell potential  $U_{cell}$  for the average values of each of these variables for  $0 \leq \xi \leq 1$ . These curves are known as I-V curves and are one of the fundamental aspect in examining the electrical performance of a particular cell or cell stack. This plot shows that there is a linear relationship between the current density and the cell potential. This is because the only overpotential that we consider within this model is the ohmic overpotential which we would expect to give a linear relationship.

In Fig. 7.1 we examined the average current-voltage curve across the entire surface on the plate. However, as can be seen from equation (7.2) these curves can vary locally since they are directly linked to the local mass fractions of both hydrogen and water species. In Fig. 7.2 we have plotted a series of I-V curves for varying points along the surface of

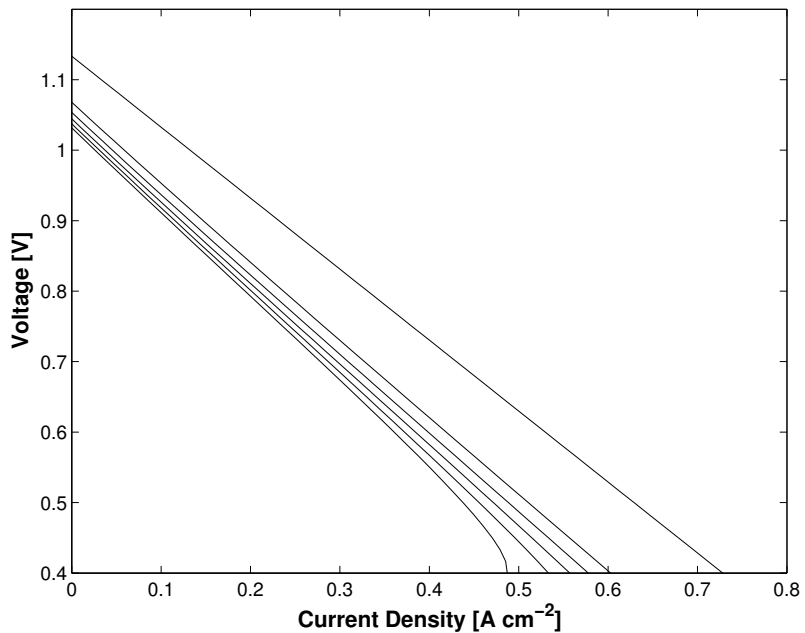


Figure 7.2: Comparison of current-voltage plots for varying values of  $\xi$ ,  $\xi=0, 0.2, 0.4, 0.6, 0.8, 1$ , where increasing  $\xi$  corresponds to a right to left shift in curves. This demonstrates how the relationship between cell potential and current density varies at different positions along the plate.

the plate at  $\xi=0, 0.2 0.4 0.6 0.8 1$ . The line on the far right corresponds to  $\xi = 0$  and the shift left in the plots correspond to increasing values of  $\xi$ . We can see a large variation between the line for  $\xi = 0$  and  $\xi = 0.2$  which is due to the severity of the reaction rate of hydrogen within this region, more details of which are found in Fig. 6.2.

## 7.2 Current-power plot

In the previous section we gave details regarding the link between the cell potential and the current density. However, these characteristics do not give details regarding the power which a cell can output. Identifying and optimising the power output of a cell is key in not only the design but the implementation of fuel cells into current markets. The main aim is to identify what operational cell potential leads to the highest power density output for a particular cell or cell stack. We are therefore required to relate the power output to

the cell potential, which is given by

$$P(x) = i(x)U_{cell}, \quad (7.3)$$

where  $P(x)$  is the local power density which is produced. We have demonstrated in Figs. 7.1 and 7.2 that there is a linear relationship between the current density and the cell potential. We would therefore expect there to be a quadratic relationship between the power density and the current density.

Fig. 7.3 represents the current density  $i$  plotted against the power density  $P$  for the average values of each of these variables along  $0 \leq \xi \leq 1$ . From this plot we can see that the maximum achievable power density is  $0.2505 \text{ W cm}^{-2}$  which occurs at a current density value of  $0.4702 \text{ A cm}^{-2}$ . If we examine Fig. 7.1 we can see that this current density value corresponds to an operating potential value of  $0.5328 \text{ V}$ . Therefore, in order to produce the maximum power output from this cell, operating at these conditions, we would need to operate the cell at  $0.5328 \text{ V}$ .

Due to the relationship between power, current and potential we would expect there to be variations within the power density at different points along the plate, as we saw with the I-V curves. In Fig. 7.4 we have plotted the power density against the current density for varying cell positions along the plate, for  $\xi=0, 0.2, 0.4, 0.6, 0.8, 1$ . The top curve, where the maximum power density occurs, relates to the point  $\xi = 0$  along the surface of the plate and decreasing curves correspond to increasing values of  $\xi$ . As with the I-V curves we have a significant difference in the power curves for  $\xi = 0$  and  $\xi = 0.2$ , again due to the reaction rate of hydrogen varying so drastically between these two points.

In section 6.7 we examined the effects of the model variables when changing the amount of the mass fraction of oxygen on the air side of the cell. We now use the results from this to examine the effects of oxygen variation on the power output of the cell in order to obtain an optimal operating mass fraction for oxygen. In Fig. 7.5 we have plotted the

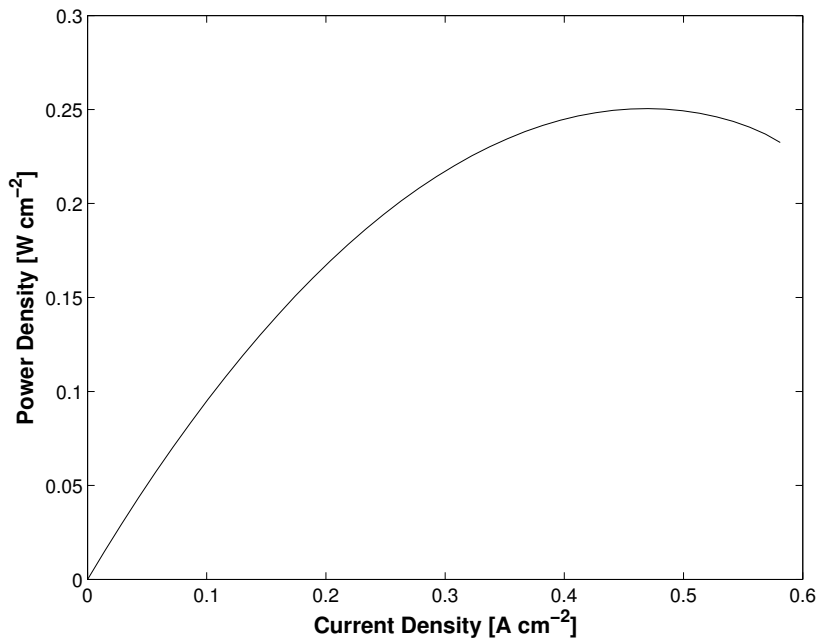


Figure 7.3: Average current-power plot across the length  $0 \leq \xi \leq 1$ . This demonstrates the relationship between the cell power density and current density for this model.

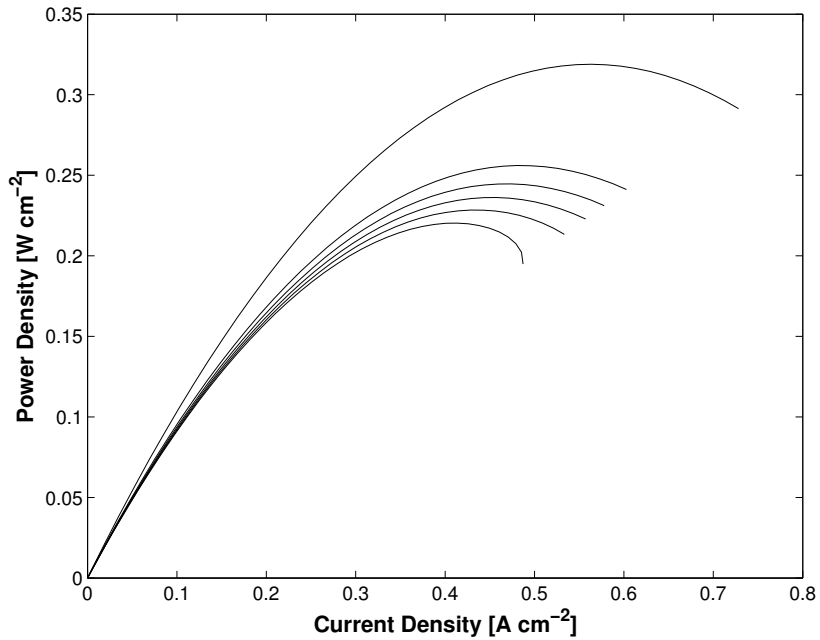


Figure 7.4: Comparison of current-power plots for varying values of  $\xi$ ,  $\xi=0, 0.2, 0.4, 0.6, 0.8, 1$ , where increasing  $\xi$  corresponds to a right to left shift in curves. This demonstrates how the relationship between the cell power density and current density varies at different positions along the plate.

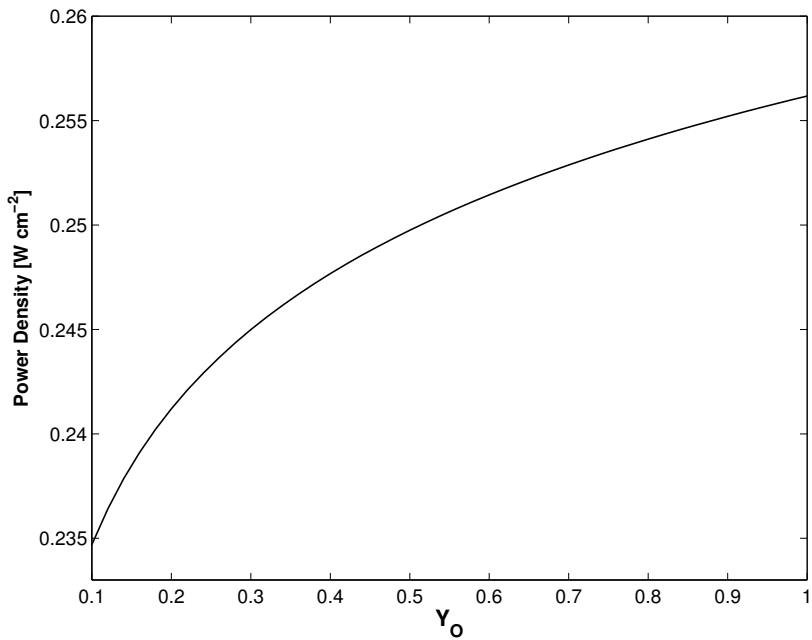


Figure 7.5: Average power density plotted against varying values of the mass fraction of oxygen on the air side,  $Y_O$ , for  $U_{cell} = 0.5$ . This demonstrates how the achievable cell power density varies when the oxygen mass fraction within the cathode side of the cell is altered.

power density against the mass fraction of oxygen for a cell potential value of  $U_{cell} = 0.5$ . We can see from this plot that increasing the mass fraction of oxygen on the air side of the cell increases the overall power density produced by that cell. More specifically, increasing the mass fraction from  $Y_O = 0.1$  to  $Y_O = 1$  gives an increase in the power density of  $0.0215 \text{ W cm}^{-2}$ . We expect this result to occur since upon examination of (7.2) we can see that increasing  $Y_O$  will give a resulting increase in the ion flux density.

### 7.3 Comparison with experimental data

An essential measure of the validity of any model is with a comparison between the model results and what the model was set out to predict. Having this validation allows the model to be confidently used to predict whatever it is the creator would like to predict. In the case of fuel cells it alleviates the need for continual experimental work which takes up a

significant amount of time and resources. Models in this context can give experimentalist accurate conditions for optimal performance when given a set of operating conditions.

The difficulty in validating this model is in obtaining experimental data which aligns exactly with our model. It is of paramount importance that the experimental data aligns with our model in order to give the optimal validation of the numerical results. On-site experimental data was not achievable due to work not aligning with the current model and the time constraints in constructing a specialised experimental set up for this model alone. Therefore, the only option was to seek previously published experimental work. Obtaining published experimental data was difficult due to the specific nature of the model but this was eventually achievable.

The experimental data used for our model validation is taken from Verbraeken *et al.* (2012) where the authors operated a planar SOFC on an inlet of humidified hydrogen at a temperature of 900 °C(1173 K). We have used their result from current-voltage and current-power plots and made comparisons to similar results from our model. It must be noted here that we have slightly varied the value of the specific resistance of the electrolyte substrate  $R_s$  to fit with the experimental results. This is viable since this parameter does not take a specific value and the value we have used is still the same order of magnitude as that utilised by previous authors (Cooper *et al.*, 2000).

Fig. 7.6 plots the numerical (solid line) and experimental (broken line) I-V curves for values of  $T_0 = 1173\text{ K}$  and  $R_s = 1.007 \times 10^{-4}\text{ }\Omega\text{ cm}^{-2}$ . We can see that the two lines are in very good agreement for all values of the current density. Slight differences between the numerical and experimental data are expected due to the assumption that the only overpotential we consider is that of the ohmic overpotential.

A comparison of the current-power plots can be found in Fig. 7.7 where the numerical (solid line) and experimental (broken line) results for  $T_0 = 1173\text{ K}$  and  $R_s = 1.007 \times 10^{-4}\text{ }\Omega\text{ cm}^{-2}$  have been plotted. Once again the two plots are in very good agreement

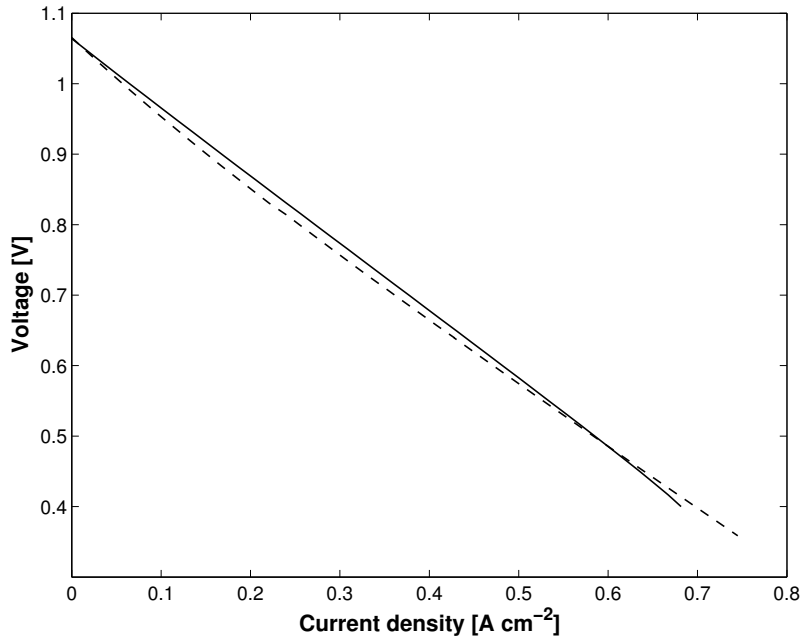


Figure 7.6: Comparison of the current-voltage plots of the numerical model (solid line) and experimental data (Verbraeken *et al.*, 2012) (broken line) for  $T_0 = 1173$  and  $R_s = 1.007 \times 10^{-4}$ .

for all of the values of current density within our model. We can see that the greatest differences occur for high values of the current density. One reason for this could be the non-existence of the concentration overpotential which comes into effect within this region, see Fig. 2.8 for a visual representation of fuel cell overpotentials. However, the model results are extremely accurate without the addition of extra overpotentials which add additional complexity to the model and inefficiency to the numerical algorithm.

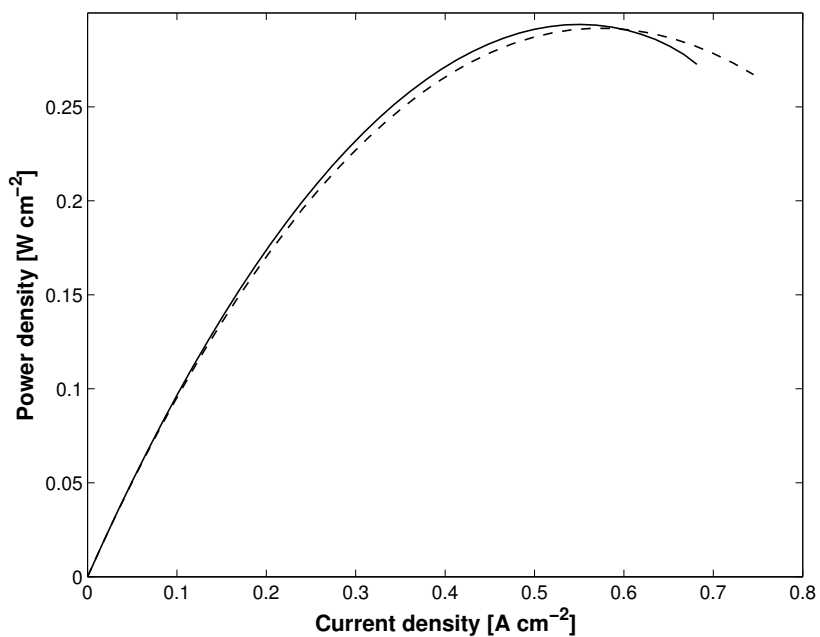


Figure 7.7: Comparison of the current-power plots of the numerical model (solid line) and experimental data (Verbraeken *et al.*, 2012) (broken line) for  $T_0 = 1173$  and  $R_s = 1.007 \times 10^{-4}$ .

# CHAPTER 8

## CONCLUSIONS AND FUTURE WORK

The aim of this thesis was to construct a model for a planar SOFC from first principles applying the necessary model equations to begin with before adding in extra complexities. The benefits in doing this were to obtain a solution which is not only analytically accurate but also numerically efficient. This was to enable fuel cell models to align more closely with industry demands for faster computational time compared to the current literature.

Within chapters 3 and 5 a simplistic model was created to examine the flow and reaction of an incompressible mixture of species across a flat, semi-infinite plate. This model was constructed to depict a planar SOFC. As part of the chapters we constructed an analytical framework which considered the solution close to naturally occurring singularities in the flow. This rigorous form of mathematical analysis is novel to current fuel cell literature and it enables us to use the model equations with confidence throughout the flow domain whilst understanding the flow dynamics close to the singularity. A numerical solution was also constructed to calculate the solution to model equations throughout the full flow domain. The benefits of adopting this approach were the calculation of numerical solutions within seconds which is materially more efficient than consensus within the current literature. Moreover, the model was demonstrated to be versatile to changes in mixture composition with the examination of humidified hydrogen and methane as inlet

fuels.

Although the results within chapters 3 and 5 may not be exactly indicative of an operational planar SOFC, due to the number of assumptions made, it enabled us to build a governing accurate and efficient modelling framework. This framework also benefited from having the flexibility to be applied to more complex systems in order to generate models with the ability to predict empirical data. Moreover, as part of the modelling framework, an electrochemical model was built in order to predict the electrical performance of the cell for varying operating conditions. Results of this for the incompressible model were presented within chapter 4.

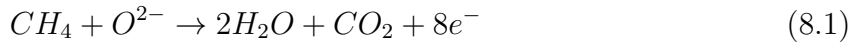
The most significant results within this thesis were presented within chapters 6 and 7 where we extended the models of the previous chapters to take into account compressibility and thermal affects within the flow. This model utilised the framework developed in the previous chapters to construct an analytical and numerical solution. Moreover, the electrochemical model from the previous chapters was used to examine the electrical performance of the cell. The results from the electrochemcial model were compared to that of experimental data and demonstrated an almost identical relationship. These results highlighted the accuracy of this model and its ability to predict the performance of a planar SOFC. Coupling this with a numerical run time to the order of seconds means that this model has bridged the gap between accuracy, mathematical rigour and numerical efficiency. The results are a model novel in the current fuel cell literature and also one which could greatly enhance the commercialisation of fuel cells through rapid accurate modelling.

## 8.1 Future work

We mentioned in chapter 2 that there is a lack of rigorous mathematical models depicting SOFCs and the operations involved within SOFCs. Therefore, the scope for future work

is vast, extending the work from this thesis or indeed moving into alternative SOFC modelling areas. Within this section we will give details of what we think are the significant future work areas moving forward from this thesis.

One way in which the work within this thesis could be extended is through introducing more dependence between the species and the electrochemical parameters within chapter 5. We showed in this chapter that only the species involved within the hydrogen oxidation reaction have a dependence on the electrochemical parameters. However, there is evidence to suggest that all of the species involved within this model should depict some dependence on these (Cooper *et al.*, 2000). Therefore, one way in which we can introduce this dependence on electrochemical parameters is to introduce the additional reaction structure



into the existing structure of chapter 5. Including these additional reactions would alter the mass-flux boundary conditions on the surface of the plate to give

$$D_f \frac{\partial Y_f}{\partial y} = \frac{k_1 Y_f Y_W \rho}{m_W} + \frac{k_2 Y_f Y_D \rho}{m_D} + \frac{q_e(x) m_f}{4\rho}, \quad (8.3)$$

$$D_h \frac{\partial Y_h}{\partial y} = 0, \quad (8.4)$$

$$D_D \frac{\partial Y_D}{\partial y} = \frac{k_2 Y_f Y_D \rho}{m_f} - \frac{k_3 Y_M Y_W \rho m_D}{m_M m_W} - \frac{5q_e(x) m_D}{4\rho}, \quad (8.5)$$

$$D_W \frac{\partial Y_W}{\partial y} = \frac{k_1 Y_f Y_W \rho}{m_f} + \frac{k_3 Y_M Y_W \rho}{m_M} - \frac{3q_e(x) m_W}{2\rho}, \quad (8.6)$$

$$D_M \frac{\partial Y_M}{\partial y} = \frac{k_3 Y_M Y_W \rho}{m_W} - \frac{k_1 Y_f Y_W \rho m_M}{m_f m_W} - \frac{2k_2 Y_f Y_D \rho m_M}{m_f m_D} + \frac{q_e(x) m_D}{\rho}, \quad (8.7)$$

$$D_H \frac{\partial Y_H}{\partial y} = \frac{q_e(x) m_H}{\rho} - \frac{3k_1 Y_f Y_W \rho m_H}{m_f m_W} - \frac{2k_2 Y_f Y_D \rho m_H}{m_f m_D} - \frac{k_3 Y_M Y_W \rho m_H}{m_M m_W}, \quad (8.8)$$

where we can see here that all of the species, apart from the inert helium, has some proportion of dependence on the electrochemical parameters incorporated within the function  $q_e(x)$ . From this we are able to adopt the same method, both analytically and numerically, as used in chapter 5.

One obvious extension of this thesis will be to take the models for the compressible flow and reaction demonstrated in chapters 6 and 7 and apply them to higher hydrocarbon inlet mixtures. The most important of these hydrocarbon mixtures to consider will be that a methane due to its commercial advantage and reaction kinetics at higher temperature. This would therefore alter the reaction structure from the hydrogen oxidation reaction to a set of reactions present in Table 2.1. The main reason why we will seek to do this is due to the correlation between the model outputs and experiential data represented in chapter 7. Therefore, having a model for a methane inlet would allow us to optimise the performance for both hydrogen and methane operated cells.

Another area in which the current models within this thesis can be extended will be through the inclusion of a complete set of overpotentials. For flow and reaction over a flat plate we can reduce the cell overpotentials down to just the ohmic overpotential and we

have shown that doing this gives a very accurate match to the experimental data, shown in chapter 7 . However to obtain a completely accurate electrochemical model we will look to introduce the activation overpotential, which takes the form

$$i = i_{0,electrode} \left[ \exp \left( \frac{\alpha zF}{RT} \eta_{act,electrode} \right) - \exp \left( -\frac{(1-\alpha)zF}{RT} \eta_{act,electrode} \right) \right], \quad (8.9)$$

It has been shown that for low activation overpotentials,  $\eta_{act} < 0.1$ , their is a linear relationship between the current density and the activation overpotential (Janardhanan & Deutschmann, 2007)

$$\eta_{act} = i \frac{RT}{zFi_0} \quad (8.10)$$

We will also include the concentration overpotential

$$\eta_{con} = \frac{RT}{zF} \ln \left( \frac{P_{H_2}^{bulk} P_{H_2O}^{react}}{P_{H_2}^{react} P_{H_2O}^{bulk}} \right) + \frac{RT}{2zF} \ln \left( \frac{P_{O_2}^{bulk}}{P_{O_2}^{react}} \right) \quad (8.11)$$

which can also be written in terms of the current density

$$\eta_{con,electrode} = \frac{RT}{2F} \ln \left( 1 - \frac{i}{i_L} \right) \quad (8.12)$$

where  $i_L$  is the limiting current which can be taken to be the maximum rate at which a reactant can be supplied to an electrode (Bove & Ubertini, 2008). The difficulty in including the concentration overpotential into our current model setup is isolating the current density within (8.12). This may mean adopting an alternative approach of treating the current density as a variable and then measuring the cell potential using an overall cell potential equation of the form

$$U_{cell} = U^N - (\eta_{ohm} + \eta_{act} + \eta_{con}) \quad (8.13)$$

and then re-write the model by replacing the ion flux density  $q_e(x)$  by its definition

$$q_e(x) = \frac{i(x)}{2F} \quad (8.14)$$

# APPENDIX A

## DERIVATION OF BOUNDARY-LAYER EQUATIONS

A main criterion for a well defined laminar boundary layer is that the Reynolds number must be large,  $Re \rightarrow \infty$ , where we define the Reynolds number to be

$$Re = \frac{U_0 L}{\nu}. \quad (\text{A.1})$$

where  $L$  is a given length scale. We will require that the Reynolds number is not too large as to move into a transition or even turbulent phase, values of which are shown above for certain cases. The first step is to show an existence of a solution of the equations of motion for large values of  $Re$  but when  $Re$  is not infinite. There are now two main methods which can be used to generate the laminar boundary-layer equations, both of which will be explained below for the case of the equations of motion for a two-dimensional incompressible flow

$$\frac{\partial u}{\partial t} + u \frac{\partial u}{\partial x} + v \frac{\partial u}{\partial y} = - \frac{1}{\rho} \frac{\partial p}{\partial x} + \nu \left( \frac{\partial^2 u}{\partial x^2} + \frac{\partial^2 u}{\partial y^2} \right), \quad (\text{A.2})$$

$$\frac{\partial v}{\partial t} + u \frac{\partial v}{\partial x} + v \frac{\partial v}{\partial y} = - \frac{1}{\rho} \frac{\partial p}{\partial y} + \nu \left( \frac{\partial^2 v}{\partial x^2} + \frac{\partial^2 v}{\partial y^2} \right), \quad (\text{A.3})$$

$$\frac{\partial u}{\partial x} + \frac{\partial v}{\partial y} = 0. \quad (\text{A.4})$$

### Method of Orders of Magnitude.

This is the original method for obtaining the boundary-layer equations from the equations of motion by examining the order of magnitude of each term as  $Re \rightarrow \infty$  and is due to Prandtl (1904) and Blasius (1908). On assessing the orders of magnitude of each term with the equations (A.2)-(A.4) it follows that the term  $t, x, u$  are of order of unity and thus we may write

$$\frac{\partial}{\partial t} \sim 1, \quad \frac{\partial}{\partial x} \sim 1, \quad (\text{A.5})$$

in this case  $u$  is the velocity within the boundary-layer and so the value of  $u$  can change rapidly from the surface to the freestream value. Now the thickness of the boundary-layer has to be shown to be approximated by  $\delta$  and so we define the order of the thickness to be this value, where  $\delta \ll 1$ , and hence

$$\frac{\partial}{\partial y} \sim \delta^{-1}, \quad \frac{\partial^2}{\partial y^2} \sim \delta^{-2}, \quad (\text{A.6})$$

Since the first term in the continuity equation (A.4) is of order unity, it must follow that the transverse velocity component to the solid surface is

$$v \sim \delta. \quad (\text{A.7})$$

Therefore, we have now obtained the orders of magnitude for all the parameters within the equations of motion. Now we must compare the orders of each terms within the equations and simplify according to leading order terms. Hence, the equations of motion with respective orders of magnitude are

$$\frac{\partial u}{\partial t} + u \frac{\partial u}{\partial x} + v \frac{\partial u}{\partial y} = -\frac{1}{\rho} \frac{\partial p}{\partial x} + \nu \left( \frac{\partial^2 u}{\partial x^2} + \frac{\partial^2 u}{\partial y^2} \right), \quad (\text{A.8})$$

1	1	1	$\delta \delta^{-1}$	
				$1 \quad \delta^{-2}$

$$\frac{\partial v}{\partial t} + u \frac{\partial v}{\partial x} + v \frac{\partial v}{\partial y} = -\frac{1}{\rho} \frac{\partial p}{\partial y} + \nu \left( \frac{\partial^2 v}{\partial x^2} + \frac{\partial^2 v}{\partial y^2} \right), \quad (\text{A.9})$$

$\delta$	1	$\delta$	$\delta \delta/\delta$	
				$\delta \quad \delta/\delta^2$

$$\frac{\partial u}{\partial x} + \frac{\partial v}{\partial y} = 0. \quad (\text{A.10})$$

			$\delta/\delta$	
--	--	--	-----------------	--

From (A.8), and the property that  $\delta \ll 1$ , we can deduce that within the viscous terms

$$\frac{\partial^2 u}{\partial x^2} \ll \frac{\partial^2 v}{\partial y^2}, \quad (\text{A.11})$$

and thus the first of these terms can be neglected. Hence, in order for the viscous and inertia terms to be of the same order of magnitude, it must follow that

$$\nu \sim \delta^2, \quad (\text{A.12})$$

which implies that the thickness of the boundary-layer is of the order  $Re^{-\frac{1}{2}}$ . From equation

(A.9) we may conclude that the pressure normal to the surface is of the order  $\delta$  and that the pressure variation across the boundary layer is of order  $\delta^2$ . Therefore, we may assume that the pressure in this direction is constant and takes the value of the pressure outside of the boundary-layer where the flow is inviscid.

At the outer edge of the boundary-layer the streamwise velocity  $u$  equals that of the freestream velocity  $U_0$ , which does not vary in the normal direction. Thus we can neglect the viscous terms in the equations of motion to obtain the equation for the outer flow

$$\frac{\partial U_0}{\partial t} + U_0 \frac{\partial U_0}{\partial x} = -\frac{1}{\rho} \frac{\partial p}{\partial x}. \quad (\text{A.13})$$

under steady state conditions this may take the form of the standard Bernoulli equation.

The equations of motions for the boundary-layer, simplified from the Navier-Stokes equations, are known as the Prandtl boundary-layer equations, and take the form

$$\frac{\partial u}{\partial t} + u \frac{\partial u}{\partial x} + v \frac{\partial u}{\partial y} = -\frac{1}{\rho} \frac{\partial p}{\partial x} + \nu \frac{\partial^2 u}{\partial y^2}, \quad (\text{A.14})$$

$$\frac{\partial u}{\partial x} + \frac{\partial v}{\partial y} = 0. \quad (\text{A.15})$$

The relative boundary conditions depend on the model in which the above equations have been applied to.

### **Non-dimensional Method.**

Although the above method is more commonly used, and referred to when deriving the boundary-layer equations, a new method was produced by Rosenhead (1963) which looks at non-dimensionalisation of the equations of motion. Rosenhead explains how this new method is more precise but maybe physically harder to understand compared to consideration of the orders of magnitude. In Rosenhead's analysis of the equations of motion (A.2)-(A.4) the following non-dimensional variables are defined

$$\bar{x} = x/l, \quad \bar{y} = Re^{\frac{1}{2}}y/L, \quad \bar{t} = Ut/L, \quad \bar{u} = u/U, \quad \bar{v} = Re^{\frac{1}{2}}v/U, \quad \bar{p} = p/\rho U^2. \quad (\text{A.16})$$

On substituting the above into the equations of motion we obtain

$$\frac{\partial \bar{u}}{\partial \bar{t}} + \bar{u} \frac{\partial \bar{u}}{\partial \bar{x}} + \bar{v} \frac{\partial \bar{u}}{\partial \bar{y}} = - \frac{\partial \bar{p}}{\partial \bar{x}} + \frac{1}{Re} \frac{\partial^2 \bar{u}}{\partial \bar{x}^2} + \frac{\partial^2 \bar{u}}{\partial \bar{y}^2}, \quad (\text{A.17})$$

$$\frac{1}{Re} \left( \frac{\partial \bar{v}}{\partial \bar{t}} + \bar{u} \frac{\partial \bar{v}}{\partial \bar{x}} + \bar{v} \frac{\partial \bar{v}}{\partial \bar{y}} \right) = - \frac{\partial \bar{p}}{\partial \bar{y}} + \frac{1}{Re^2} \frac{\partial^2 \bar{v}}{\partial \bar{x}^2} + \frac{1}{Re} \frac{\partial^2 \bar{v}}{\partial \bar{y}^2}, \quad (\text{A.18})$$

$$\frac{\partial \bar{u}}{\partial \bar{x}} + \frac{\partial \bar{v}}{\partial \bar{y}} = 0, \quad (\text{A.19})$$

If we assume here that all the non-dimensional derivatives have the same order of magnitude for large values of  $Re$  then the above equations become, on dropping the bars for convenience

$$\frac{\partial u}{\partial t} + u \frac{\partial u}{\partial x} + v \frac{\partial u}{\partial y} = - \frac{\partial p}{\partial x} + \frac{\partial^2 u}{\partial y^2}, \quad (\text{A.20})$$

$$0 = - \frac{\partial p}{\partial y}, \quad (\text{A.21})$$

$$\frac{\partial u}{\partial x} + \frac{\partial v}{\partial y} = 0, \quad (\text{A.22})$$

where the above are the boundary-layer equations but in a non-dimensional form, which can be re-transformed to generate the Prandtl boundary-layer equations already given.

# APPENDIX B

## CONCEPT OF SIMILARITY

The concept of similarity is a very useful tool when it comes to finding a solution to the boundary layer equations

$$\frac{\partial u}{\partial t} + u \frac{\partial u}{\partial x} + v \frac{\partial u}{\partial y} = -\frac{1}{\rho} \frac{\partial p}{\partial x} + \nu \frac{\partial^2 u}{\partial y^2}, \quad (\text{B.1})$$

$$\frac{\partial u}{\partial x} + \frac{\partial v}{\partial y} = 0. \quad (\text{B.2})$$

If we consider the steady state case of these equations with boundary conditions

$$u = v = 0 \quad \text{on } y = 0, \quad \text{and} \quad u = U(x) \quad \text{as } y \rightarrow \infty, \quad (\text{B.3})$$

then for a given kinematic viscosity,  $\nu$ , we can express the general solution to the boundary layer equations as

$$\frac{u}{U} = g(x, y), \quad (\text{B.4})$$

where  $g$  is given to be an arbitrary function of  $x$  and  $y$ . In certain special cases of boundary layer flow we are able to write

$$\frac{u}{U} = g(\eta), \quad (\text{B.5})$$

where  $\eta$  is defined to be a similarity variable and is a function of  $x$  and  $y$ . Hence, in the cases where this special similarity solution exists the problem reduces from one with two independent variables to a problem with just one. Thus, the boundary layer equations, above, can be transformed into a set of ordinary differential equations (ODEs) with respect to the similarity variable  $\eta$ .

The similarity concept is useful for scenarios such as laminar and turbulent flow without pressure gradients. However, most applications of boundary layers do not exhibit a similarity solution and so the boundary layer equations are required to be solved in full.

## B.1 Derivation of similarity variable $\eta$ .

We have shown above how the concept of a similarity solution is of great use in simplifying the boundary layer problem. However, we have not explained how the similarity variable  $\eta$  is found and under what conditions  $\eta$  actually exists. There are several methods that can be used to find  $\eta$  but we will present the group-theoretic method which can be found in greater detail in Hansen (1964) and Cebeci & Bradshaw (1977). We begin by considering the standard boundary layer equations (B.1) and (B.2) under steady state conditions and we introduce the following linear group transformation

$$x = A^{\alpha_1} \bar{x}, \quad y = A^{\alpha_2} \bar{y}, \quad u = A^{\alpha_3} \bar{u}, \quad v = A^{\alpha_4} \bar{v}, \quad U = A^{\alpha_5} \bar{U} \quad (\text{B.6})$$

where  $\alpha_i$ ,  $i = 1, \dots, 5$ , are constants and  $A$  is defined to be the parameter of transformation. Substitution of these transformations into the boundary layer equations yields

$$A^{2\alpha_3 - \alpha_1} \bar{u} \frac{\partial \bar{u}}{\partial \bar{x}} + A^{\alpha_4 + \alpha_3 - \alpha_2} \bar{v} \frac{\partial \bar{u}}{\partial \bar{y}} - A^{2\alpha_5 - \alpha_1} \bar{U} \frac{\partial \bar{U}}{\partial \bar{x}} - \nu A^{\alpha_3 - 2\alpha_2} \frac{\partial^2 \bar{u}}{\partial \bar{y}^2} = 0, \quad (\text{B.7})$$

$$A^{\alpha_3-\alpha_1} \frac{\partial \bar{u}}{\partial \bar{x}} + A^{\alpha_4-\alpha_2} \frac{\partial \bar{v}}{\partial \bar{y}} = 0 \quad (\text{B.8})$$

It is desirable that the above equations are invariant such that the transformation does not alter the boundary layer equations. For this to occur we require that the powers of  $A$  in each equation equate to one another. Hence, we obtain the system of equations for  $\alpha_i$

$$\alpha_3 - \alpha_1 = \alpha_4 - \alpha_2, \quad (\text{B.9})$$

$$2\alpha_3 - \alpha_1 = \alpha_4 + \alpha_3 - \alpha_2 = 2\alpha_5 - \alpha_1 = \alpha_3 - 2\alpha_2 \quad (\text{B.10})$$

where a partial solution exists

$$\alpha_3 = \alpha_5 = \alpha_1 - 2\alpha_2, \quad \alpha_4 = \alpha_2 \quad (\text{B.11})$$

Since we now have a relationship between the values of  $\alpha_i$  and we have the linear group transformation (B.6), by eliminating  $A$  we can obtain the relationship

$$A = \left(\frac{x}{\bar{x}}\right)^{\frac{1}{\alpha_1}} = \left(\frac{y}{\bar{y}}\right)^{\frac{1}{\alpha_2}}, \quad (\text{B.12})$$

which equates to

$$\frac{y}{x^\alpha} = \frac{\bar{y}}{\bar{x}^{-\alpha}}, \quad (\text{B.13})$$

where  $\alpha = \alpha_2/\alpha_1$ . We can arrive at a relationship between the other variables in a similar way, to obtain

$$\frac{u}{x^{1-2\alpha}} = \frac{\bar{u}}{\bar{x}^{-1-2\alpha}}, \quad \frac{v}{x^{-\alpha}} = \frac{\bar{v}}{\bar{x}^{-\alpha}}, \quad \frac{U}{x^{1-2\alpha}} = \frac{\bar{U}}{\bar{x}^{1-2\alpha}} \quad (\text{B.14})$$

These variables are defined to be absolute variables and are similarity variables if we can express the boundary conditions independent of  $x$ . Now we set

$$\eta = \frac{y}{x^\alpha}, \quad \bar{f}(\eta) = \frac{u}{x^{1-2\alpha}}, \quad \bar{g}(\eta) = \frac{v}{x^{-\alpha}}, \quad \bar{h}(\eta) = \frac{U}{x^{1-2\alpha}} = \text{Constant} \quad (\text{B.15})$$

and hence on transformation of the boundary conditions (B.3), we obtain

$$\bar{f} = \bar{g} = 0 \quad \text{on } \eta = 0, \quad \bar{f} = \text{Constant} \quad \text{as } \eta \rightarrow \infty \quad (\text{B.16})$$

Therefore, the boundary conditions for  $\bar{f}$  and  $\bar{g}$  are constant for constant values of  $\eta$  and hence they are independent of  $x$ . As described above this means that the absolute variables (B.15) are similarity variables. We may then substitute these similarity variables into our boundary layer equations to produce a set of equations in one variable  $\eta$ . If, under the above transformation, constant boundary conditions are not produced then no similarity solution will exist for the problem.

# APPENDIX C

## MIXTURE PROPERTIES

Within chapter 6 we gave details of the equations used to calculate the viscosity and density of a mixture of gases at low pressures (around 1 atm). For simplicity we neglected to consider the variations in the thermal conductivity of a mixture of gases and the specific heat capacity at constant pressure when the mixture composition varies. We will henceforth give details about how one would examine the variations in these values.

The thermal conductivity of a mixture of gases can be expressed in the form (Lindsay & Bromley, 1950)

$$k_m = \sum_{i=1}^n \frac{k_i}{\frac{1}{X_i} \sum_{l=1}^n X_l A_{lj}} \quad (\text{C.1})$$

where  $k_m$  is the mixture thermal conductivity,  $k_i$  are the species thermal conductivities,  $X_i$  is the mole fraction of the species and  $A_{ij}$  is an interaction parameter. This interaction parameter is defined by

$$A_{ij} = \frac{1}{4} \left\{ 1 + \left[ \frac{\mu_i}{\mu_l} \left( \frac{m_l}{m_i} \right)^{\frac{3}{4}} \left( \frac{T + S_i}{T + S_l} \right) \right]^{\frac{1}{2}} \right\}^2 \left( \frac{T + S_{il}}{T + S_i} \right) \quad (\text{C.2})$$

where  $S_i$  is the Sutherland's constant.  $S_i$  and  $S_{il}$  are given by

$$S_{il} = \sqrt{S_i S_l} \quad S_i = 1.5T_{b_i} \quad (\text{C.3})$$

where  $T_{b_i}$  is the absolute boiling temperature of species  $i$  at 1 atm of pressure. In relevance to the model constructed in chapter 6 it is worth noting that  $S_H = 79K$ . It is noted that the relationship for  $S_i$  is not a good assumption but for large errors in this equation only give small errors in the mixture thermal conductivity occur (Lindsay & Bromley, 1950). Therefore, it is sufficient to use this simplification.

The specific heat capacity of a mixture at constant pressure is represented by (Perry & Green, 2008)

$$C_{P,m} = \sum_{i=1}^n X_i C_{P,i} \quad (\text{C.4})$$

## BIBLIOGRAPHY

- ACHESON, D. J. 1990 *Elementary fluid dynamics*. Oxford University Press.
- AGUIAR, P., ADJIMAN, C. & BRANDON, N. 2004 Anode-supported intermediate temperature direct internal reforming solid oxide fuel cell. i: model-based steady-state performance. *J. Power Sources* **138** (1), 120–136.
- AKHTAR, N. 2009 *Single-Chamber, Solid Oxide Fuel Cells: Modelling and Experiments*. Master's Thesis, The University of Birmingham.
- AKHTAR, N., DECENT, S., LOGHIN, D. & KENDALL, K. 2009 Mixed-reactant, micro-tubular solid oxide fuel cells: An experimental study. *Journal of Power Sources* **193** (1), 39–48.
- ANDERSON JR, J. D. 2005 Ludwig prandtl's boundary layer. *Physics Today* **58** (12), 42–48.
- ANDREWS, J. W. 2008 *Long Slender Solid Oxide Fuel Cells*. PhD Thesis, The Univerisity of Birmingham.
- ARIMA, T. 2006 Numerical methods for chemically reacting fluid flow computation under low-mach number approximation. *Tokyo Journal of Mathematics* **29** (1), 167–198.
- ARMOR, J. N. 1999 The multiple roles for catalysis in the production of h2. *Applied Catalysis A: General* **176** (2), 159–176.
- BARBIR, F. & GÓMEZ, T. 1997 Efficiency and economics of proton exchange membrane (pem) fuel cells. *International Journal of Hydrogen Energy* **22** (1011), 1027 – 1037.
- BESSETTE, N., WEPFER, W. & WINNICK, J. 1995 A mathematical model of a solid oxide fuel cell. *J. Electrochem. Soc.* **142**, 3792.
- BILLINGHAM, J., KING, A., COPCUTT, R. & KENDALL, K. 1999 Analysis of a model for a loaded, planar, solid oxide fuel cell. *SIAM J. Appl. Maths* pp. 574–601.
- BIRD, R. B., STEWART, W. E. & LIGHTFOOT, E. N. 2006 *Transport phenomena*. Wiley.

- BLASIUS, H. 1908 Boundary layers in fluids with small friction. *Zeitschrift fuer Mathematische und Physik* **56**, 1–37.
- BOVE, R. & UBERTINI, S. 2006 Modeling solid oxide fuel cell operation: Approaches, techniques and results. *J. Power Sources* **159**, 543–549.
- BOVE, R. & UBERTINI, S. 2008 *Modeling solid oxide fuel cells: methods, procedures and techniques*, , vol. 1. Springer Science+ Business Media.
- BROMLEY, L. & WILKE, C. 1951 Viscosity behavior of gases. *Industrial & Engineering Chemistry* **43** (7), 1641–1648.
- CAMUS, A. 1998 *L'Etranger 3rd edition*. Routledge.
- CEBEKI, T. & BRADSHAW, P. 1977 *Momentum Transfer in Boundary Layers*. McGraw-Hill.
- CHAUDHARY, M. & MERKIN, J. 1995 Free convection boundary layers driven by exothermic surface reactions: critical ambient temperatures. *Mathematical Engineering in Industry* **5** (2), 129–145.
- CIMENTI, M. & HILL, J. M. 2009 Direct utilization of liquid fuels in sofc for portable applications: challenges for the selection of alternative anodes. *Energies* **2** (2), 377–410.
- COHEN, C. B. & RESHOTKO, E. 1955 *The compressible laminar boundary layer with heat transfer and arbitrary pressure gradient*. National Advisory Committee for Aeronautics.
- COOPER, R. J., BILLINGHAM, J. & KING, A. C. 2000 Flow and reaction in solid oxide fuel cells. *J. Fluid Mech.* **411**, 233–262.
- COPCUTT, R., KING, A. & KENDALL, K. 1996 Reaction-diffusion of fuel with air between planar solid oxide fuel cells stacked with ceramic felt. *Proc. R. Soc. Lond. A* **452** (1955), 2639–2653.
- COSTAMAGNA, P., SELIMOVIC, A., BORGH, M. D. & AGNEW, G. 2004 Electrochemical model of the integrated planar solid oxide fuel cell (ip-sofc). *Chem. Eng. J.* **102**, 61–69.
- COWARD, H. & JONES, G. 1952 Limits of flammability of gases and vapors. *Tech. Rep.. DTIC Document*.
- CURNICK, O. J., MENDES, P. M. & POLLET, B. G. 2010 Enhanced durability of a pt/c electrocatalyst derived from nafton-stabilised colloidal platinum nanoparticles. *Electrochemistry Communications* **12** (8), 1017 – 1020.
- DEBE, M. K., POIRIER, R. J., WACKERFUSS, M. K. & ZIEGLER, R. J. 1999 Membrane electrode assembly. US Patent 5,879,828.

- DHIR, A. 2008 *Improved Microtubular Solid Oxide Fuel Cells*. PhD Thesis, The University of Birmingham.
- ELLIS, M., VON SPAKOVSKY, M. & NELSON, D. 2001 Fuel cell systems: efficient, flexible energy conversion for the 21st century. *Proceedings of the IEEE* **89** (12), 1808–1818.
- FAUR GHENCIU, A. 2002 Review of fuel processing catalysts for hydrogen production in pem fuel cell systems. *Current opinion in solid state and materials science* **6** (5), 389–399.
- FERGUS, J. W. 2004 Lanthanum chromite-based materials for solid oxide fuel cell interconnects. *Solid State Ionics* **171** (1), 1–15.
- FUEL CELL HANDBOOK 2004 Eg&g technical services. Inc. *Science Applications International Corporation* .
- FUEL CELL TODAY 2013 Applications. <http://www.fuelcelltoday.com/about-fuel-cells/applications>.
- FUEL CELLS 2003 Fuel cell vehicles. [www.fuelcells.org](http://www.fuelcells.org).
- FUENTES, R. & BAKER, R. 2008 Synthesis and properties of gadolinium-doped ceria solid solutions for it-sofc electrolytes. *International Journal of Hydrogen Energy* **33** (13), 3480–3484.
- GÜLZOW, E. 2004 Alkaline fuel cells. *Fuel cells* **4** (4), 251–255.
- HANSEN, A. G. 1964 *Similarity analyses of boundary value problems in engineering*. Prentice-Hall.
- HUANG, K. & GOODENOUGH, J. B. 2009 *Solid oxide fuel cell technology: principles, performance and operations*. CRC Press.
- IVERS-TIFFE, E., WEBER, A. & HERBSTRITT, D. 2001 Materials and technologies for sofc-components. *Journal of the European Ceramic Society* **21** (1011), 1805 – 1811.
- JANARDHANAN, V. M. & DEUTSCHMANN, O. 2007 Modeling of solid-oxide fuel cells. *Zeitschrift für Physikalische Chemie* **221** (4), 443–478.
- JOHNSON, R. W. 1998 *Handbook of fluid dynamics*. CRC.
- JU, H. & WANG, C.-Y. 2004 Experimental validation of a pem fuel cell model by current distribution data. *Journal of the Electrochemical Society* **151** (11), A1954–A1960.
- KAWADA, T. & YOKOKAWA, H. 1996 Materials and characterization of solid oxide fuel cell. *Key Engineering Materials* **125**, 187–248.

- KENDALL, K. 2000 Hydrocarbon fuels: Hopes for a flame-free future. *Nature* **404** (6775), 233–235.
- KENDALL, M. 1993 Tubular cells. a study of a tubular solid oxide fuel cell. *Final Year Project Report, University of Middlesex* .
- KRIEGER, F. J. 1951 Calculation of the viscosity of gas mixtures .
- LEE, D., HAN, J.-H., CHUN, Y., SONG, R.-H. & SHIN, D. R. 2007 Preparation and characterization of strontium and magnesium doped lanthanum gallates as the electrolyte for it-sofc. *Journal of power sources* **166** (1), 35–40.
- LEHNERT, W., MEUSINGER, J. & THOM, F. 2000 Modelling of gas transport phenomena in softc anodes. *J. Power Sources* **87** (1), 57–63.
- LI, Q., HE, R., GAO, J.-A., JENSEN, J. O. & BJERRUM, N. J. 2003 The co poisoning effect in pemfcs operational at temperatures up to 200 c. *Journal of the Electrochemical Society* **150** (12), A1599–A1605.
- LI, Y., FU, Q. & FLYTZANI-STEFANOUPOULOS, M. 2000 Low-temperature water-gas shift reaction over cu- and ni-loaded cerium oxide catalysts. *Applied Catalysis B: Environmental* **27** (3), 179 – 191.
- LINDSAY, A. L. & BROMLEY, L. A. 1950 Thermal conductivity of gas mixtures. *Industrial & Engineering Chemistry* **42** (8), 1508–1511.
- LIU, M., LYNCH, M. E., BLINN, K., ALAMGIR, F. M. & CHOI, Y. 2011 Rational softc material design: new advances and tools. *Materials Today* **14** (11), 534–546.
- MEKSYN, D. 1961 *New Methods in Laminar Boundary-Layer Theory*. Oxford: Pergamon.
- MERKIN, J. & CHAUDHARY, M. 1994 Free-convection boundary layers on vertical surfaces driven by an exothermic surface reaction. *The Quarterly Journal of Mechanics and Applied Mathematics* **47** (3), 405–428.
- MERKIN, J. H. 1996 A model for isothermal homogeneous-heterogeneous reactions in boundary-layer flow. *Mathl. Comput. Model.* **24**, 125–136.
- MINH, N. Q. 2004 Solid oxide fuel cell technology features and applications. *Solid State Ionics* **174** (14), 271 – 277. Solid State Ionics Dokya Memorial Special Issue.
- MINH, N. Q. & TAKAHASHI, T. 1995 *Science and technology of ceramic fuel cells*. Elsevier Science.
- MOORE, F. K. 1951 Three-dimensional compressible laminar boundary-layer flow .
- MOUNIR, H., EL GHARAD, A., BELAICHE, M. & BOUKALOUCH, M. 2010 Non-isothermal and electrochemical modelling of the multi-cell module performance in the integrated-planar solid oxide fuel cell. *P. I. Mech. Eng. A-J. POW.* **224** (1), 23–33.

- MURRAY, E. P., TSAI, T. & BARNETT, S. 1999 A direct-methane fuel cell with a ceria-based anode. *Nature* **400** (6745), 649–651.
- NEWMAN, J. & THOMAS-ALYEKA, K. 2004 *Electrochemical Systems*. J. Wiley.
- Ó CONAIRE, M., CURRAN, H. J., SIMMIE, J. M., PITZ, W. J. & WESTBROOK, C. K. 2004 A comprehensive modeling study of hydrogen oxidation. *International journal of chemical kinetics* **36** (11), 603–622.
- PERRY, R. H. & GREEN, D. W. 2008 *Perry's chemical engineers' handbook*. McGraw-Hill New York.
- PETERS, N. 1976 Analysis of a laminar flat plate boundary-layer diffusion flame. *International Journal of Heat and Mass Transfer* **19** (4), 385 – 393.
- PRANDTL, L. 1904 Fluid motion with very small friction. *Proc. 3 Int. Congr. on Mathematics* .
- ROSENHEAD, L. 1963 *Laminar Boundary Layers*. Oxford: Clarendon.
- SCHLICHTING, H. & GERSTEN, K. 2004 *Boundary-layer theory*. Springer.
- SIMNER, S. P., BONNETT, J. F., CANFIELD, N. L., MEINHARDT, K. D., SHELTON, J. P., SPRENKLE, V. L. & STEVENSON, J. W. 2003 Development of lanthanum ferrite sofc cathodes. *Journal of power sources* **113** (1), 1–10.
- SINGHAL, S. 2000 Science and technology of solid-oxide fuel cells. *MRS Bulletin* **25** (3), 16–21.
- SINGHAL, S. & KENDALL, K. 2003 *High temperature solid oxide fuel cells: fundamentals, design, and applications*. Elsevier Science.
- STAMBOULI, A. B. & TRAVERSA, E. 2002 Solid oxide fuel cells (sofcs): a review of an environmentally clean and efficient source of energy. *Renewable and Sustainable Energy Reviews* **6** (5), 433–455.
- TADMOR, E. 2012 A review of numerical methods for nonlinear partial differential equations. *Bulletin of the American Mathematical Society* **49** (4), 507–554.
- TETZLAFF, K., WALZ, R. & GOSSEN, C. 1994 Alkaline falling-film fuel cell a breakthrough in technology and cost. *Journal of power sources* **50** (3), 311–319.
- TIETZ, F. 1999 Thermal expansion of sofc materials. *Ionics* **5** (1), 129–139.
- TU, X., GALLON, H., TWIGG, M., GORRY, P. & WHITEHEAD, J. 2011 Dry reforming of methane over a ni/al<sub>2</sub>o<sub>3</sub> catalyst in a coaxial dielectric barrier discharge reactor. *Journal of Physics D: Applied Physics* **44** (27), 274007.

- VERBRAEKEN, M. C., IWANSCHITZ, B., MAI, A. & IRVINE, J. T. 2012 Evaluation of ca doped  $\text{La}_{0.2}\text{Sr}_0.7\text{TiO}_3$  as an alternative material for use in sofc anodes. *Journal of The Electrochemical Society* **159** (11), F757–F762.
- WANG, S., KOBAYASHI, T., DOKIYA, M. & HASHIMOTO, T. 2000 Electrical and ionic conductivity of gd-doped ceria. *Journal of The Electrochemical Society* **147** (10), 3606–3609.
- WINSEL, A., FÜHRER, O., RÜHLING, K. & FISCHER, C. 1990 Eloflux fuel cells and electrolysis cells. *Berichte der Bunsengesellschaft für physikalische Chemie* **94** (9), 926–931.
- ZHU, W. & DEEVI, S. 2003a Development of interconnect materials for solid oxide fuel cells. *Materials Science and Engineering: A* **348** (1), 227–243.
- ZHU, W. & DEEVI, S. 2003b A review on the status of anode materials for solid oxide fuel cells. *Materials Science and Engineering: A* **362** (1), 228–239.